Thermochronometry and Thermomechanical Modeling of the Taiwan Orogen

Christopher W. Fuller

Master of Science

University of Washington

2002

Department of Earth and Space Sciences

1.0 Introduction

The mechanics of mountain building has long been an area of study in the earth sciences (e.g. Hall, 1859; Broggi, 1932). Particular interest has been given to the deformational history and kinematics of convergent orogens (e.g. Chapple, 1978; Cowan and Silling, 1978; Suppe, 1980; Davis et al., 1983; Stockmal, 1983; England and Houseman, 1985; Escher and Beaumont, 1997; Brandon et al., 1998; Batt and Braun, 1999; Tang and Chemenda, 2000) (figure 1.1). In convergent orogens with high erosion rates and rapid uplift, geologic structures and stratigraphic relationships are unable to elucidate long-term kinematic relationships due to the removal of a large portion of the geologic record (Batt and Brandon, 2002). In these cases it is common to use thermochronometry and observations of metamorphic assemblages to construct pressure or temperature histories of the rocks in the orogen as the main constraint on the deformational and kinematic history (e.g. Zeitler, 1985; Copeland and Harrison, 1990; Barr and Dahlen, 1991; Batt and Braun, 1999; Wintsch et al., 1999).

While metamorphic assemblages have the potential to indicate the maximum pressures and temperatures reached by materials, they are generally unable to give precise temporal bounds on when these temperatures and pressures were reached. However, thermochronometry does allow for the prediction of the time since materials pass through specific temperatures (Dodson, 1973, 1979). Therefore, increasing interest has been placed in the use of thermochronometry over other methods in studies of orogen evolution. In particular, researchers have focused on the suite of low-temperature (less than ~300 ˚C) thermochronometers including zircon fission track dating (ZFT), apatite fission track dating (AFT) and apatite (U-Th)/He ages (e.g. Wagner, 1968; Wagner and Reimer, 1972; Zeitler, 1985; Wolf et al., 1996a; Brandon et al., 1998; Batt and Braun, 1999; Garver et al., 1999; Batt et al., 2001). With average closure temperatures ranging between ~70 ˚C and ~240 ˚C (Wagner and Reimer, 1972; Krishnaswami et al., 1978; Wolf et al., 1996b), this suite of thermochronometers is able to record three different stages of a material's thermal history as it is exhumed from moderate depth to surface temperatures (figure 1.1). In order to use the thermal history as a constraint on orogen kinematics, we require knowledge of the orogen's thermal structure.

The thermal structure of a non-deforming portion of the continental crust is primarily controlled by the conduction of heat from the asthenosphere and the generation of heat from radiogenic elements in the crust. In convergent orogens there may be additional heating from thickening of the radiogenic crust (Huerta et al., 1999), friction on faults (Scholz, 1980), the removal of subducted oceanic or continental lithosphere (Sacks and Secor, 1990) and its replacement by hotter asthenosphere (Houseman et al., 1981). There is also advective cooling from the subduction of lithosphere. This process is especially important in regions where subduction has been active for millions of years prior to orogen growth. The thermal structure of a convergent orogen is also complicated by the advection of heat from crustal motion (Clark and Jager, 1969; Koons, 1987; Batt and Braun, 1997). The precise effects of this advection depend on the kinematics of the orogen, but the general trend is to raise isotherms near regions where exhumation rates are high.

With the complex thermal structure of orogens resulting from these factors, the question then becomes, given surface patterns of thermochronometer ages, what can be inferred about the deformation and kinematics of the orogen? A common technique for addressing this problem is the use of numerical models that take into account some, if not all, of the above factors in predicting the thermal structure and kinematics of convergent orogens (e.g. Barr and Dahlen, 1989; Dahlen and Barr, 1989; Huerta et al., 1996, 1998, 1999; Jamieson et al., 1996, 1998, 2002; Batt and Braun, 1997; Beaumont et al., 2001). The temperature histories from these models are used to make predictions of thermochronometer ages, which are then compared to observed data (e.g. Wagner et al., 1977; Green, 1986; Kamp et al., 1989; Barr and Dahlen, 1990; Batt and Braun, 1999; Batt et al., 2001). In this manner one can test the model parameterization of the orogen and gain insight into the deformational and kinematic history.

In this study I investigate the kinematics of convergent orogen growth and the ability of low-temperature thermochronometers to constrain orogen evolution. Previous workers have used both kinematic (Dahlen and Barr, 1989; Barr and Dahlen, 1989; Huerta et al., 1996, 1998, 1999; Batt et al., 2001) and dynamic (Jamieson et al., 1996, 1998, 2002; Batt and Braun, 1997, 1999; Beaumont et al., 2001) models of crustal deformation in convergent orogens coupled to thermal models to predict the temperature histories of material exposed at the surface. Some of these workers have also used models of thermochronometer behavior to compare thermochronometric ages from model temperature histories to observed ages for various orogens (Batt and Braun, 1997, 1999; Batt et al., 2001). However, none of these studies has combined the more advanced models of the thermal structure in subduction zones (Jamieson et al., 1996, 1998, 2002; Beaumont et al., 2001) with the latest predictive thermochronometry models for (U-Th)/He, AFT and ZFT dating (Wolf et al, 1998; Ketcham et al., 2000; Batt et al., 2001).

The study presented here is a new contribution to the field in that it uses a modified version of an existing thermomechanical model with a full thermal representation of a subduction zone setting (Willett, 1992a; Fullsack, 1995; Pope and Willett, 1998) to which I have added key components allowing for the evaluation of underplating as a mode of orogen growth and predictions of AFT, ZFT and (U-Th)/He ages (Wolf et al, 1998; Ketcham et al., 2000; Batt et al., 2001). I also present new AFT and ZFT ages for Taiwan that are used in conjunction with existing ages (Liu, 1982; Liu et al., 2001) to apply the model as applied to the Taiwan orogen. I address the following questions. What qualitative insights do the thermochronometers give towards the evolution of the Taiwan orogen? Can I produce an orogen with the same height, width and overall topographic expression as Taiwan? Can the observed pattern of thermochronometer ages, in particular the location of the reset zones, be reproduced? What erosion rates are consistent with the observed thermochronometer data? Do the patterns of reset thermochronometers constrain the importance of underplating as a mode of accretion? Finally, what rate of propagation for the Taiwan collision is consistent with the new thermochronometry data and the thermomechanical modeling?

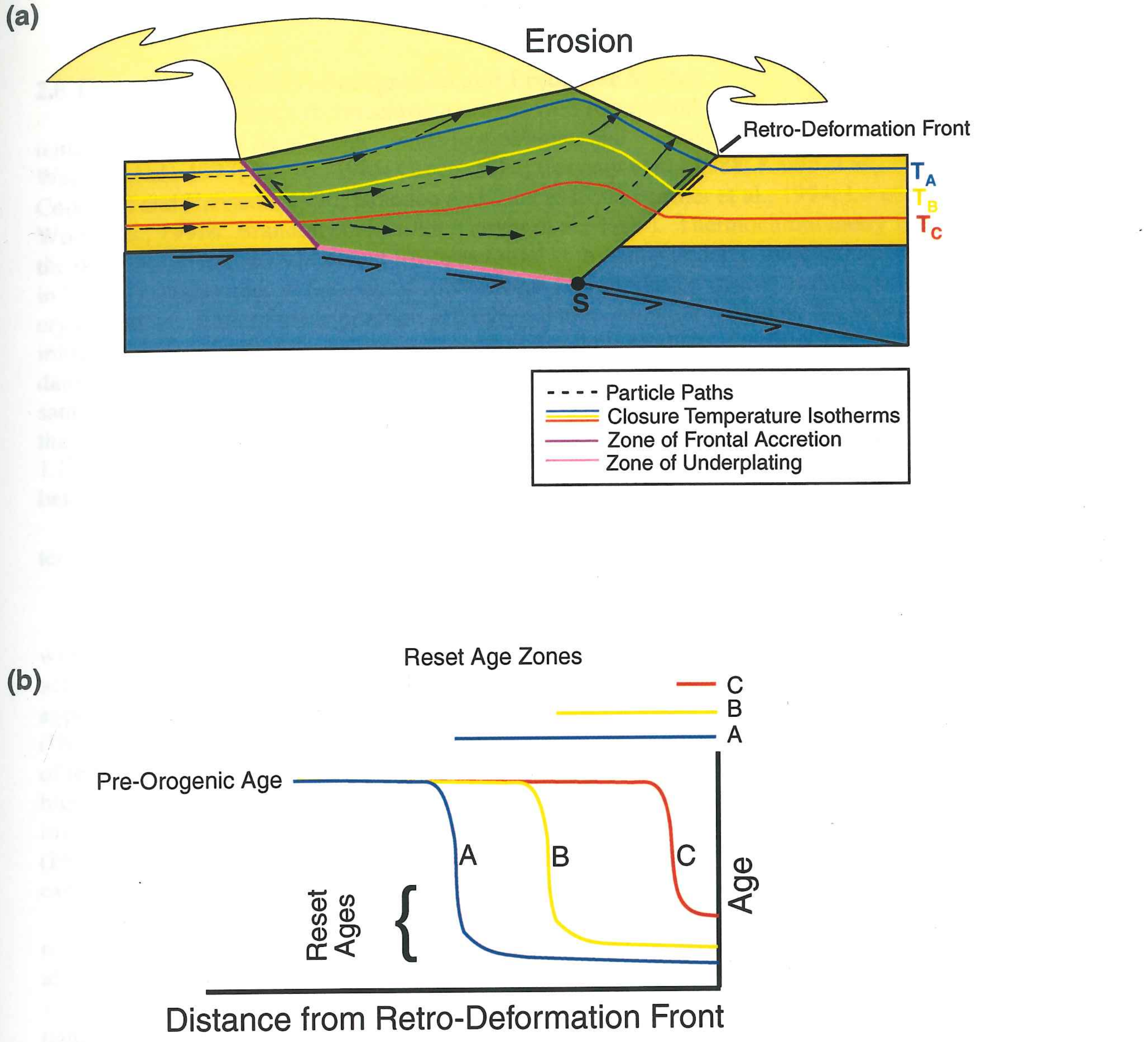

Figure 1.1: (a) Typical subduction related convergent orogen setting. S marks the discontinuity where material is no longer being transported from the subducting plate to the fixed, over-thrusting plate. The orogen has two modes of growth: frontal accretion and underplating. Hypothetical particle paths are shown passing through assumed closure temperatures for three thermochronometers. (b) The resulting surface patterns of thermochronometer ages. Reset ages for a particular thermochronometer are those that have passed through their respective closure temperature. *Modified from Willett and Brandon (2002).*

2.0 Thermochronometry: Background and Predictive Models

Low-temperature thermochronometry is well recognized for its ability to impose temporal constraints on orogenic events (e.g. Wagner and Reimer, 1972; Harrison et al, 1979; Wagner et al., 1977; Zeitler, 1985; Green, 1986; Cerveny et al., 1988; Kamp et al., 1989; Copeland and Harrison, 1990; Brandon and Vance, 1992; Burtner et al., 1994; Lo et al., 1995; Wolf et al., 1996a; Brandon et al., 1998; Garver et al., 1999). Thermochronometry is based on the observation that certain parent isotopes found in minerals undergo radioactive decay resulting in lighter isotopes and, in the case of spontaneous fission, fission tracks, or damaged tracks in the crystal lattice. Both of these products are referred to as daughter products. By knowing the initial concentrations of the parent isotopes and daughter products, the final concentrations of the daughter products and the rate of daughter generation, it is possible to determine the age of a sample. This technique is useful in the study of orogenesis because the age reflects the time since the sample has passed through a particular isotherm referred to as a "closure" isotherm (figure 1.1). The temperature of this isotherm depends on several factors and is discussed in more detail below.

Isotopic daughter products tend to diffuse out of the crystal lattice. Over certain temperatures the diffusion is described by the Arrhenius equation,

$$D = D_0 e^{\left(\frac{-E}{RT}\right)} \qquad (1)$$

where D is the diffusion coefficient, D_0 is the diffusion coefficient at infinite temperature, E is the activation energy, R is the gas constant and T is the temperature. This equation can also be applied to the temperature dependent annealing of fission tracks in a crystal lattice (equation 1) (Dodson, 1979). Daughter products diffuse or anneal out of the crystal lattice over a wide range of temperatures (figure 2.1). At most temperatures the rate of diffusion and annealing is either high enough that no significant amount of daughter product accumulates over geologic time or low enough that no significant amount of daughter product escapes. The partial retention zone (PRZ) of a thermochronometric system is the temperature range in between where the sample experiences no loss and total loss of daughter products on geologic time scales (figure 2.2).

As a sample cools through the PRZ, only a fraction of the produced daughter products are not diffused or annealed out of the crystal (figure 2.2). Once the sample leaves the PRZ it retains all of the daughter products. Since the sample only retains a portion of the daughter product while in the PRZ, the apparent age records a time when the sample was between the two temperature bounds of the PRZ. More specifically, the apparent age records the time at which the sample reached what is referred to as the closure temperature of the system (Dodson, 1973, 1979). The closure temperature model is useful in determining thermal histories since each thermochronometer has a unique closure temperature.

In a convergent orogen, material exposed at the surface has been heated and cooled through various PRZs dependent upon its path through the deforming orogen (figure 2.3a). The surface pattern of ages for a thermochronometer evolves with time as the orogen approaches steady-state thermal conditions (figure 2.3b) (Willett and Brandon, 2002). At the onset of exhumation (t_1, t_2) the apparent ages are pre-orogenic ages since samples have not reached high enough temperatures to lose all daughter products acquired prior to the orogenesis. These are referred to as unreset samples. As the orogen evolves (t_3-t_5) some young ages appear. These ages are referred to as reset since they are from samples that lost all daughter products due to orogenic heating and have begun to accumulate them again. With time the zone of reset ages widens and continues to widen until the orogen reaches an exhumational steady where the reset ages do not change with time. Throughout the evolution of the orogen some samples reach temperatures above the lower bound of the PRZ yet below the closure temperature allowing for partial diffusion or annealing of daughter products. These samples are referred to as partially reset. At any time in the evolution of the orogen the ages from different thermochronometers will show a nested pattern reflecting their respective closure temperatures (figure 2.3c).

While the concepts behind the expected patterns of thermochronometer ages in a convergent orogen are fairly simple, interpreting them in terms of orogen kinematics is difficult without the use of predictive thermomechanical models. With the temperature histories from the model, age patterns can be predicted using annealing and diffusion models. In this study I use models to predict ages for (U-Th)/He dating in apatite and fission track dating in apatite and zircon.

2.1 (U-Th)/He Dating in Apatite

The retention of ^{4}He in apatite from the decay of ^{238}U, ^{235}U and ^{232}Th first gained recognition as a low-temperature thermochronometer by Zeitler et al. (1987) and has since been applied successfully to studies of exhumation (e.g., Wolf et al., 1996a; Batt et al., 2001). The diffusion of He from apatite displays a linear Arrhenius relationship at temperatures below ~265 °C that is well modeled by thermally activated volume diffusion in a sphere (Farley, 2000; Wolf et al., 1996b). Closure temperatures and PRZ zones are primarily dependent on grain size, diffusion coefficient at infinite temperature (D_0) and the cooling rate (Zeitler et al., 1987; Wolf et al., 1996b; Wolf et al., 1998; Farley, 2000).

2.1.1 Predictive Model

The amount of He present in a sample depends on the production of He from the decay of ^{238}U, ^{235}U and ^{232}Th and the diffusion of He. The change in He concentration with respect to time t and radial distance r within a spherical diffusion domain a is

$$\frac{\partial^4 He(r,t)}{\partial t} = \frac{D(t)}{a^2}\left[\frac{\partial^{2\,4} He(r,t)}{\partial r^2} + \frac{2}{r}\frac{\partial^4 He(r,t)}{\partial r}\right] \qquad (2)$$
$$+ 8\lambda_{238}\,{}^{238}U(t) + 7\lambda_{235}\,{}^{235}U(t) + 6\lambda_{232}\,{}^{232}Th(t)$$

where $He(t)$, $Th(t)$ and $U(t)$ are the amounts of the isotopes present at time t and $D(t)$ is the temperature, and thus time, dependent diffusion coefficient from equation (1) (Wolf et al., 1998). In application, the He contributions from the decay of ^{235}U can be ignored due to the small faction of He it contributes relative to ^{238}U, e.g. 0.5% over 2×10^8 yr (Wolf et al., 1998). Analytical solutions to equation (2) exist assuming constant He production and diffusivity, but for geologic applications with varying temperature and diffusivity (figure 2.1), a numerical solution should be used (Batt et al, 2001; Ehlers, 2001; Wolf et al., 1998). In this study I use the finite element solution to spherical diffusion as described by equation (2) developed by Ehlers (2001).

2.1.2 Model Behavior

Isothermal holding models illustrate the temperature dependence of diffusion (figure 2.4). The parameters used are those of Farley (2000), $D_0 = 50.0 \times 10^8$ μm²/s and $E = 33.0$ kcal/mol, with moderate concentrations of ^{238}U and ^{232}Th, 13.0 and 27.0 ppm respectively, and a grain radius of 42.5 μm. At temperatures above 50 °C rapid diffusion allows for little accumulation of He resulting in ages orders of magnitude less than the holding time. When the temperature is decreased to 25 °C the rate of diffusion is low enough that the He ages are similar to the holding time. Also, closure temperatures are highly dependent on the grain size given that the diffusion domain for He is the entire apatite grain (figure 2.5a). Therefore, larger grains are able to diffuse more He and have lower closure temperatures than smaller grains.

2.2 Fission Track Dating in Apatite and Zircon

Fission track dating is based on the relationship between the number of damaged tracks left in a crystal lattice from the spontaneous fission of an isotope to the age of the sample with respect to the closure temperature. ^{232}Th, ^{235}U and ^{238}U all undergo spontaneous fission, but over geologically reasonable periods of time only ^{238}U has enough fission events to be useful in dating. When U undergoes fission, the nucleus breaks into two lighter nuclei that recoil in opposite directions. The highly charged fragments disturb the electron balance in their path leaving a positively charged zone of ions. These ions repulse each other creating a track a few angstroms wide and 10-20 μm in length. Using a chemical etchant the tracks can be made visible under an optical microscope (Fleischer and Price, 1964; Fleischer, et al., 1964; Naeser, 1979; Ravenhurst and Donelick, 1992). The damaged zones of the crystal are not stable, and undergo shortening, or annealing, through a temperature dependent diffusion process (Green et al., 1986; Donelick et al., 1990). The annealing of tracks occurs when a sample is within or above the PRZ described above. If a sample is held above the closure temperature over geologic timescales there is complete annealing of the fission tracks. In theory, knowing the abundance of ^{238}U, the density of tracks in a sample and the rate at which fission occurs an apparent age can be determined for the sample (see Ravenhurst and Donelick (1992) for complete details of age determinations).

2.2.1 Apatite Annealing Model

The mechanisms of fission track annealing are poorly understood leading researchers to develop empirical annealing models (e.g. Duddy et al., 1988; Willett, 1992b; Crowley, 1993; Ketcham et al., 2000). In this study I use a model described by Ketcham et al. (1999, 2000). The primary benefit of this model is its ability to account for the variable annealing behavior of apatite (Carlson et al, 1999). While researchers believe that the variable annealing characteristics primarily depend on composition of the apatite grains (Green et al, 1985, 1989; Ketcham et al., 1999), researchers have shown that annealing properties in apatite correspond to the easily measured etch pit diameter on the grain, D_{par}, (Donelick, 1993; Burtner et al., 1994). The etch pits are a feature of the fission-track dating process where grains are etched in acid to help reveal fission tracks. The model of Ketcham et al. (2000), and the model used here, is formulated to allow for variability in annealing properties as correlated to D_{par}.

I have written the predictive AFT thermochronometry described by Ketcham et al. (1999, 2000) in a new form to allow for the batch processing of temperature histories without extensive user interaction. This model has been calibrated to the model of Ketcham et al. (2000). Below I give a brief overview of the model. For more details the reader is directed to Ketcham et al. (1999, 2000), Willett et al. (1992b) and Duddy et al. (1988). The model takes a time-temperature history and divides it into a number of substeps or components. Each component represents a population of tracks that formed during a segment of the history. All of the components are annealed according to an annealing function dependent upon D_{par} from the beginning of their substep until the end of the temperature history. This calculation determines the mean track length of each component. A mean track length for the entire sample is then calculated from a weighted sum of the components and converted to a fission track age.

2.2.2 Zircon Closure Temperature Model

Attempts at developing an annealing model for zircon similar to those of apatite have not been successful due to significant discrepancies between closure temperatures determined from experimental and geologic studies (e.g. Brandon and Vance, 1992; Yamada et al., 1995; Foster et al., 1996). Therefore, I determine ZFT ages using effective closure temperatures as defined by (Dodson, 1973, 1979)

$$\dot{T} = \frac{-RT_c^2}{\bar{E}Be^{\bar{E}/(RT_c)}} \qquad (3)$$

where $\dot{T}$ is the cooling rate, R is the universal gas constant, T_c is the effective closure temperature, $\bar{E}$ is the activation energy measured at 50% annealing and B is a material proportionality constant. I follow Batt et al. (2001), and use values of $B = 3.160 \times 10^{-22}$ (My) and

$\bar{E} = 49.77$ (kcal/mol) as estimated by Brandon et al. (1998) and Brandon and Vance (1992). For a given temperature history, I approximate the cooling history between 200 ˚C and 300 ˚C with a constant cooling rate and determine the closure temperature from equation (3). The ZFT age is then calculated as the time since the sample passed the closure temperature. Batt et al. (2001) note that this technique agrees with closure temperatures determined from $^{40}Ar/^{39}Ar$ analyses in the study of Foster et al. (1996). It should be noted that this model does not allow for the partial annealing of samples.

2.2.3 Behavior of Fission Track Models

Figure 2.5b shows the dependence of AFT closure temperatures on both D_{par} and cooling rate as determined from the annealing model. A D_{par} value of 1.6 is common for easily annealed apatite while 2.4 is in the range of the most commonly observed resistive apatites. In general, the PRZ is 20 to 40 ˚C higher than the closure temperature and extends to ~20 ˚C (Donelick et al., 1990; Willett, 1992b). Figure 2.5c shows the closure temperature of zircon as determined directly from equation (3).

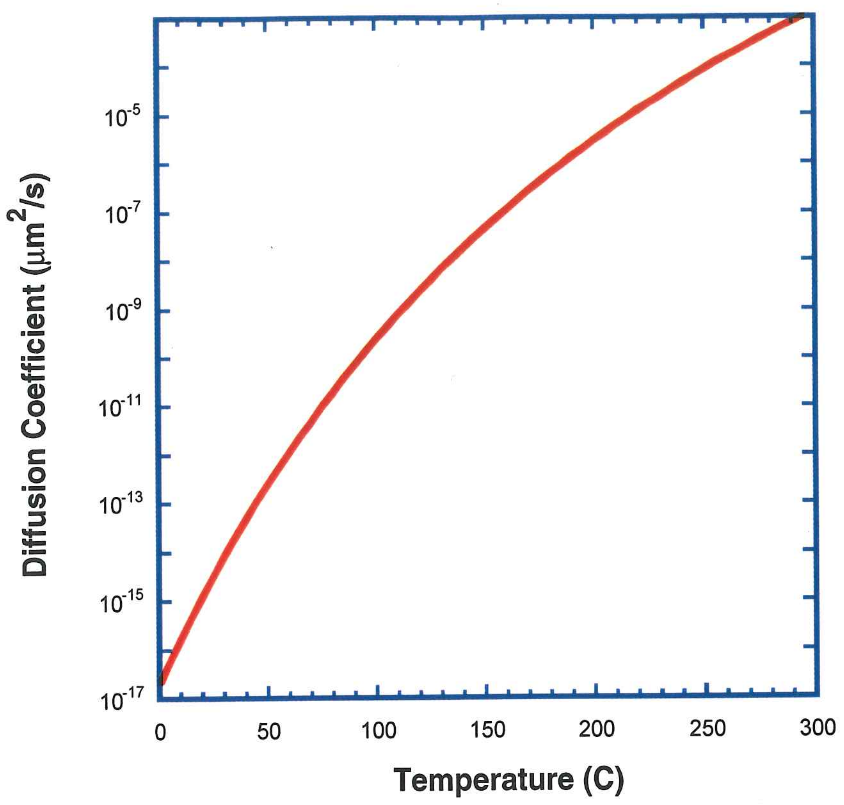

Figure 2.1: Temperature dependence of He diffusion in apatite as modeled with equation (1). Values for D_0 and *E* are taken from Farley (2000).

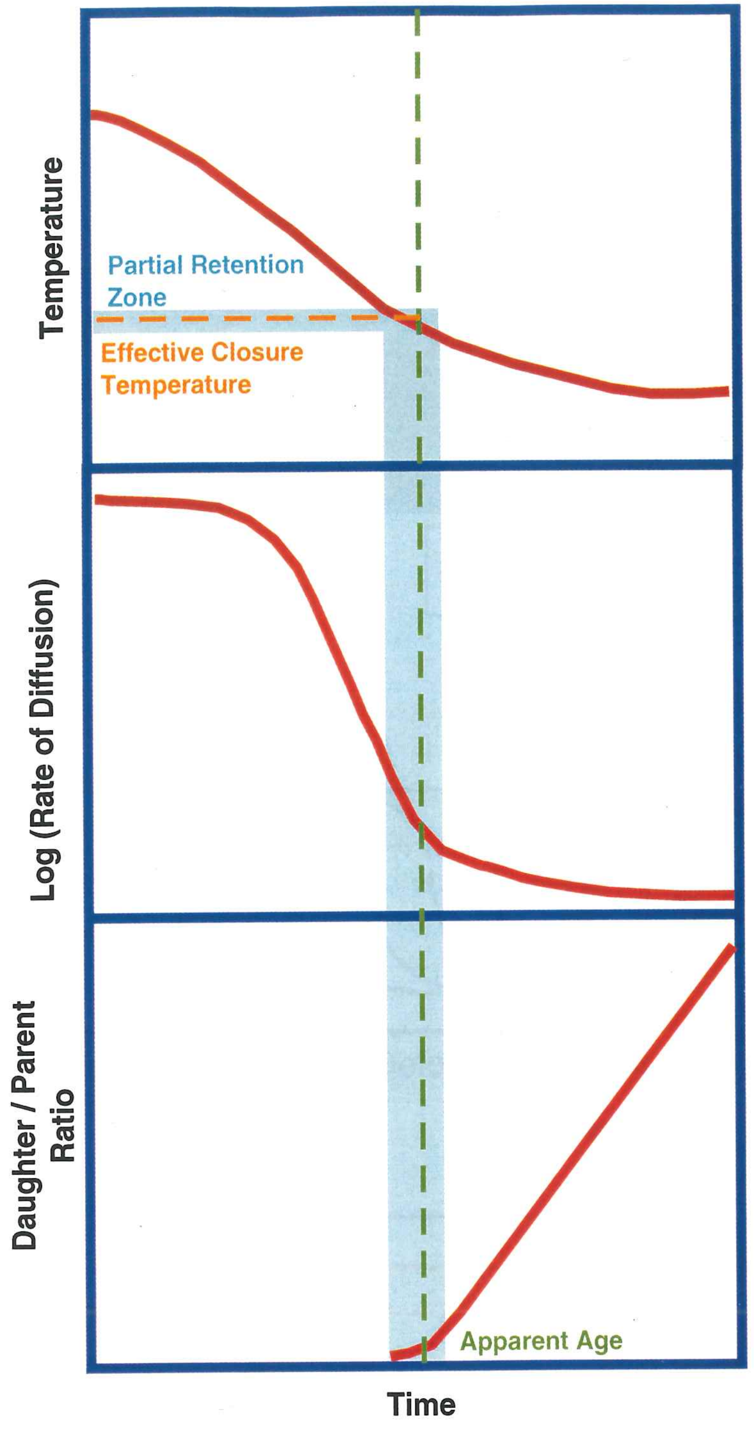

Figure 2.2: Hypothetical temperature history of a sample and the resulting behavior of the diffusion coefficient and ratio of daughter to parent. Note that no daughter products are retained until the sample reaches the partial retention zone (PRZ) and that upon leaving the PRZ all daughter products are retained. Also note the correlation between the apparent age and the effective closure temperature that is bracketed by the PRZ.

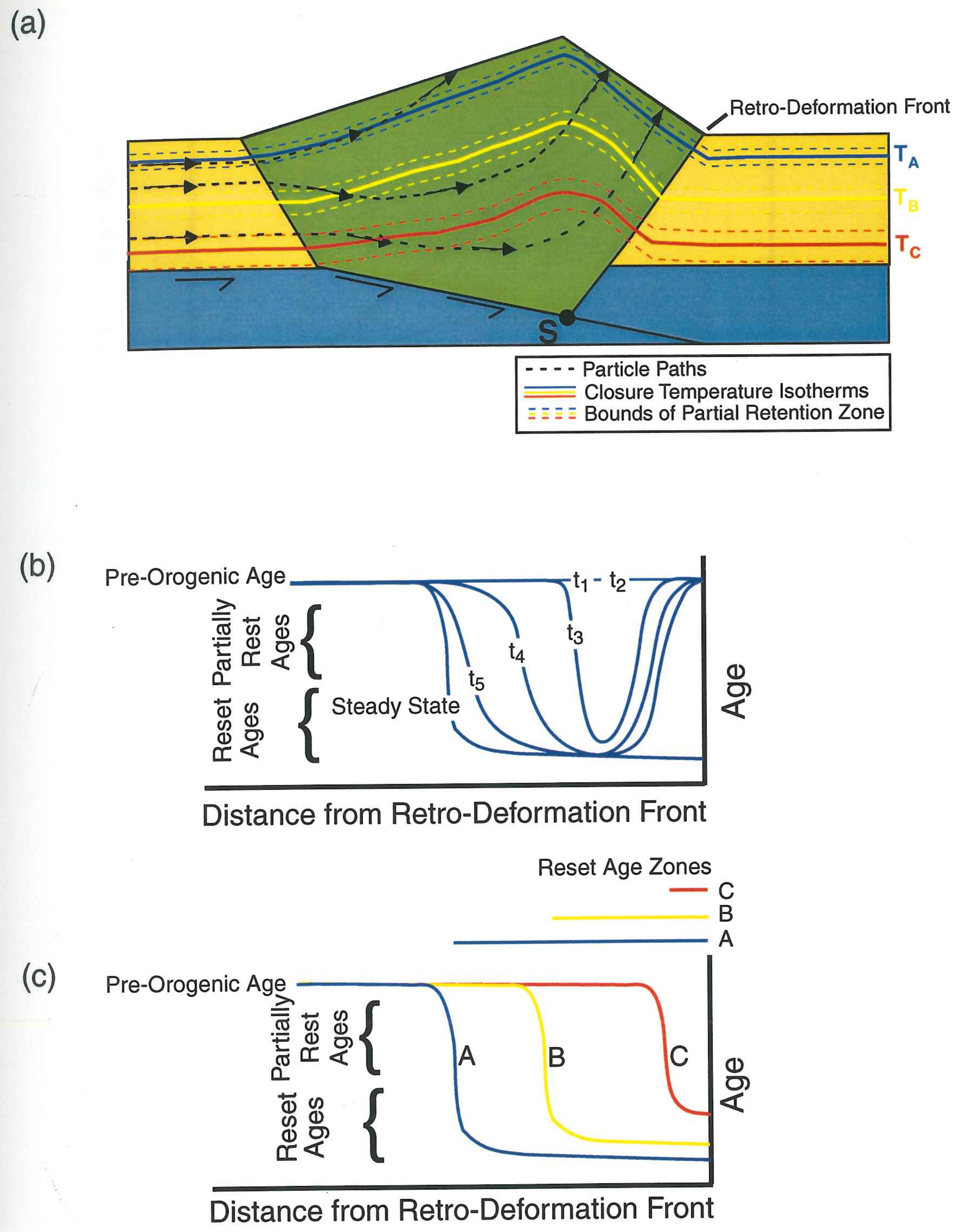

Figure 2.3: (a) Hypothetical orogen during steady-state conditions with particle paths and closure temperatures for thermochronometers A, B, and C. (b) The distribution of ages for thermochronometer A evolve through time until a steady state is reached. Ages are classified as reset, partially reset or unreset (pre-orogenic). (c) At any time in the evolution of the orogen, a suite of thermochronometers will display a nested pattern of reset ages corresponding to closure temperature. *Modified from Willett and Brandon (2002).*

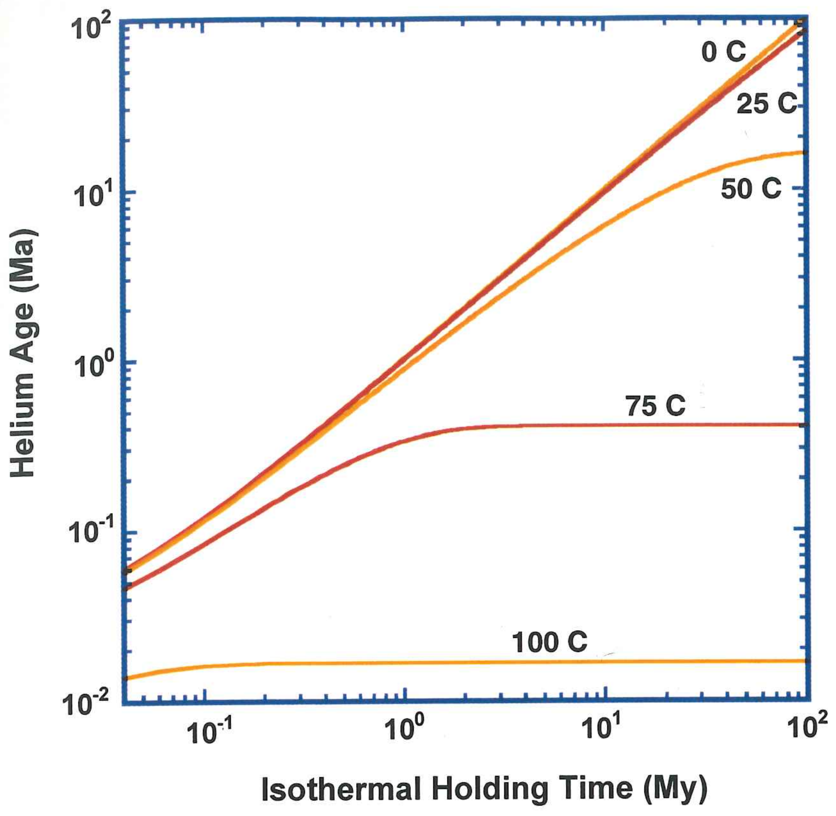

Figure 2.4: Dependence of helium ages on isothermal holding times. See text for parameter values used in these models.

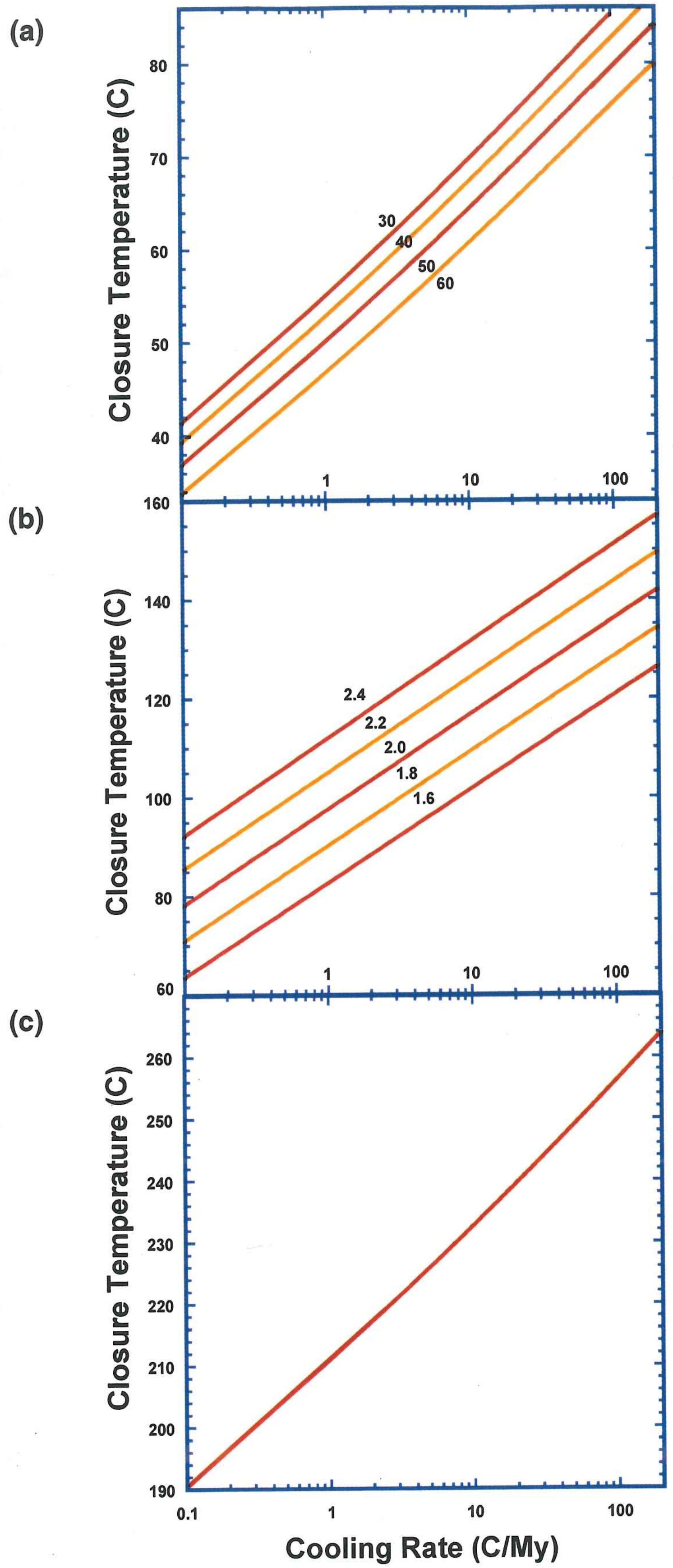

Figure 2.5: Closure temperatures for constant cooling rates determined from the models used in this study. (a) He closure temperatures varying with diffusion domain size or grain radius (in mm). (b) AFT closure temperatures varying with kinetic parameter D_{par} (in µm). (c) ZFT closure temperature model used in this study. See text for parameter values.

3.0 Modeling Background

While numerical models have been used in studies of convergent orogenesis (e.g., Bird, 1978; England and McKenzie, 1982), using them to predict detailed pressure and temperature histories and thermochronometer ages is relatively recent (Barr and Dahlen, 1989, 1990; Batt and Braun, 1997). With one of the main focuses of this study being the use of a thermomechanical model to predict surface patterns of thermochronometer ages in an evolving orogen, it is useful to look at previous studies in this field. Below I review models that have either kinematically or dynamically solved for crustal deformation in a convergent orogen and tracked material through the orogen evolution to determine pressure and or temperature histories.

Each model describes deformation in two dimensions and has two components: a solution to the velocity field that allows for the tracking of particles and a solution to the temperature field that allows for the determination of temperature histories for the tracked particles. Within the velocity models there are four characteristics that typically vary: the domain of the model, the method of solving for the velocity, the erosion law used and whether or not underplating is explicitly formulated as a boundary condition. In the thermal models key differences are the components included in the heat production term in the heat transfer equation, the domain of the model and the basal boundary condition for the thermal model. Finally, while all of the models determine pressure or temperature histories, what is finally predicted with these histories also varies between models.

The previous modeling efforts I look at are referred to as follows: the Barr & Dahlen model (Dahlen and Barr, 1989; Barr and Dahlen, 1989, 1990; Barr et al., 1991), the Batt & Brandon model (Batt et al., 2001), the Huerta model (Huerta et al., 1996, 1998, 1999), the Batt & Braun model (Batt and Braun, 1997, 1999) and the Jamieson & Beaumont model (Jamieson et al., 1996, 1998, 2002; Beaumont et al., 2001). Each of these models is looked at in detail below, and table 2.1 summarizes the main features of each model.

3.1 Barr & Dahlen Model

The model of Barr & Dahlen (Dahlen and Barr, 1989; Barr and Dahlen, 1989, 1990; Barr et al., 1991) predicts the kinematics of accretionary wedges and fold-and-thrust belts with the assumption that stresses are determined by a Coulomb failure criterion in a wedge (Davis et al., 1983). They use a kinematic description of the velocity field determined by enforcing a flux balance between accreted and eroded material and by assuming an isotropic and incompressible material. The domain of the kinematic model is from the toe of the accretionary wedge to a no-flux backstop and down to the decollement. Their model allows for the explicit use of underplating as a mode of accretion implemented as a constant flux across the entire decollement and for uniform erosion of the upper surface. The production term in the heat flow equation includes radiogenic heating, internal strain heating and shear heating on the decollement. The domain of the thermal model extends below the decollement allowing for the effects of shear heating on the decollement. The basal boundary condition of the thermal model is a constant heat flux from the mantle. With the coupled model, Barr and Dahlen (1989, 1990) predict pressure and temperature (P-T) histories for materials as they move through the orogen. In later work the (P-T) paths are applied to a thermodynamic model to make predictions of metamorphic assemblages (Barr et al. 1991).

3.2 Batt & Brandon Model

The velocity model of Batt & Brandon (Batt et al., 2001; Pazzaglia and Brandon, 2001) is similar to that of Barr & Dahlen since it also uses a kinematic description of the velocity field. The model domain is an accretionary wedge above a decollement between the toe and backstop. Batt & Brandon also allow for underplating and erosion across the orogen. Erosion is imposed along the entire subaerial portion of accretionary wedge according to an arbitrary function. In their work, Batt et al. (2001) and Pazzaglia and Brandon (2001) use an erosion function determined from field studies (Pazzaglia and Brandon, 2001). Underplating is also implemented along the entire length of the orogen distributed according to the same arbitrary function. The accretion of material into the orogen is allowed to vary between entirely by underplating to entirely by frontal accretion. The thermal model allows for heating from both radiogenic sources and shear heating on the decollement. The domain of the thermal model coincides with the kinematic model, and they prescribe the lower temperature boundary condition according to an analytical solution of temperature at the base of an accretionary wedge (Molnar and England 1995). Batt & Brandon use the temperature histories from the model to predict AFT ages using the annealing model of Willett (1992b), ZFT ages using the effective closure temperature technique described by Dodson (1973, 1979), and (U-Th)/He ages using the approach from Wolf et al. (1996b).

3.3 Huerta Model

The model of Huerta et al. (1996, 1998, 1999) also uses a kinematic solution for the velocity field. The domain of the model is that of a collisional orogen with a slab of subducting continental lithosphere being overridden by wedge of continental lithosphere. With accretion of new material occurring as a vertical transfer of material across the subduction boundary, the material velocity in the upper plate is easily derived from the magnitude of erosion, uniform along the upper surface, the magnitude of accretion and the dip of the subduction contact. Similarly, the velocity in the lower plate is determined from the convergence velocity and the velocities in the upper plate. Formulated as such, the model does not allow for the explicit implementation of underplating. The domain for the thermal solution is the same domain as the kinematic solution, and the heat transfer equation is solved with radiogenic heating as the only production term. Finally, there is a constant temperature basal boundary condition for the thermal model representing the temperature at the lithosphere/asthenosphere contact. The temperature and temperature-depth histories of tracked particles are compared to the stability fields of kyanite, andalusite and sillimanite.

3.4 Batt & Braun Model

The Batt & Braun (1997, 1999) model simulates continental collision in a subduction setting. They use a dynamic solution to the velocity field in the crust for a temperature dependent, visco-elastoplastic rheology using a finite element formulation. The domain of the velocity component encompasses the entire crust in vertical extent and extends laterally well beyond the actively deforming region. Erosion of the upper surface of the model is handled through diffusive and fluvial means primarily dependent upon a stream-power type erosion law (Kooi and Beaumont, 1996). The formulation of this model does not explicitly allow for underplating as a mode of accretion. Again, radiogenic heating is the only production term considered in the thermal solution. The domain of the thermal model coincides with the crust of the velocity model, and the base of the model is held at a constant temperature. With the pressure-temperature histories determined for the tracked material AFT ages and K-Ar ages in K-feldspar, biotite, muscovite and hornblende are calculated. The AFT ages are determined from an annealing model as presented by van der Beek (1995), and the K-Ar ages are calculated using effective closure temperatures as described by Dodson (1973).

3.5 Jamieson & Beaumont Model

The Jamieson & Beaumont model (Jamieson et al., 1996, 1998, 2002; Beaumont et al., 2001) obtains a dynamic solution of the crustal velocity field for continental collision in a subduction setting assuming a viscoplastic rheology and using a finite element formulation. The erosion law is similar to that of the Batt & Braun model using a stream-power formulation dependent on slope and contributing area, and there is no explicit underplating. Once again, radiogenic heating is the only term considered in the heat production. However, unlike any of the previous models, the Jamieson & Beaumont thermal model extends to the upper asthenosphere encompassing the kinematics and thermal effects of the subducting lithosphere. The model uses a constant temperature boundary condition representing the temperature of the asthenosphere at the base of the model. The temperature-pressure histories from the tracked particles are compared to known pressures and temperatures of metamorphic assemblages.

	VELOCITY MODEL				THERMAL MODEL			
Model	Domain	Velocity Solution	Erosion Law	Underplating	Domain	Heat Production Includes...	Basal Boundary Conditions	Predictions
Barr and Dahlen	Accretionary wedge	Kinematic	Uniform	Uniform along decollement	Surface to downgoing plate	Radioactive decay, shear heating, strain heating	Constant heat flux	Metamorphic assemblages, P-T histories
Batt and Brandon	Accretionary wedge	Kinematic	Arbitrary function, from field work	Arbitrary function, matched surface uplift	Same as velocity model	Radioactive decay, shear heating	Analytical solution	AFT, ZFT, (U-Th)/He ages
Huerta	Subducting and overriding lithosphere	Kinematic	Uniform	Not explicit	Same as velocity model	Radioactive decay	Constant temperature	Temperature-depth histories
Batt and Braun	Crust	Dynamic: visco-elastoplastic rheology	Slope and contributing area dependent	Not explicit	Same as velocity model	Radioactive decay	Constant temperature	AFT and K-Ar ages
Jamieson and Beaumont	Crust	Dynamic: viscoplastic rheology	Slope and contributing area dependent	Not explicit	Surface to upper asthenosphere	Radioactive decay	Constant temperature	P-T histories

Table 3.1: The five models looked at in this study and their key components.

4.0 Thermomechanical Model

In this study I use a thermomechanical model of convergent orogenesis adapted from Willett (1992a), Fullsack (1995) and Pope (1997). To the model of Pope (1997) I have made three major modifications: (1) addition of a particle tracking routine to determine the temperature histories of material at the surface, (2) the coupling of predictive thermochronometry models for AFT, ZFT and (U-Th)/He dating and (3) addition of underplating as a mode of accretion. With these additions the model can be viewed as a hybrid of the models presented above since it uses a dynamic solution to the velocity field similar to the Batt & Braun and Jamieson & Beaumont models, has a thermal model that includes the subducting lithosphere and extends to the asthenosphere similar to the Jamieson & Beaumont models and predicts (U-Th)/He, AFT and ZFT ages similar to the Batt & Brandon model (Batt et al., 2001).

4.1 Mechanical Model

Deformation with in the crust is modeled as a quasi-static creeping flow with a plastic yield criterion (Zienkiewicz and Godble, 1974). Assuming the Stokes condition, the Navier-Stokes equation of motion in two dimensions for an Eulerian reference frame is then

$$\rho g_j - \frac{\partial p}{\partial x_i} - \frac{\mu}{3}\frac{\partial^2 v_i}{\partial x_i \partial x_j} = 0 \qquad (1)$$

where v is the velocity, t is time, p is the pressure, μ is a viscosity coefficient, g is gravity and summation is implied over repeated indices and i, j = 1,2. The flow is considered almost incompressible resulting in the continuity equation

$$\frac{p}{\kappa} + \frac{\delta v_i}{\delta x_i} = 0 \qquad (2)$$

where κ^{-1} is a penalty factor used to assure the compressibility of the material. The three unknowns in equations (4) and (5), velocity in two directions and pressure, are solved for using an arbitrary Lagrangian-Eulerian (ALE) finite element formulation (Fullsack, 1995). The finite element method used here is implemented with mixed quadrilateral elements in velocity and pressure giving a bilinear velocity interpolation and constant pressure for an element (Bathe, 1996).

At high temperatures or low stresses, crustal material is assumed to deform viscously following the constitutive equation

$$D_{ij} = A\sigma_{ij}\exp\left(\frac{-Q}{RT}\right) \qquad (3)$$

where σ is the stress tensor, D is the rate of deformation, or strain rate, tensor, T is the temperature, R is the universal gas constant, Q is the activation energy and A is a material constant. Following equation (6) the viscosity is

$$\mu = \frac{1}{A}\exp\left(\frac{Q}{RT}\right) \qquad (4)$$

where the pre-exponential, A, is

$$A = \exp\left(\frac{Q}{RT_{ref}}\right)\frac{1}{\mu_{\min}} \qquad (5)$$

where μ_{min} is the viscosity at temperature T_{ref}. When the stresses are high and the temperatures are low, the material in the upper crust is observed to fail plastically (Kohlstedt et al., 1995) as described by the Coulomb failure criteria. In tensor notation, the Coulomb yield stress is defined as

$$\sigma_y = c\cos(\phi) + \frac{1}{3}J_1\sin(\phi) \tag{6}$$

and yielding occurs when

$$\sqrt{J'_2} \geq \sigma^y \tag{7}$$

where c is the cohesion of the material, φ is the internal angle of friction, J_1 is the first stress invariant and J'_2 is the second invariant of the deviatoric stress defined respectively as

$$J_1 = \sigma_{kk} \tag{8}$$

$$J'_2 = -\frac{1}{2}\sigma'_{ij}\sigma'_{ij} \tag{9}$$

The deviatoric stress tensor, σ' is

$$\sigma'_{ij} = \sigma_{ij} - \frac{1}{3}\delta_{ij}\sigma_{kk} \tag{10}$$

where δ_{ij} is the Kronecker delta.

When failure occurs an effective viscosity is determined from the Coulomb failure criteria (Willett, 1992a)

$$\mu_{eff} = \frac{c\cos(\phi) + \frac{1}{3}J_1\sin(\phi)}{2\sqrt{I'_2}} \tag{11}$$

where I'_2 is the second invariant of the deviatoric rate of deformation tensor.

The model simulates a subduction zone setting by using a velocity discontinuity at point S where the basal tangential velocity, v_{tan}, goes from the convergence velocity, v_c, on the pro-side to zero on the retro side (figure 4.1a). The pro and retro edges of the domain have velocity boundary conditions of $v_x = v_c$ and $v_x = 0$ respectively. The upper surface is a free surface that erodes due to hillslope and fluvial processes. Fluvial erosion follows the law of Howard and Kirby (1983) assuming a linear dependence of erosion rate on stream power and linearly increasing downstream discharge,

$$\dot{e}_v = k_v x_r \left|\frac{dh}{dx}\right| \tag{12}$$

where k_v is a proportionality constant, x_r is the distance from the drainage divide and dh/dx is the slope of the river bed (Willett, 1999). The hillslope erosion is governed by

$$\dot{e}_r = k_r(h_{ridge} - h_{valley})^n \tag{13}$$

where k_r and n are empirical constants, h_{ridge} is the height of the ridge profile and h_{valley} is the height of the valley profile. To calculate erosion rates ridge and valley surfaces are tracked through the evolution of the model. The mean of these surfaces is used as the upper surface in the mechanical model (figure 4.2). The erosion routine acts over a limited region of the model surface. This region is defined as either the bounding basins of the orogen or the portion of the orogen that is exposed above a defined sea level (see below for example) (figure 4.1).

4.1.1 Underplating

One of the problems of previous dynamic models of deformation in convergent orogens is that they only account for frontal accretion as a mode of orogen growth (Jamieson et al., 1996, 1998, 2002; Batt and Braun, 1997, 1999; Beaumont et al., 2001). In this model underplating is simulated through an additional velocity boundary condition at the base of the mechanical model. The underplating zone begins at a prescribed row of nodes in the mechanical model, u_{beg}, and extends until the S point. A velocity normal to the lower boundary of the mechanical model, v_{up}, defines the magnitude of underplating (figure 4.1a). To enable comparisons between models with different amounts of underplating, the initial model thickness, h_o, scales with the magnitude and extent of underplating. The scaled model thickness, h_s, is determined so that the flux of material into the orogen remains constant for a constant initial thickness regardless of the amount of underplating. The scaled model thickness is determined from

$$h_s = \frac{Q_0 - Q_{up}}{v_c} \qquad (14)$$

where Q_o is the accretionary flux with no underplating, and Q_{up} is the underplating flux.

With a flux of material into the mechanical model along the boundary of the thermal and mechanical models, the prescribed velocity field of the thermal model needs to be augmented to conserve mass and heat. The flux of material across the mechanical model boundary for each element, Q_{in}, is described by

$$Q_{in} = \Delta x_m v_{up} \qquad (15)$$

where Δx_m is the distance along the base of the model between two nodes (figure 4.1c). To conserve mass and heat, the vertical flux of material out of the thermal model over the same horizontal distance, given by

$$Q_{out} = \Delta x_t v_z \qquad (16)$$

where Δx_t is the horizontal spacing between nodes and v_z is the vertical velocity component in the thermal model (figure 4.1c), needs to be equivalent to the flux into the mechanical model (18). This requirement results in each node of the thermal model below the zone of underplating having an addition vertical velocity of

$$v_z = \frac{Q_{in}}{\Delta x_t}. \qquad (17)$$

4.1.2 Particle Tracking

While the equations governing the velocity field of the mechanical model (equations 4 and 5) are solved on an Eulerian finite element mesh, a Lagrangian mesh is constructed to track material through the orogen (figure 4.5). In the vertical dimension the Lagrangian mesh extends from the surface of the mechanical model to at least the base of the mechanical model. In models with extensive underplating the mesh extends further to track underplated particles. The mesh also extends in horizontal extent beyond the model domain to account for material advected into the model. The Lagrangian mesh moves, or deforms, by interpolating the velocity solution determined for the Eulerian nodes to the Lagrangian nodes (Fullsack, 1995) (figure 4.5). Particle paths for materials exposed at the surface of the model are determined through a search algorithm that finds the closest Lagrangian node to defined points on the surface of the model. The position of the node is backtracked through model time to find the temperature history as determined from the thermal model described below. These temperature histories are then used in the predictive thermochronometry models described above (section 2).

4.2 Thermal Model

The thermal model is solved over the domain depicted in figure 4.1b encompassing the domain of the mechanical model, the subducting and over riding lithosphere and the upper asthenosphere. The temperature field is solved using the advective-conductive heat transfer equation with radiogenic heat production,

$$\rho c \frac{\partial T}{\partial t} = \frac{\partial}{\partial x}\left(k \frac{\partial T}{\partial x}\right) + \frac{\partial}{\partial z}\left(k \frac{\partial T}{\partial z}\right) - \rho c v_x \frac{\partial T}{\partial x} - \rho c v_z \frac{\partial T}{\partial z} + A \qquad (18)$$

where ρ is the density, *c* is the specific heat, *k* is the conductivity, *T* is the temperature, *t* is the time, v_x, v_z is the velocity in the x and z directions and *A* is the radiogenic heat production. The velocity for the mechanical model domain is taken from the dynamic solution and the velocity of the subducting lithosphere is prescribed kinematically. The velocity of the overriding lithosphere and the asthenosphere is set to zero. The subducting lithosphere is assigned the same velocity as the convergence velocity of the model, v_c, with a direction tangential to the mechanical/thermal model boundary left of the S point. Right of the S point the subducting lithosphere bends to the specified subduction angle, θ, and the velocity is tangential to the boundary between the subducting and overriding lithosphere. As described above, the velocity field is also augmented below zones of underplating. Equation (21) is solved using the finite element method with 3-noded triangular elements. Constant temperature boundary conditions are used along the upper and lower surfaces except where the subducting lithosphere reaches the base of the model. This area and the sides of the model are no heat flux boundaries. Finally, to simulate convergent margins where subduction takes place for an extended period of time prior to an arc or continental collision, the thermal model is designed to run for a specified amount of time, t_{runup}, without deformation in the crust.

4.3 Solution Procedure

The coupled thermomechanical model is non-linear due to the plastic failure, so an iterative time stepping approach is used:

1) Solve for the temperature field (eqn. 21).
2) Calculate the viscosity of each element using the temperature from the thermal model (eqn. 7).
3) Solve the Navier-Stokes equation (4) and the continuity condition (5) to determine a new velocity field. From the velocity field calculate the strain rate and stress.
4) For each element, check if stresses are below the yield stress (eqn. 10).
    a. If below, continue to next element.
    b. If above, calculate new effective viscosity from plastic flow law (14) and continue to next element
5) Compare velocity of current iteration to velocity of the previous iteration.
    a. If the convergence criterion is meet, go to step 6.
    b. If the convergence criterion is not met, go to step 3 and use the updated viscosities in the next iteration.
6) Update position of lagrangian mesh with velocity solution.
7) Erode upper surface.
8) Begin the next time step at 1.

At the end of the model run, particle paths and temperature histories of material at the surface are found as described above and used in the predictive thermochronometry models (section 2) to determine AFT, ZFT and (U-Th)/He ages.

4.4 Parameters

The parameters for the mechanical, thermal and thermochronometric models are listed in table 4.1 and 4.2. Parameters that are constant for all models shown in this study are in table 4.1. Table 4.2 lists variable parameters that are calibrated to the Taiwan orogen below (section 6). For the fixed parameters in the mechanical model, the rheological parameters (μ_{min}, T_{ref}, Q) are representative of a quartz rheology (Kronenberg and Tullis, 1984) and the material densities are typical for crustal and mantle values (Fowler, 1990). The ridge erosion parameters are independently determined through models not presented here to produce realistic ridge and valley profiles. One of the problems with a continuum model using the Coulomb failure criteria is that if the cohesion is too low and the time step size is too large, steep surfaces undergo massive failures creating anomalously large velocities. These high velocities are unrealistic and do not allow the model to converge to a solution. For this reason, the cohesion is kept as low as possible while avoiding numerical instabilities. Finally, the convergence velocity is selected for the Taiwan orogen and is described below (section 6).

For the fixed parameters in the thermal model, the thermal conductivities for the lithosphere and crust and the specific heat are within the range of observed values (Fowler, 1990), while the asthenosphere conductivity is high to simulate mantle convection. The subducting lithosphere thickness is set at a fairly low value (50 km) to allow for the development of a warm orogen. With a thicker lithosphere the temperature of the asthenosphere would need to be raised in order to reach the same temperatures within the orogen. The thermal model run-up time and slab dip are selected to represent the Taiwan orogen and are discussed below (section 5). All of the parameters for the thermochronometry models are fixed as described above (section 2) except for the kinetic parameter, D_{par}, for apatite.

4.5 Model Results

Below I present a suite of models demonstrating the model behavior. In particular I look at the effects of varying the erosion rate, amount and extent of underplating, by defining a sea level and thereby delaying the onset of erosion until the orogen is subaerially exposed and by including a crustal detachment. For this suite of models the asthenosphere temperature (T_a = 1360 °C), annealing model etch pit diameter (D_{par} = 1.8 μm), crustal heat production (A = 1.75 $\mu W/m^3$) and initial crustal thickness (h_o = 10 km) are held constant. Other model parameters are shown in table 4.3.

4.5.1 Reference Model

Model Mg4 has a fluvial erosion factor of 4.5, a uniform internal angle of friction of 15° and no underplating or imposed erosion constraint. Figure 4.3 shows the evolution of the temperature field from a pre-orogenic thermal steady state (time = 0 My) through 10 My of convergence. The thermal field is dominated by competition between the advection of heat from erosion and subduction. Figure 4.4 shows the second invariant of the strain rate tensor. As was described above, the material in the model deforms as a creeping flow until the stress exceeds the Coulomb yield stress (equation 10). When this occurs the material deforms plastically with an effective viscosity defined by equation (14). The contours in figure 4.4 indicate regions where the yield stress is surpassed and the material is deforming plastically. Also note the shear zones bounding the orogen.

Figure 4.5 shows the Lagrangian mesh that is used to track particles through the orogen. To determine temperature histories, Lagrangian mesh nodes at the surface are tracked back through model time (figure 4.6). There are two distinct categories of particle paths seen in the models that I refer to as frontally accreted and over-thrust particles. Frontally accreted particles begin far from the orogen, approach near the convergence velocity and are then brought to some depth and rapidly exhumed. Over-thrust particles begin near the center of the orogen, are over thrust by frontally accreted material and are exhumed much more slowly than frontally accreted material as is evident in both their particle paths and temperature histories (figure 4.6b,c).

Mg4 shows the expected behavior of a rapidly eroding convergent orogen. At approximately 4 My the orogen width, maximum elevation and erosion rate averaged over the orogen are constant with time (figure 4.7). On the scale of the entire orogen, this observation suggests that the orogen has reached a topographic steady state (Willett and Brandon, 2002). However, the slight increase in erosion rate averaged over the retro side of the orogen indicates that the retro slope steepens with time and that the orogen is not in a perfect topographic steady state on a smaller scale.

The temperature histories shown in figure 4.6 are also used to predict thermochronometry ages. The histories shown are held at a fixed temperature for 50 My prior to recording the temperature histories determined with the model. As is evident from the patterns of predicted ages (figure 4.8a), the padding spreads the predicted ages over a large range but clusters them into two groups easily identified as reset (ages near 60 My) and unreset (ages near 1 My). There are a few ages between these groups that are partially reset. These ages are partially reset from remaining near the partial retention zone for the thermochronometer during their initial isothermal holding padded and not because of orogenic heating. To filter out these partially reset samples I define (U-Th)/He, AFT and ZFT reset ages as ages less than 2.0, 3.0 and 6.0 My respectively. These age limits are then used to delineate reset zones across the orogen (figure 4.8b). Varying these limits within reason, on the order of a few million years, has no effect on the size of the reset zones. The constant width of the reset zones (figure 4.8b) and the relatively constant ages (figure 4.8c) show that the orogen reaches an exhumational steady state (Willett and Brandon, 2002) for all three thermochronometers by 7.5 My.

4.5.2 Effect of Variation in Erosion Rates

By varying the valley erosion factor, the effects of higher and lower erosion rates can be seen in the orogen dimensions and thermochronometer ages. Model Mg3 has a valley erosion factor of 7.0 compared to 4.5 in model Mg4 (table 4.3). The higher erosion factor increases erosion rates by approximately 1 mm/yr (figure 4.9a). The higher erosion rates also reduce the steady-state maximum elevation by 800 m and reduce the steady-state orogen width by 10-15 km allowing the orogen to reach a topographic steady state by 2 My, half the time taken by model Mg4. The higher erosion rates have little effect on the particle paths and maximum temperatures (figure 4.9b) compared to model Mg4 (figure 4.6). However, the higher erosion rates lead to faster exhumation and younger reset ages in Mg3 (figure 4.9b,c). The reset zones of model Mg3 (figure 4.9c) are actually somewhat narrower than Mg4 (figure 4.8) since the orogen itself is narrower.

Decreasing the valley erosion factor to 2.0 in model Mg5 (table 4.3) has the opposite effect, raising the erosion factor in Mg3 compared to Mg4. The erosion rates are 2 mm/yr less than Mg4 resulting in an orogen that does not reach a topographic steady state as is evident from the increasing orogen width and maximum elevation (figure 4.10a). Again, there is little effect on the particle paths, but the particles do experience a much slower exhumation (figure 4.10b) than in model Mg4 (figure 4.6b,c). Correspondingly, the reset ages of Mg5 (figure 4.10c) are .25-2 My younger than in Mg4 (figure 4.8) depending on the thermochronometer. Finally, because the orogen never reaches a topographic steady state, the reset zones do not stabilize to a constant with (figure 4.10c).

4.5.3 Effect of Underplating

Model Mg7 is identical to Mg4 but with 15% of accreted material coming from underplating. The mechanical model thickness in Mg7 is scaled to 8.5 km from the 10 km of model Mg4 (table 4.3) to account for the underplating flux as described above (equation 17). The addition of underplating does not drastically change the maximum elevation of the orogen, the orogen width or the average erosion rates (figure 4.11a). The main effect of underplating in this case is to exhume particles from below the boundary of the mechanical model where they experience higher temperatures (figure 4.11b) than in model Mg4 (figure 4.6b,c). The higher temperatures reached by the particles change the ZFT ages slightly but not the AFT or He ages (figure 4.11b,c). The AFT and HE ages are unaffected because the position of the near surface closure isotherms of these thermochronometers are not altered by the underplating.

Increasing the width of the underplating zone from 37 to 76 km in model Mg9 also has little effect on the maximum elevations of the orogen (figure 4.12a), compared to Mg4 (figure 4.7). However, the more extensive underplating does increase the orogen width and decrease the erosion rate. The increased width and lower erosion rates are expected since the underplating zone extends beyond the orogen bounds and the erosion rates are averaged over this wider zone (figure 4.12b) while there is little change in the relief (figure 4.7). The wider zone of underplating does result in some particles reaching higher temperatures earlier in their history (figure 4.12c) than in the narrow zone of underplating (figure 4.11c), but this earlier heating has little affect on the thermochronometer ages or reset zones.

Model Mg14 is identical to Mg7, but the amount of accreted material due to underplating is increased to 50% (table 4.3). Because of the increased underplating flux, the scaled crustal thickness is reduced to 5.0 km. The increase in underplating has relatively minor effects on the orogen dimensions and erosion rates (figure 4.13a) compared to the Mg7 (15% underplating, 4.11a). However, the tracked particles reach higher temperatures and cool faster (figure 4.13b) than with 15% underplating (figure 4.11b). The higher temperatures and faster exhumation of Mg14 is apparent in the younger reset ages and wider reset zones (figure 4.13c) when compared to model Mg7 (figure 4.11c).

4.5.4 Effect of Raising Erosion Base Level

In order to investigate an orogen originating as a submarine wedge isolated from fluvial and hillslope erosion, I raise the erosion base level by defining a water depth (d_w) and corresponding sea level below which erosion does not occur (figure 4.1a). In doing so I assume submarine erosion is negligible compared to the rates of accretion and subaerial erosion. Model Mg25 is identical to Mg4 (table 4.3) but has a water depth of 2 km and a valley erosion factor of 12, compared to an erosion factor of 4.5 in Mg4. Since raising the base level delays the onset of erosion and forces the erosion to act over a narrower area, a higher erosion factor is needed to keep the size of the orogen in Mg25 comparable to the orogen in Mg4. Therefore, the maximum elevation, orogen width and average erosion rates of Mg25 (4.14a) are similar to Mg4 (figure 4.7). However, the raised base level makes it difficult for the orogen to achieve a balance between the accretionary and erosive flux, and the orogen does not reach a topographic steady state in 10 Ma (figure 1.14a).

Despite the similar surface dimensions, the orogen in Mg25 (figure 4.14b) is significantly larger than the orogen in Mg4 (4.6b). The increase in thickness leads to an increase in the radiogenic heating and a hotter orogen (figure 4.15) compared to Mg4 (figure 4.5). Although the warmer orogen of Mg25 (figure 4.14b) does not lead to higher peak temperatures compared to Mg4 (figure 4.6c), more particles exposed at the surface in Mg25 reach high temperatures and stay at these high temperatures for longer durations. These changes to the particle paths and temperature histories when compared to Mg4 leads to Mg25 having significantly wider reset zones after approximately 3-4 My of convergence (figure 4.14c, 4.8).

4.5.5 Effect of Detachment

Model Mg18 investigates the effects of a weak layer at the base of the mechanical model. This layer can be viewed in one of two ways. If the mechanical model represents the entire crust, the layer is the strength discontinuity at the Moho (Kohlstedt et al., 1995). However, if the mechanical model represents an upper section of crust, the weak layer represents a detachment or decollement. In this study I use the interpretation of the weak layer as a crustal detachment. The weak layer is imposed as a reduction in the internal angle of friction along the base of the model from the S point to the pro edge of the model. Model Mg18 is identical to Mg4 except that the internal angle of friction of the weak layer is lowered from 15° to 5°. The detachment causes a partial decoupling between the orogen and the moving substrate allowing deformation to radiate farther from the S point and create a much wider orogen (figure 14.16a) than seen in Mg4 (figure 4.7). The erosion rates for Mg18 are approximately 3-4 mm/yr less than in Mg4 since the models have similar relief but Mg25 is up to twice as wide. The more extensive deformation and erosion combined with the partial decoupling of the orogen from the subducting substrate leads to a wider thermal anomaly and slower cooling of particles moving through the anomaly (figure 4.16b) than seen in Mg4 (figure 4.6b). Finally, the wider orogen combined with the more slowly cooled particles leads to older reset ages and more extensive reset zones (figure 4.16c) than in model Mg4 (figure 4.8).

4.6 Summary

A wide range of models is presented above (figure 4.6-4.16) showing the effects of varying specific model parameters (table 4.3) on the orogen dimensions, temperature histories and patterns of reset ages. Raising the erosion factor was shown to increase the erosion rates thereby reducing the orogen width and maximum elevations and lowering the reset ages (figure 4.9). Lowering the erosion factor had the effect of increasing the orogen width and maximum elevation, decreasing the erosion rates and increasing the reset ages (figure 4.10). With 15% of accretion coming from underplating over a narrow zone (37 km wide), there is little change in the orogen dimensions, but tracked particles reach higher temperatures and the ZFT reset zone widens (figure 4.11). With 50% underplating over the same zone the reset zones of all the thermochronometers are widened, and the reset ages are younger (figure 4.13). With 15% underplating over a wider zone (76 km wide) the orogen also widens but there is little effect on the reset zones or ages (figure 4.12). The most important effect of increasing the erosion base level is that it allows particles to reach higher temperatures and cool more slowly (figure 4.14). Because of these changes to the temperature histories, an orogen of similar surface dimensions to one without a sea level has significantly wider reset zones. Finally, through imposing a weak detachment at the base of the model, there is a decoupling between the orogen and the subducting plate that allows for a broader zone of deformation on the pro side of the model and wider reset zones (figure 4.16).

Parameter	Description	Value
Mechanical Model		
v_c	Convergence velocity	50 mm/yr
c	Cohesion	1000 Pa
μ_{min}	Minimum viscosity	1500 Pa s
T_{ref}	Reference temp for μ_{min}	1000 °C
Q	Activation energy	130,000 J/mol
ρ_c	Density of crustal material	2800 kg/m^3
ρ_l	Density of subducting lithosphere	3200 kg/m^3
k_r	Ridge erosion factor	.04
n	Exponent of ridge erosion law	2.0
Thermal Model		
$k_{c,l,a}$	Thermal conductivity of crust, lithosphere and asthenosphere (eqn. 11)	2.0, 2.0. 50.0 w/(m °K)
c	Specific heat	1000 J/(kg °K)
θ	Slab dip	35°
h_{lith}	Thickness of the lithosphere	50 km
T_s	Surface temperature	0 °C
t_{runup}	Duration of thermal model run-up	20 My
Thermochronometry Models		
D_0	He diffusivity at infinite temperature	50.0 x 10^8 $\mu m^2/s$
E_a	Activation energy for He diffusion	33.0 kcal/mol
U_c	^{238}U concentration	13.0 ppm
Th_c	^{232}Th concentration	27 ppm
a	Diffusion domain radius	42.5 μm
B	Material constant for ZFT	3.160×10^{-22} My
$\bar{E}_z$	Average activation energy for ZFT	49.77 kcal/mol

Table 4.1: Parameters constant for all models.

Parameter	Description
Mechanical Model	
v_{up}	Underplating velocity
u_{beg}	Beginning of underplating
h_o	Initial crustal thickness. Actual thickness will vary with the amount of underplating
h_s	Crustal thickness scaled for underplating
φ	Internal angle of friction
k_v	Valley erosion factor
d_w	Water depth used in defining sea level
Thermal Model	
A	Heat production, only defined in crust
T_a	Basal / asthenosphere temperature
Thermochronometry Models	
D_{par}	Kinetic annealing parameter for AFT

Table 4.2: Parameters allowed to vary in models and calibrated to the Taiwan orogen (section 6).

Model	Mg4	Mg3	Mg5	Mg7	Mg9	Mg14	Mg18	Mg25
% Underplating	0	0	0	15	15	50	0	0
Width of Underplating Zone (km)	NA	NA	NA	37	76	37	NA	NA
v_{up} (m/My)	NA	NA	NA	2050	1000	6850	NA	NA
Crustal Thickness, h_s (km)	10	10	10	8.5	8.5	5.0	10	10
k_v	4.5	7.0	2.0	4.5	4.5	4.5	4.5	12
d_w (m)	0	0	0	0	0	0	0	2000
φ (°)	15	15	15	15	15	15	15 with basal detachment at 5	15

Table 4.3: Parameters used in the first suite of models.

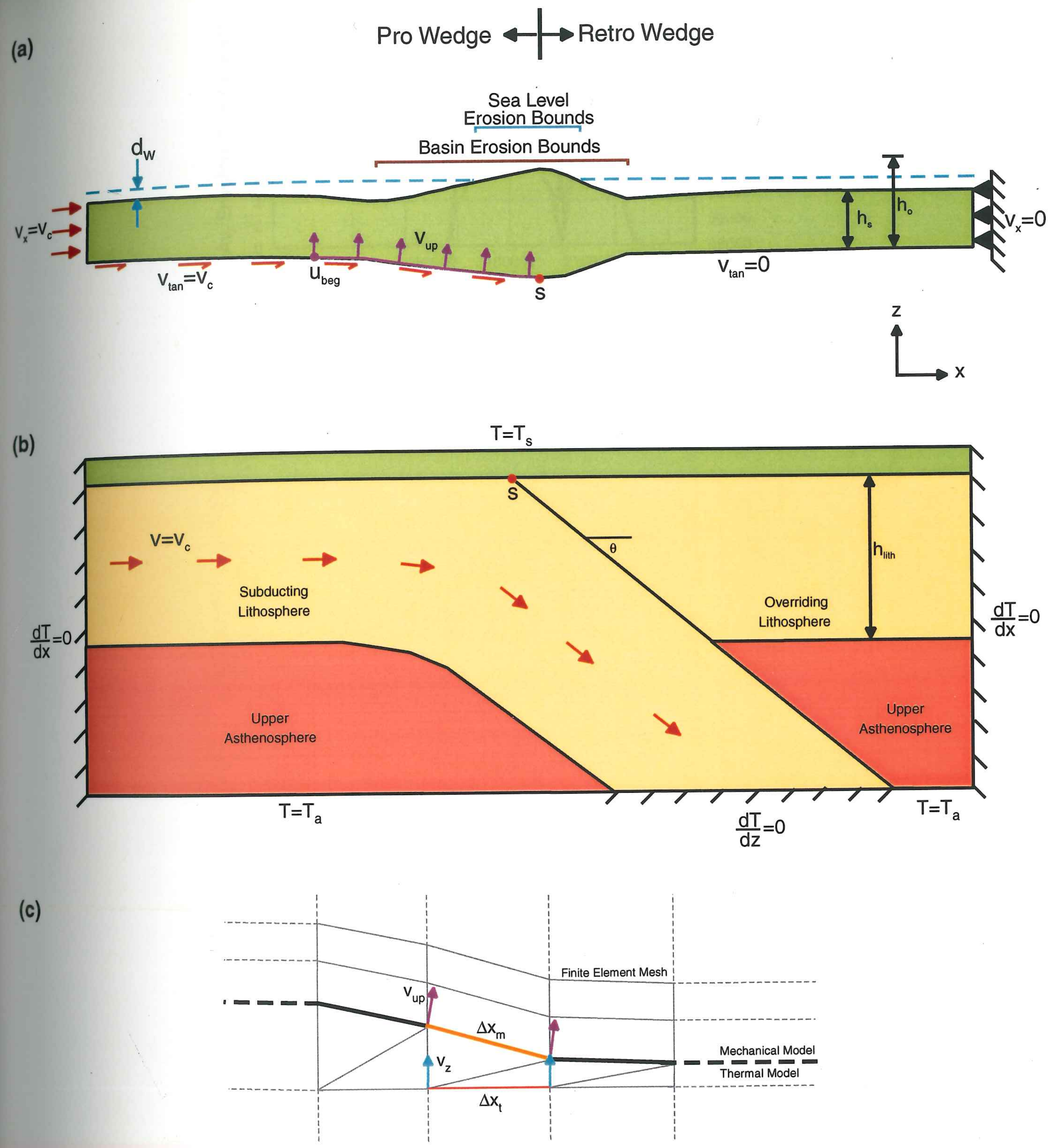

Figure 4.1: Model domains and boundary conditions for the (a) mechanical and (b) thermal models. (c) Diagram of the finite element mesh at the boundary of the mechanical and thermal model. When there is underplating, the velocity field of the thermal model is augmented by v_z (eqn. 20) to conserve mass and heat between the mechanical and thermal domains.

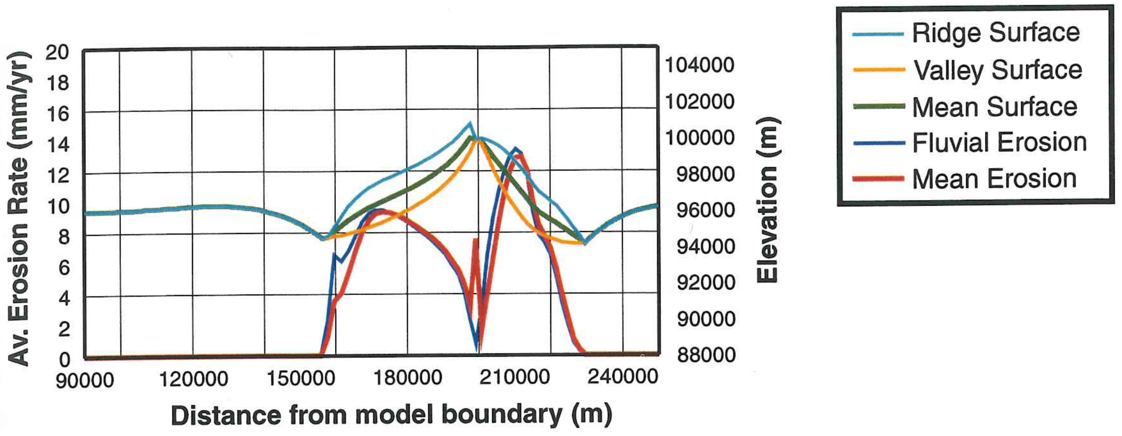

Figure 4.2: Surface profiles for the valley, ridge and mean surfaces plotted with the fluvial and mean erosion rate across the orogen for model Mg4.

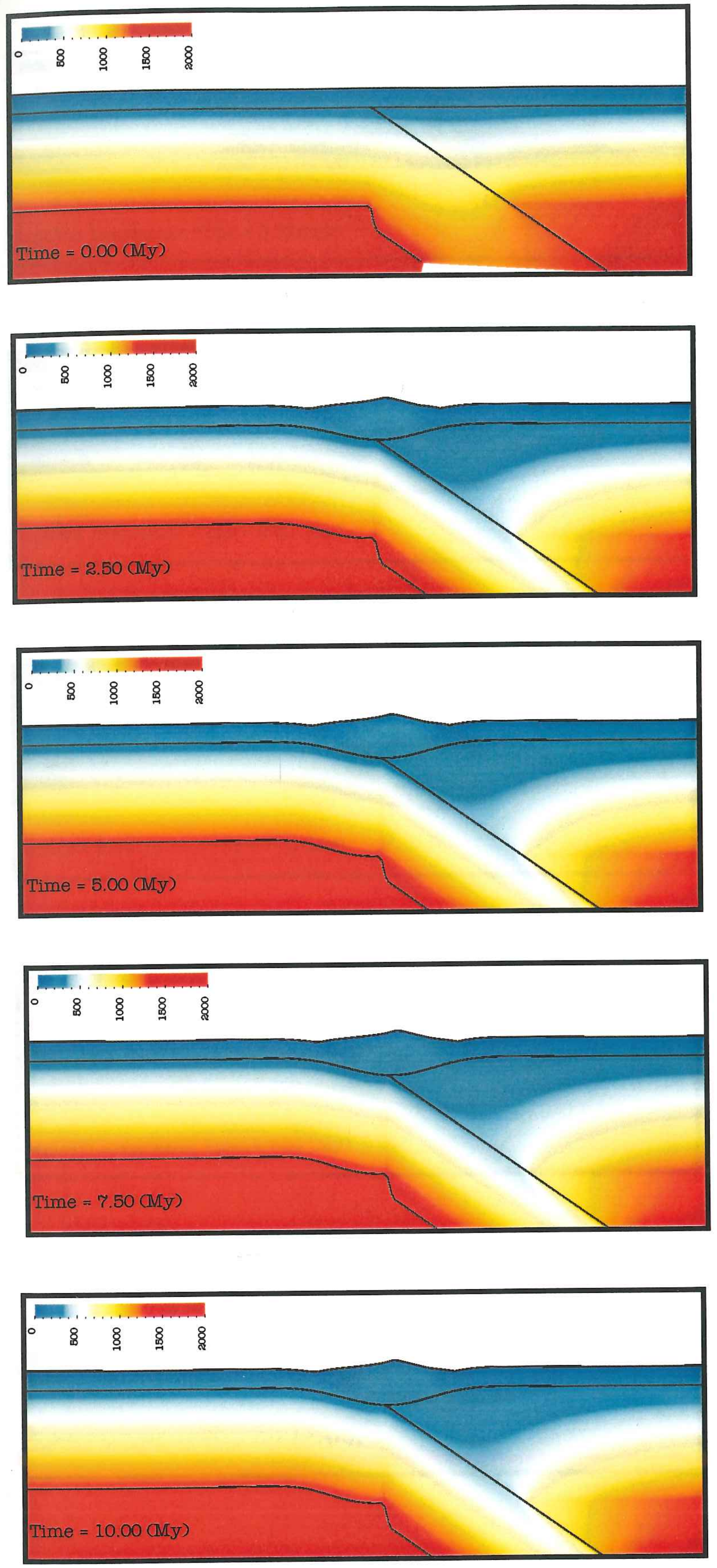

Figure 4.3: Temperature field (°C) for model Mg4. The mechanical model boundary and lithosphere-asthenosphere contact are indicated with lines. The elapsed time between frame 1 and 2 is the indicated time plus the thermal run-up time (20 My).

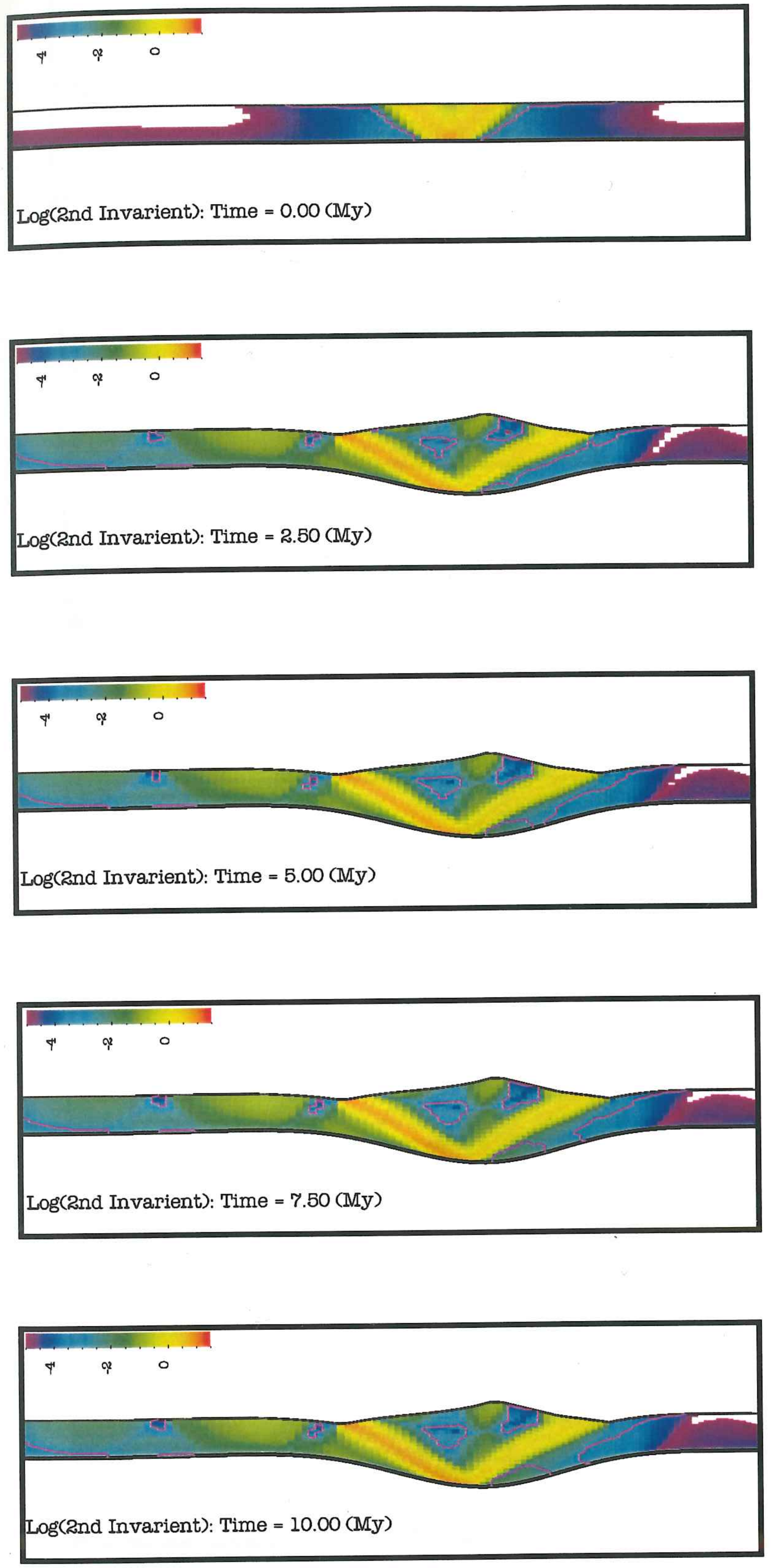

Figure 4.4: Log of the second invariant of the strain rate for model Mg4. The purple lines indicate regions of plastic failure. For reference, the model edges are not above the Coulomb yield stress. White space represents values < -5.0.

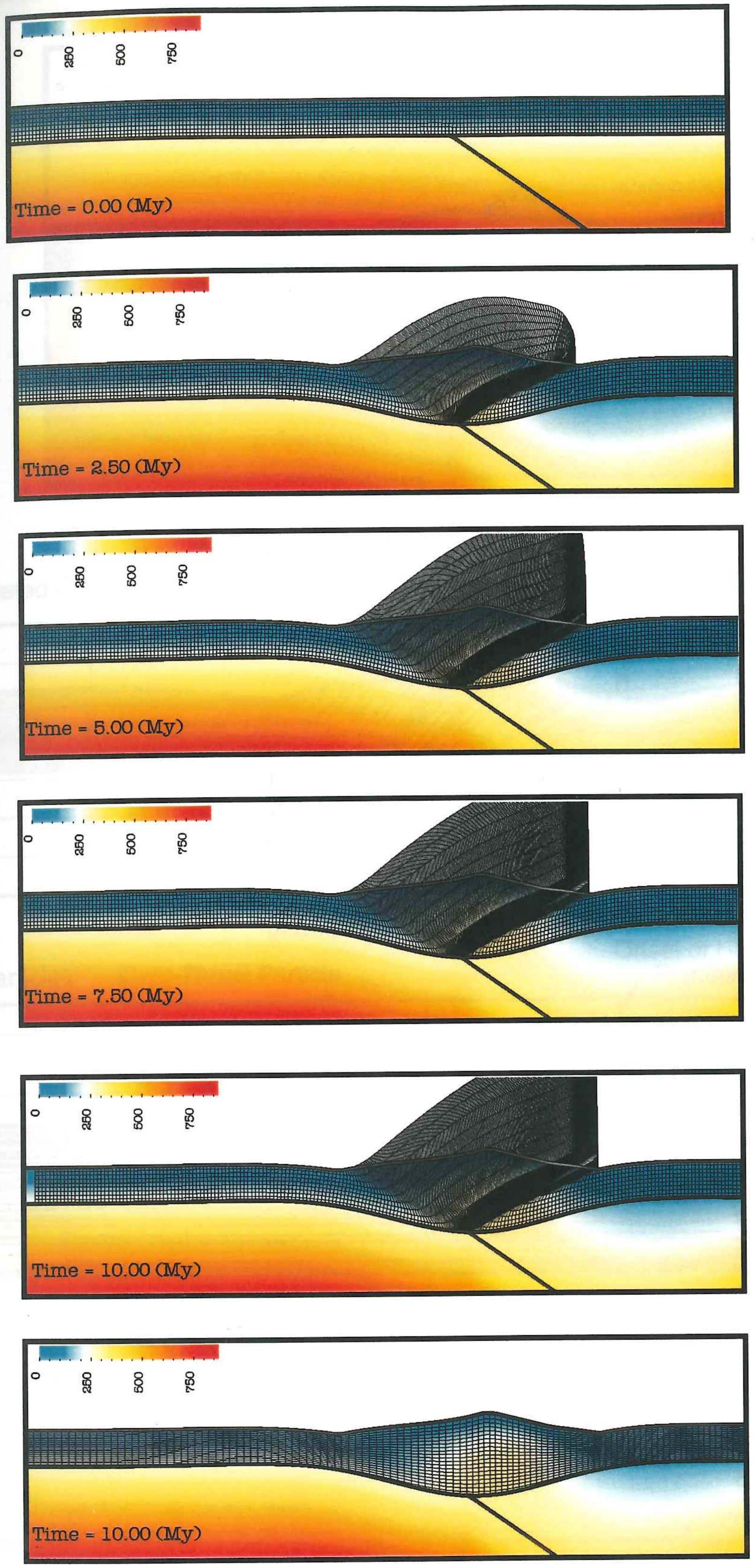

Figure 4.5: Temperature field (˚C) and Lagrangian mesh used for particle tracking in model Mg4. The Eulerian mesh used in calculating the velocity solution is shown in the last frame. Portions of the Lagrangian mesh above the model surface represents material that has been eroded. Note the advection of heat into the orogen due to erosion. The elapsed time between frame 1 and 2 is the inidcated time plus the thermal run-up time.

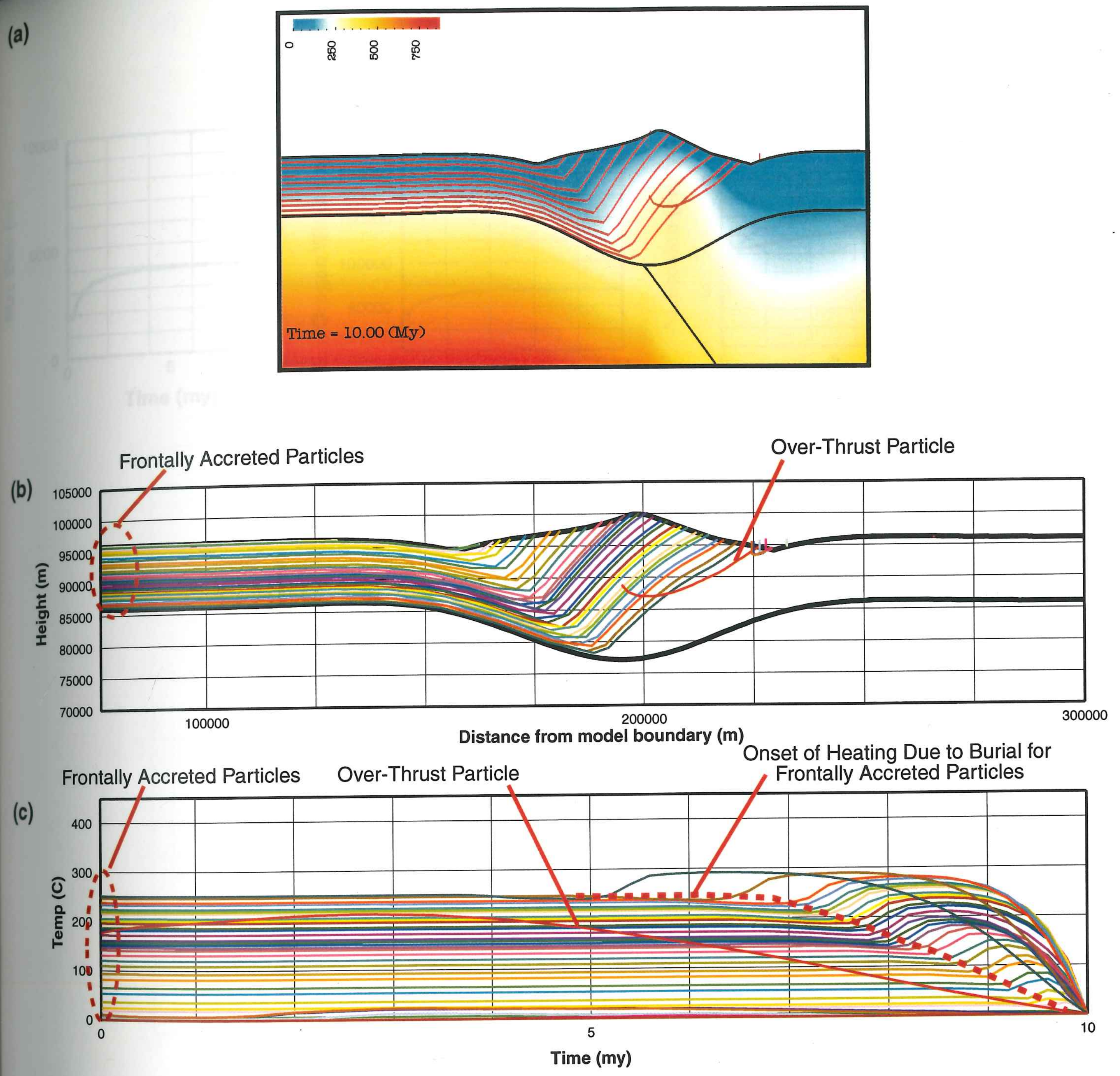

Figure 4.6: (a) Subset of tracked particles for model Mg4 at 10 My and the temperature field with 2x vertical exageration. All subsequent plots of tracked material in this section come from 10 My. (b) All of the tracked particles at 10 My and (c) their corresponding temperature histories. Frontally accreted particles are accreted into the orogen while over-thrust particles begin inside the orogen and experience a slower burial and exhumation. The two types of particle paths have distinct thermal histories reflecting the different rates of burial and

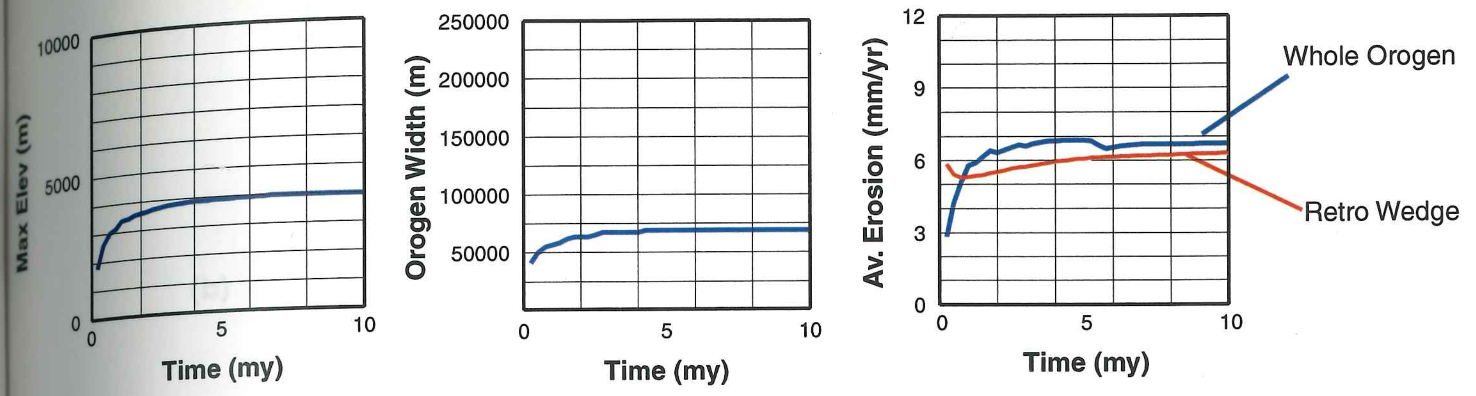

Figure 4.7: Orogen dimensions and erosion rates through time for model Mg4. Erosion rates are averaged over the whole orogen (blue line) and the retro side (red line). The constant nature of the width, peak elevation and erosion rates over the entire orogen suggest that the model has reached a topographic steady state after ~ 4 My.

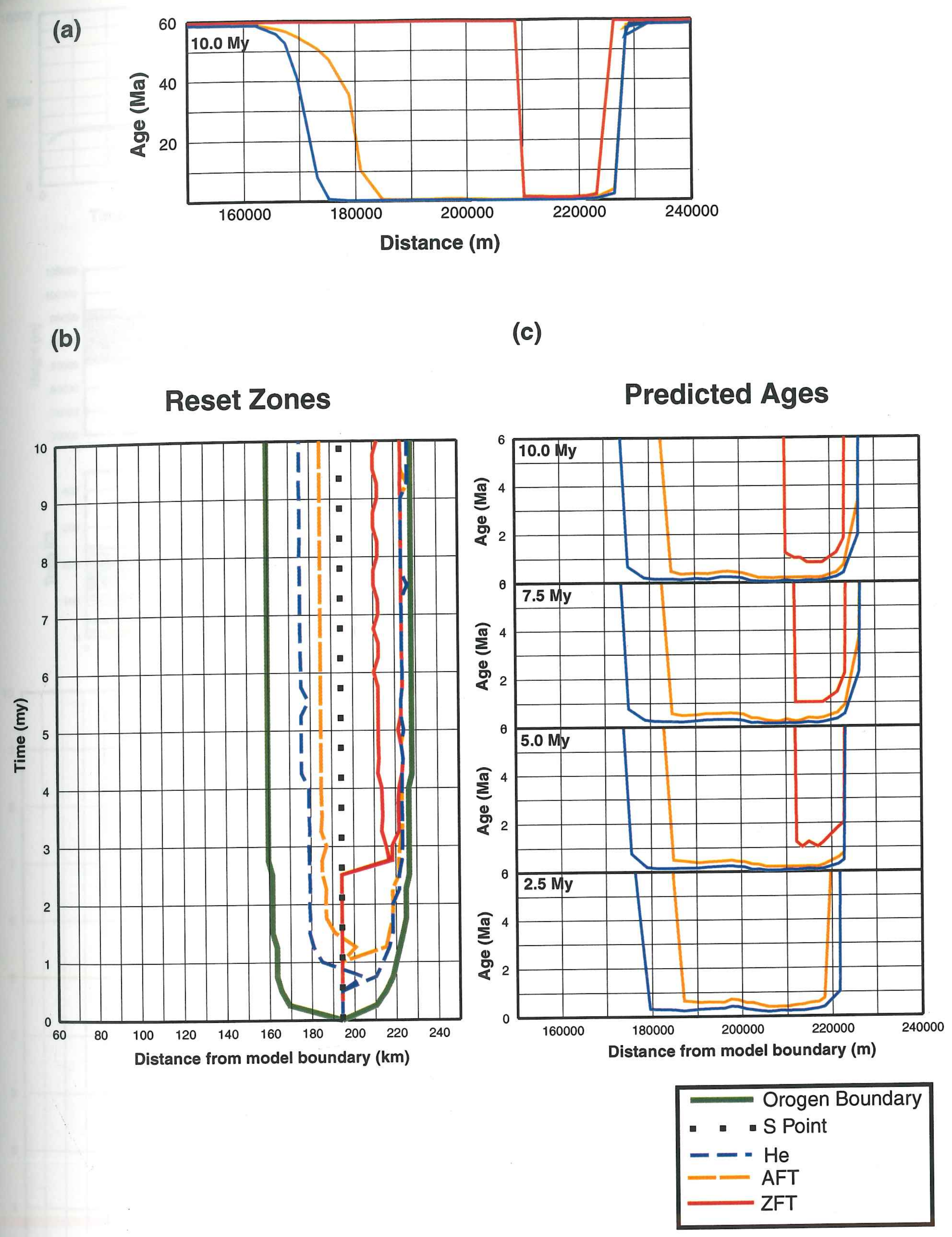

Figure 4.8: (a) Predicted (U-Th)/He, AFT and ZFT ages at the surface of model Mg4 after 10 My. (b) Zones of reset ages plotted with the orogen width and location of subduction boundary. Reset zones are defined as ages less than 2.0, 3.0 and 6.0 My for (U-Th)/He, AFT and ZFT dating respectively. (c) Evolution of reset ages through time. Note the similarity of (c) to figure 2.3 and that all thermochronometers have reached an exhumational steady state by approximately 5 My.

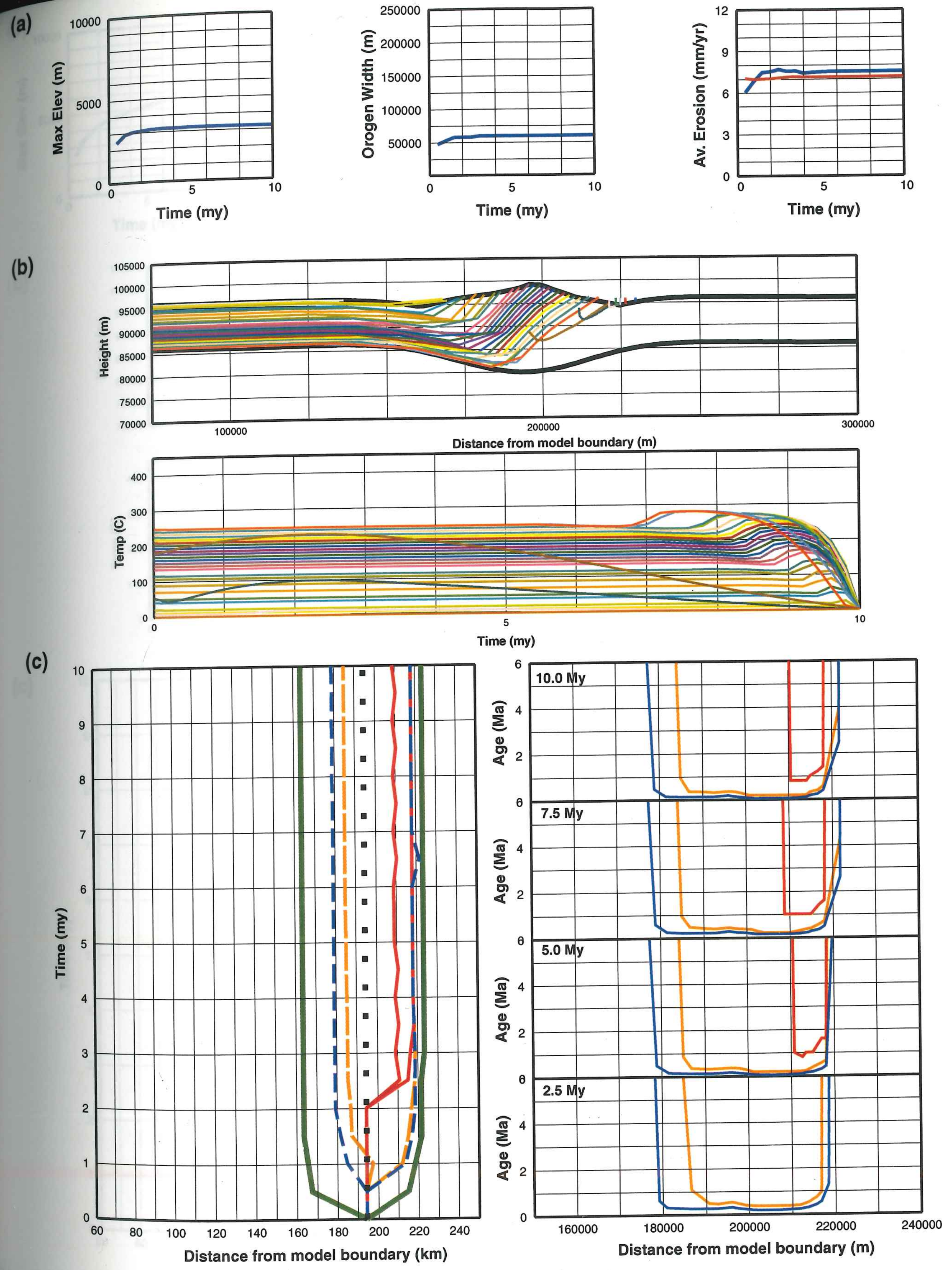

Figure 4.9: Results of model Mg3 with a valley erosion factor of 7.0 (2.5 higher than Mg4). (a) The raised erosion factor results in higher erosion rates that lead to lower elevations and a narrower orogen. (b) While there is little effect on the particle paths, the temperature histories show that material is exhumed much faster than in model Mg4 (fgure 4.6c). (c) The reduction in orogen width also reduces the width of the reset zones, and the faster exhumation leads to younger reset ages.

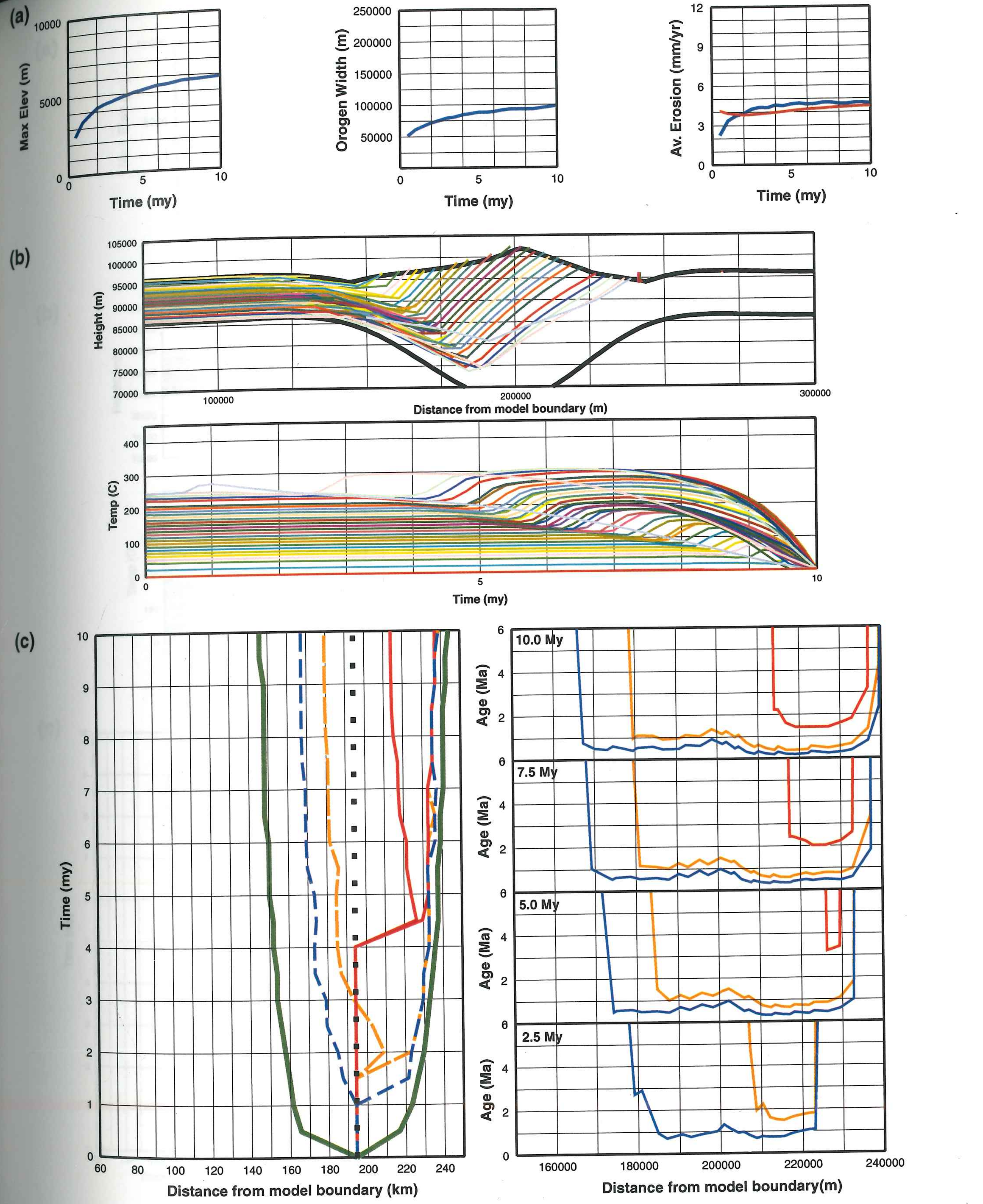

Figure 4.10: Results of model Mg5 with a valley erosion factor of 2.0. The lower erosion rates resulting from the lower erosion factor lead to the development of an orogen that does not reach a topographic steady state (a). The lower erosion rates also lead to the slower cooling of particles exposed at the surface (b) and younger reset ages (c). Because the orogen never reaches a topographic steady state, the reset zones continue to widen (c).

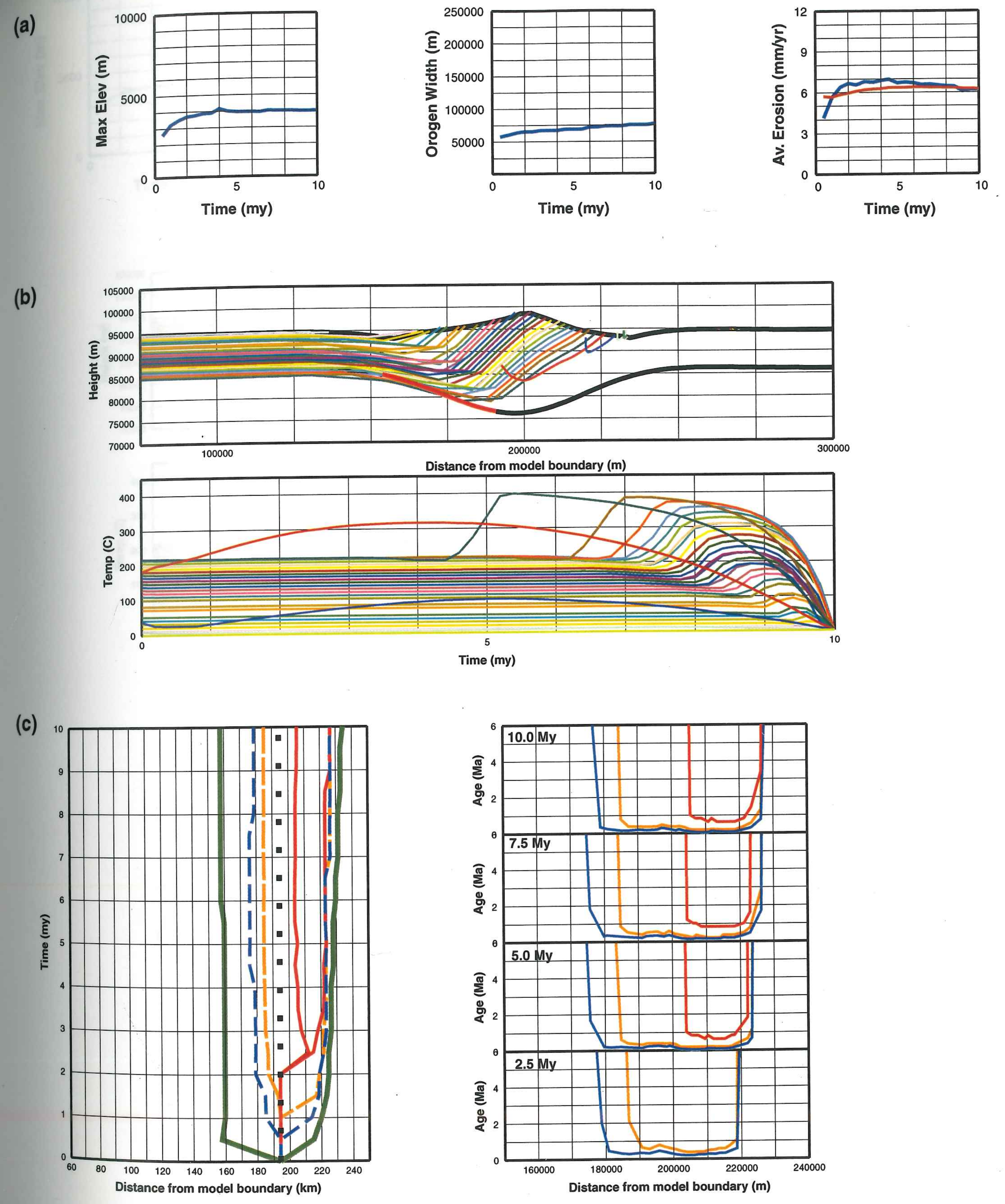

Figure 4.11: Model Mg7, shown here, is identical to Mg4 but with 15% of accreted material coming from underplating in the region indicated with red (b) (table 4.3). (a) The orogen dimensions and erosion rates are relatively unaffected by the underplating when compared to model Mg4 (figure 4.7). (b) The underplating exhumes particles from significantly higher temperatures than in Mg4 (figure 4.6b), but the increased temperatures only slightly change the pattern of ZFT ages and have almost no effect on the other thermochronometers (c).

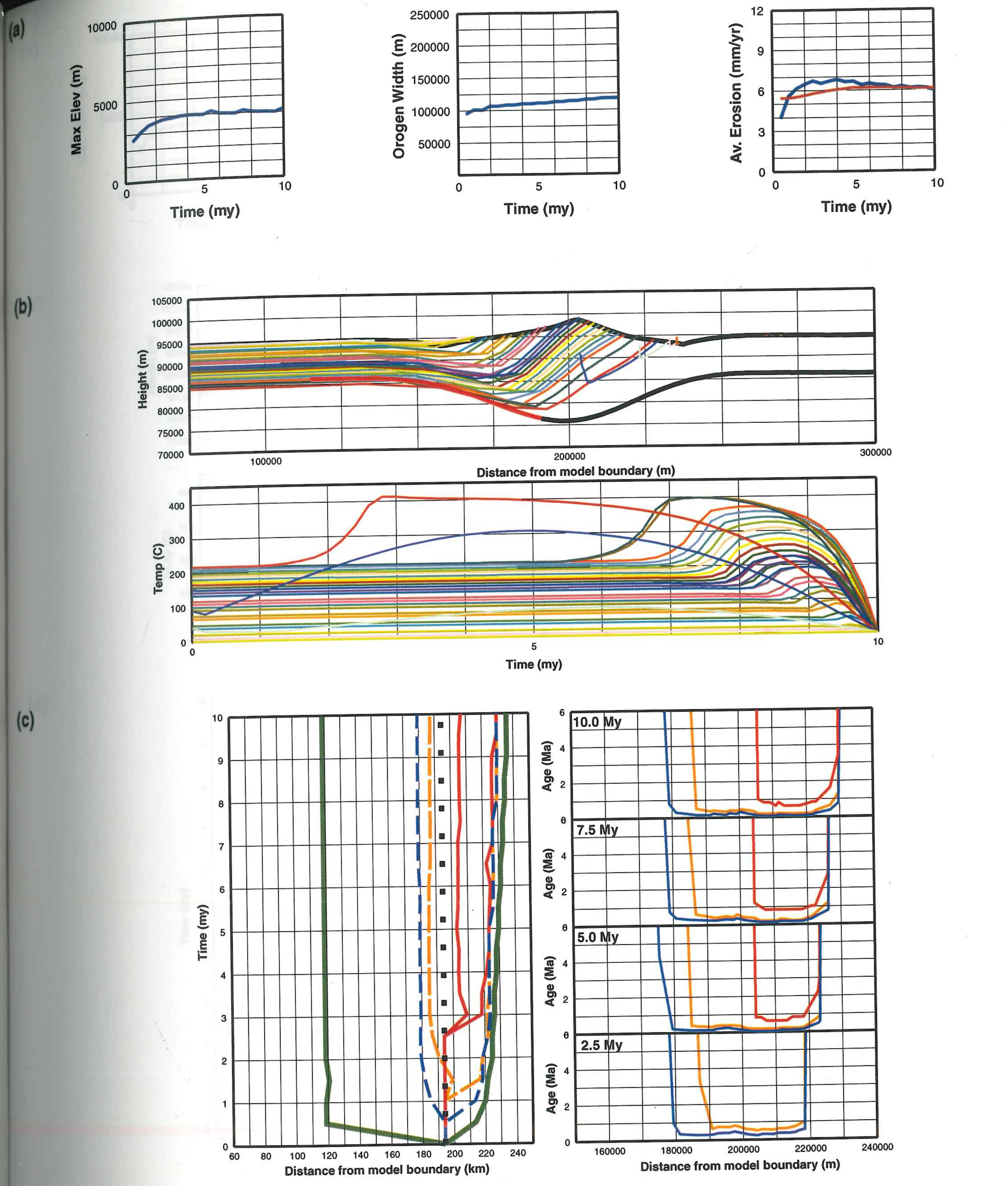

Figure 4.12: Model Mg9 (shown here) is identical to Mg7 but has the 15% underplating occuring over a broader zone (b). (a) The more extensive underplating has little effect on the maximum elevations but does widen the orogen and lower the erosion rates. (b) Some particles are heated earlier in their history when compared to a narrow zone of underplating (Mg7, figure 4.11b), but the earlier heating has little effect on the reset zones and ages (c).

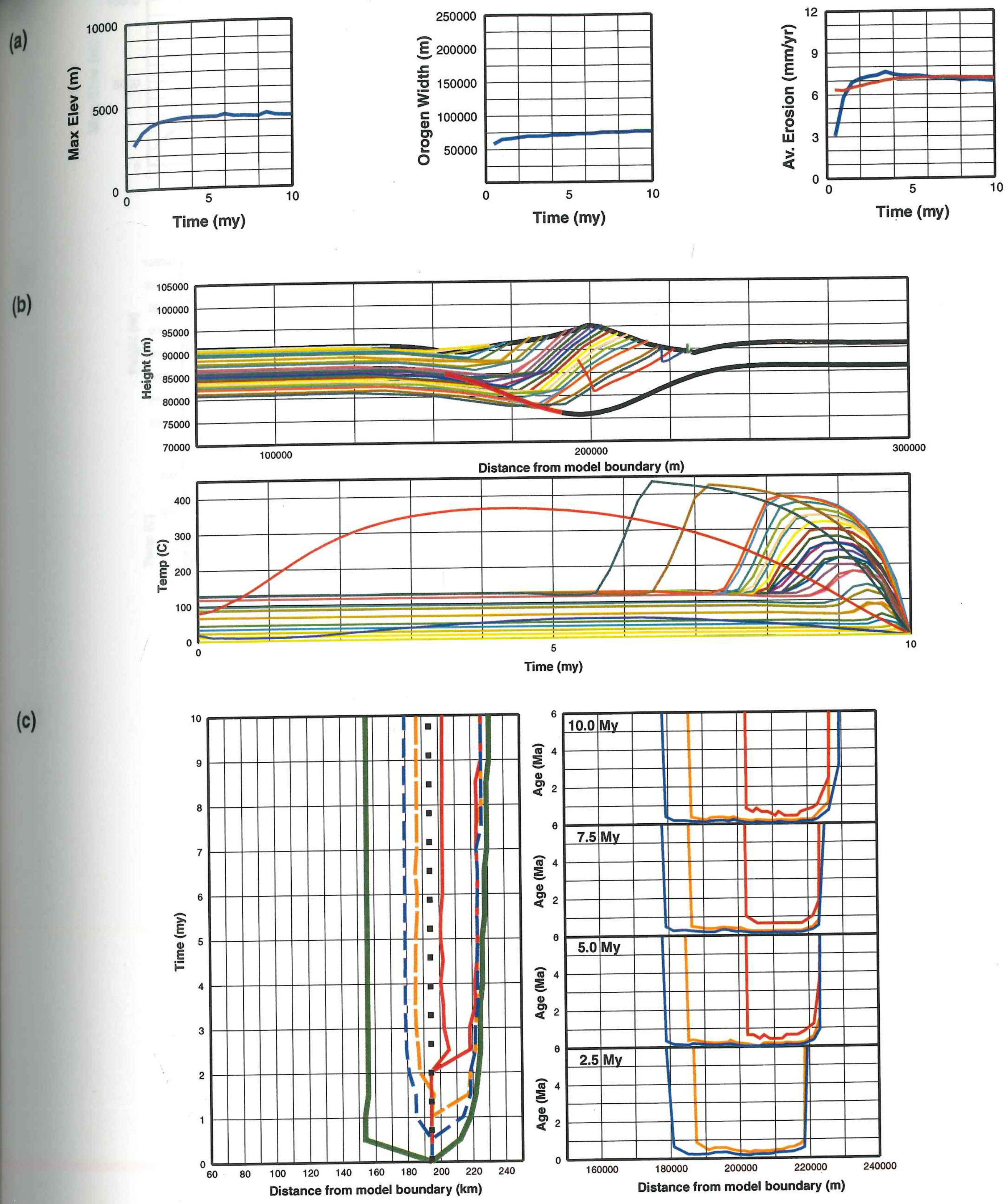

Figure 4.13: Model Mg14 (shown here) is identical to Mg7 but with 50% underplating. As with Mg7 (figure 4.11a) the underplating has little effect on the orogen dimensions and erosion rates (a). (b) The increased underplating does result in particles being exhumed from higher temperatures faster. (c) The faster exhumation and higher temperatures are apparent in the wider reset zones and younger reset ages when compared to model Mg7 with 15% underplating (figure 4.11c).

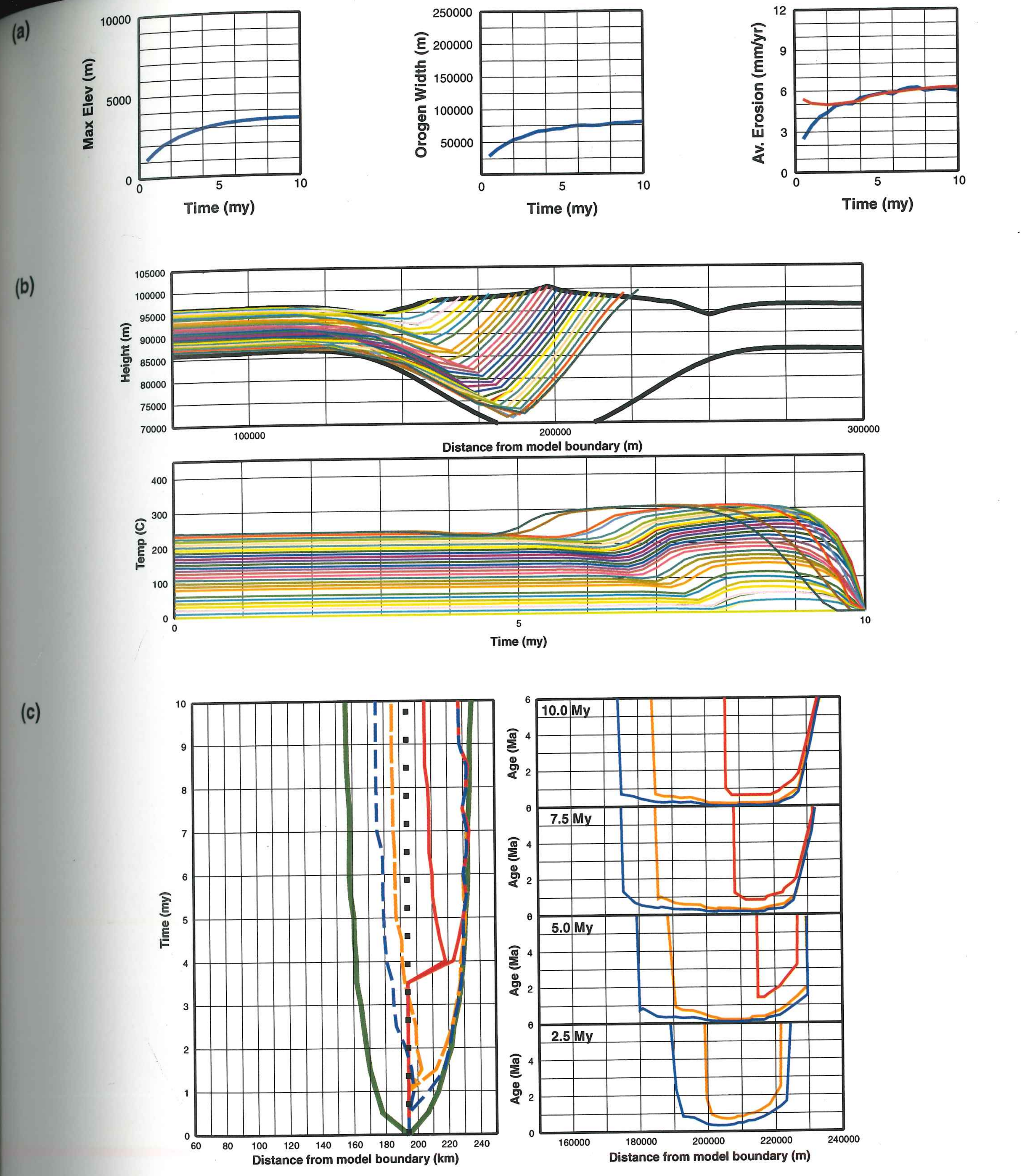

Figure 4.14: Model Mg25 (shown here) is identical to model Mg4 but with a sea level constraint raising the erosion base level 2 km and a higher erosion factor (increased from 4.5 to 12). While the surface dimensions of the orogen (a) are similar to Mg4 (figure 4.7), the orogen in Mg25 (b) is much larger overall (figure 4.6b). The incresed size leads to increased radiogenic heating and particles reaching higher temperatures for longer periods of time (b) (figure 4.6c). (c) The wider reset zones of Mg25 show the effect of the different thermal histories when compared to Mg4 (figure 4.8).

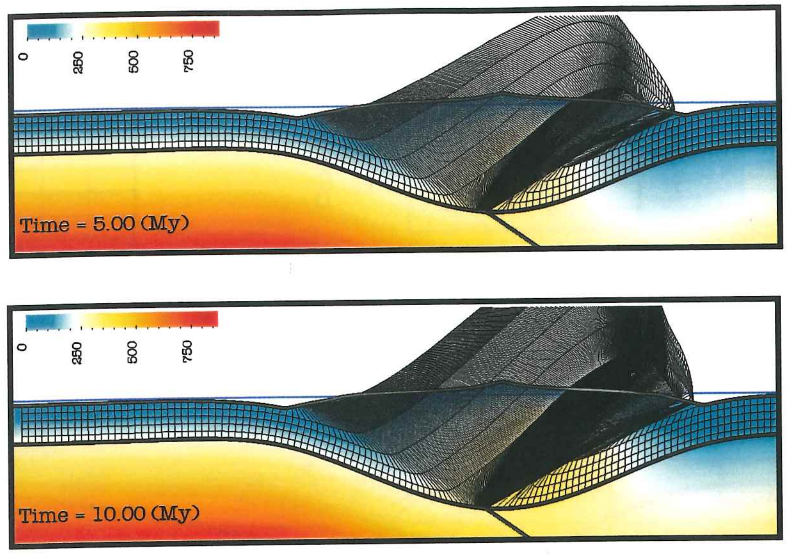

Figure 4.15: Temperature field and Lagrangian mesh for model Mg25. The blue line indicates the sea level below which no erosion occurs. The sea level constraint leads to a larger orogen with increased radiogenic heating and higher temperatures than seen in Mg4 without the constraint (figure 4.15).

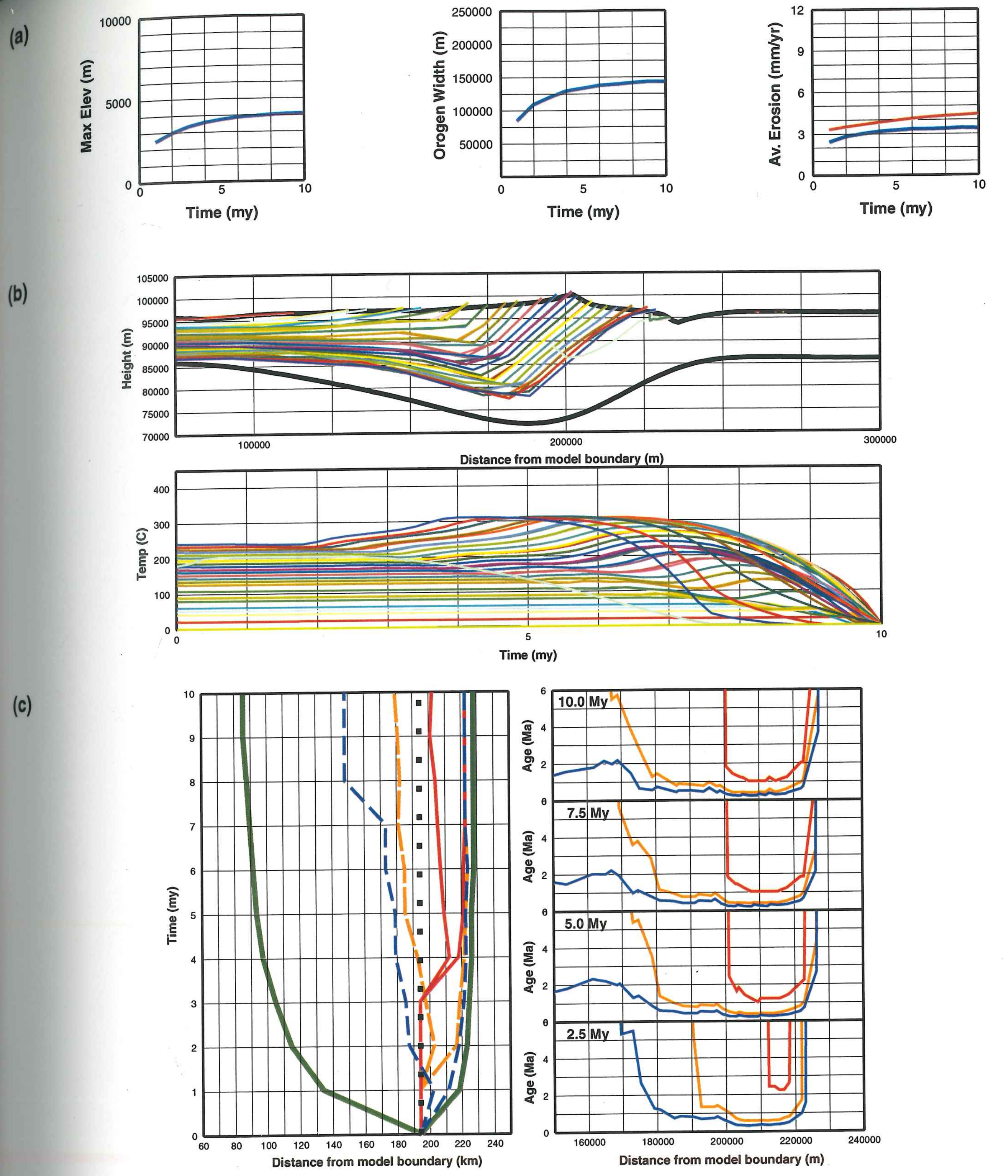

Figure 4.16: Model Mg18 (shown here) is identical to Mg4 but has a weak detachment at the base of the model. (a) The detachment leads to a partial decoupling of the orogen from the subducting substrate and a much wider orogen with lower erosion rates than seen in Mg4 (figure 4.7). The decoupling combined with the wider zone of deformation leads to the slower cooling of paticles (b), wider reset zones and younger reset ages (c) than seen in model Mg4 (figure 4.6c, 4.8).

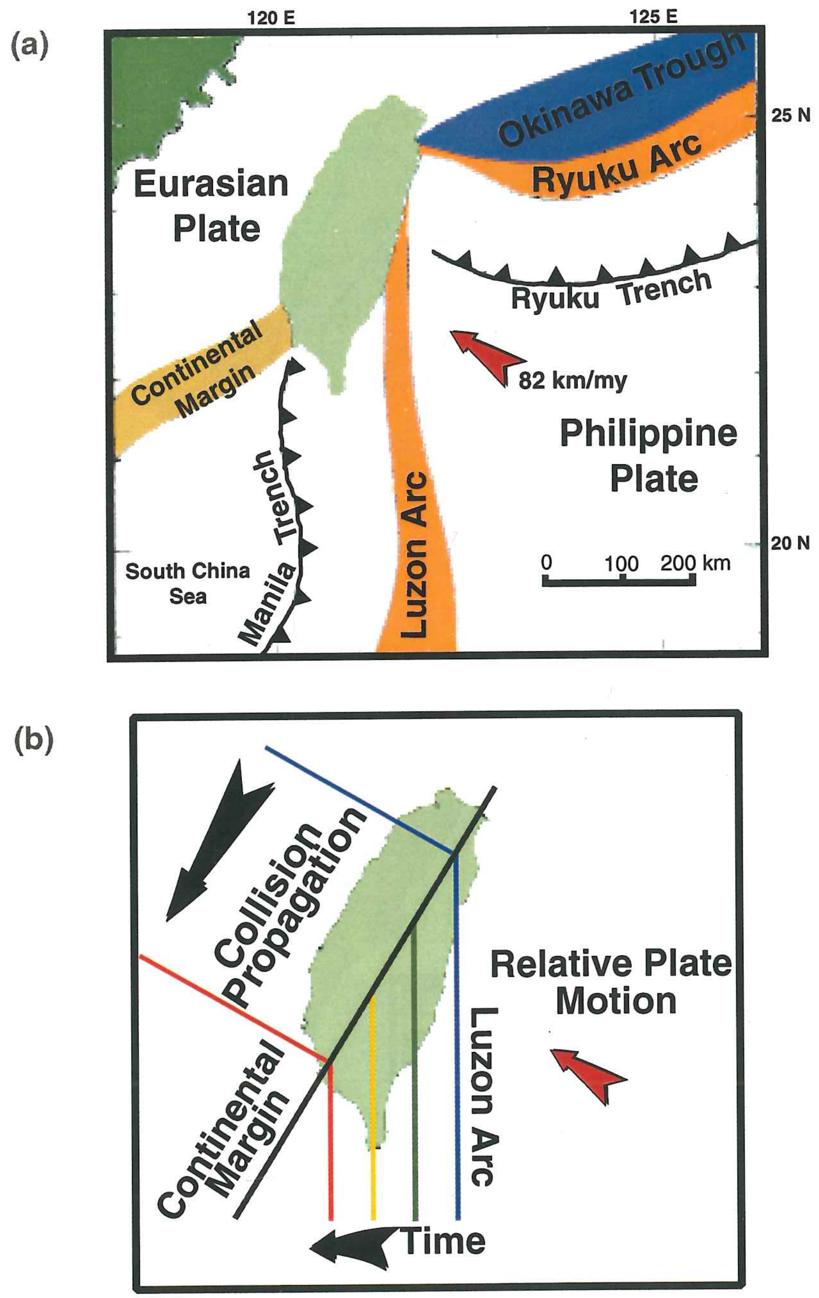

Figure 5.1: (a) General tectonic setting of Taiwan (modified from Barr and Dahlen (1989), and (b) a schematic representation of the southward propagation of collision.

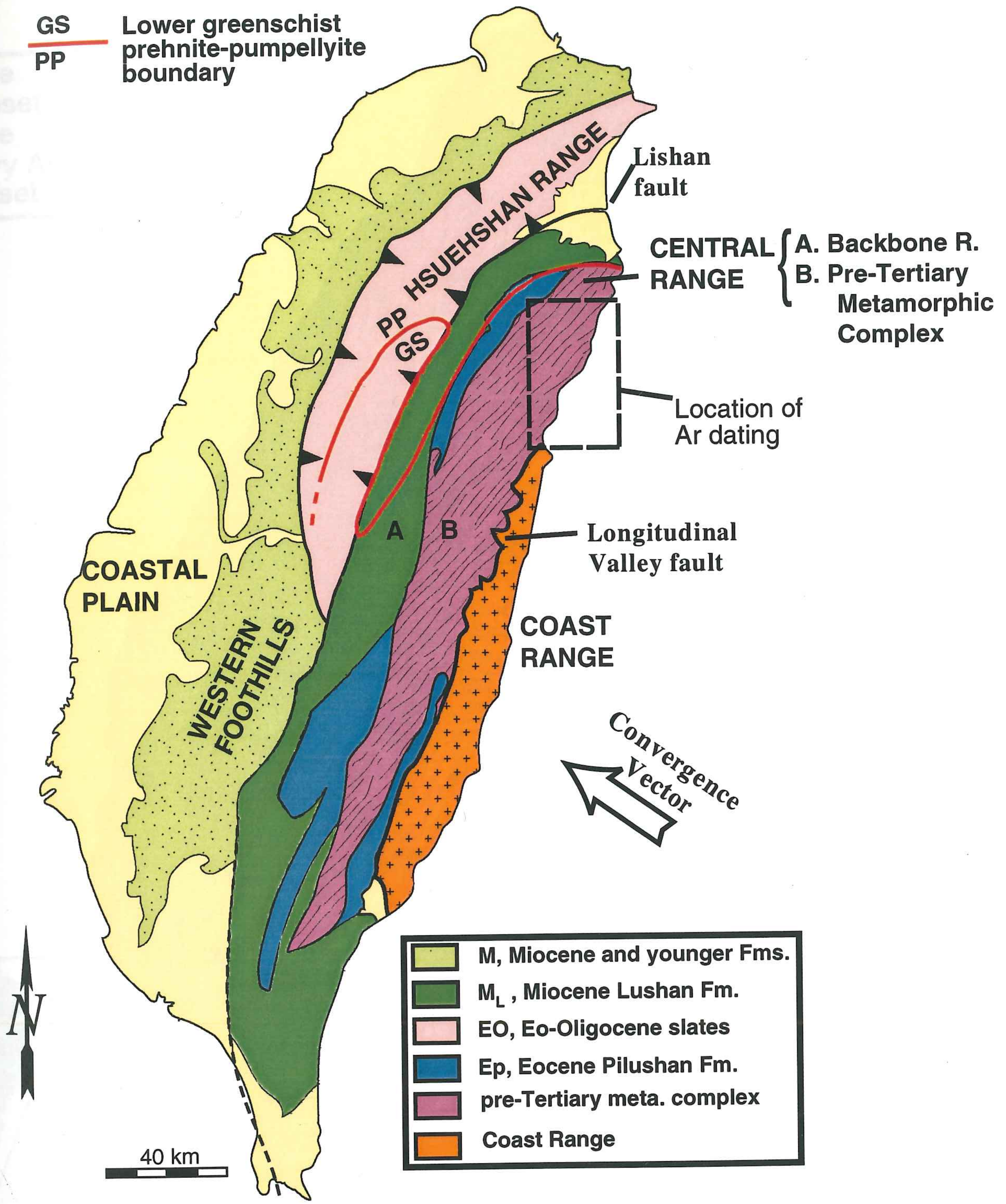

Figure 5.2: Simplified geologic map of Taiwan showing the main tectonostratigraphic units and faults.

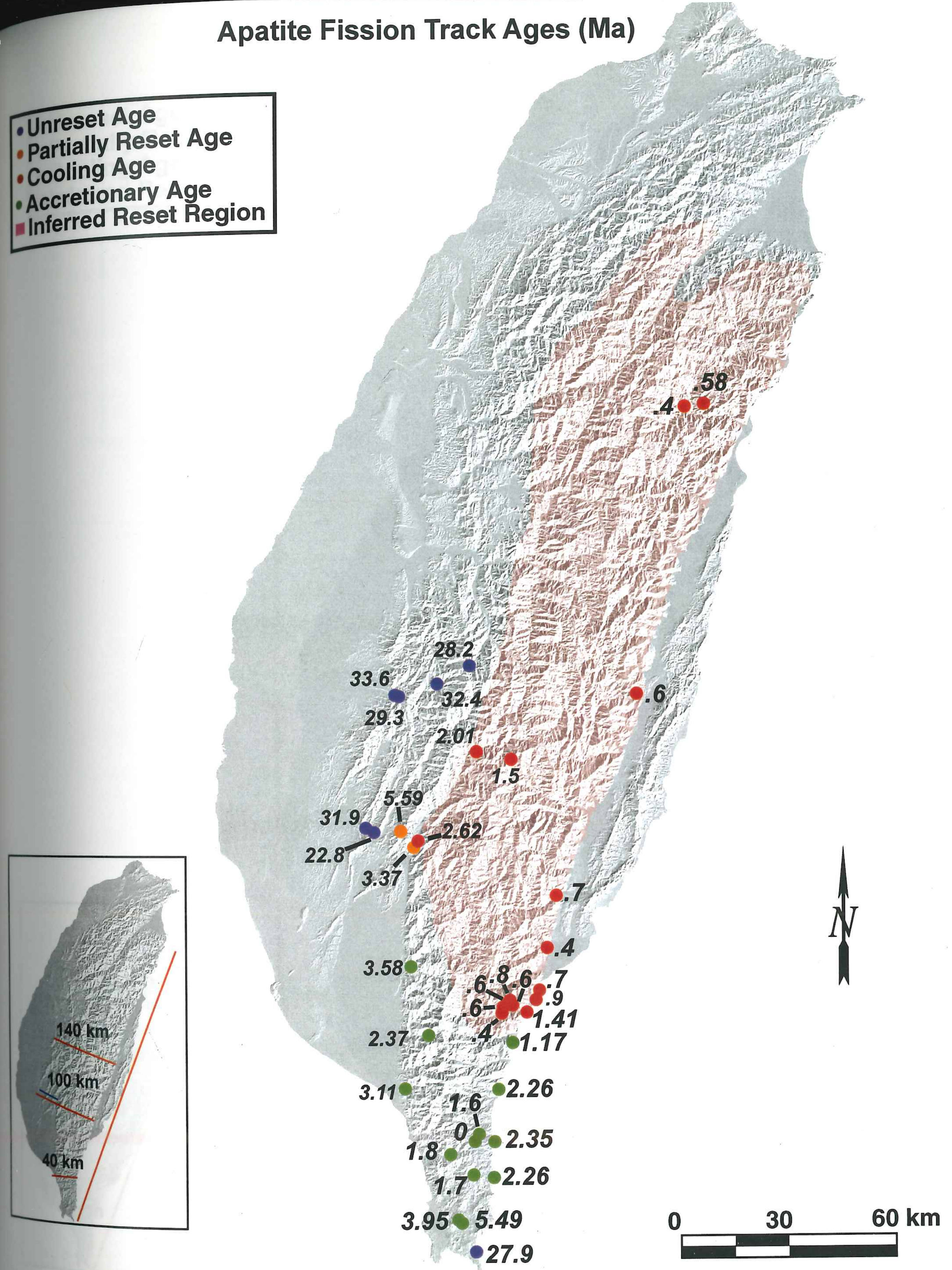

Figure 5.3: Locations and pooled ages of AFT samples used in this study. Inset shows the projections used in figures 5.6 and 5.7 in red and the cross section location of figure 5.9 in blue.

8'/22/5

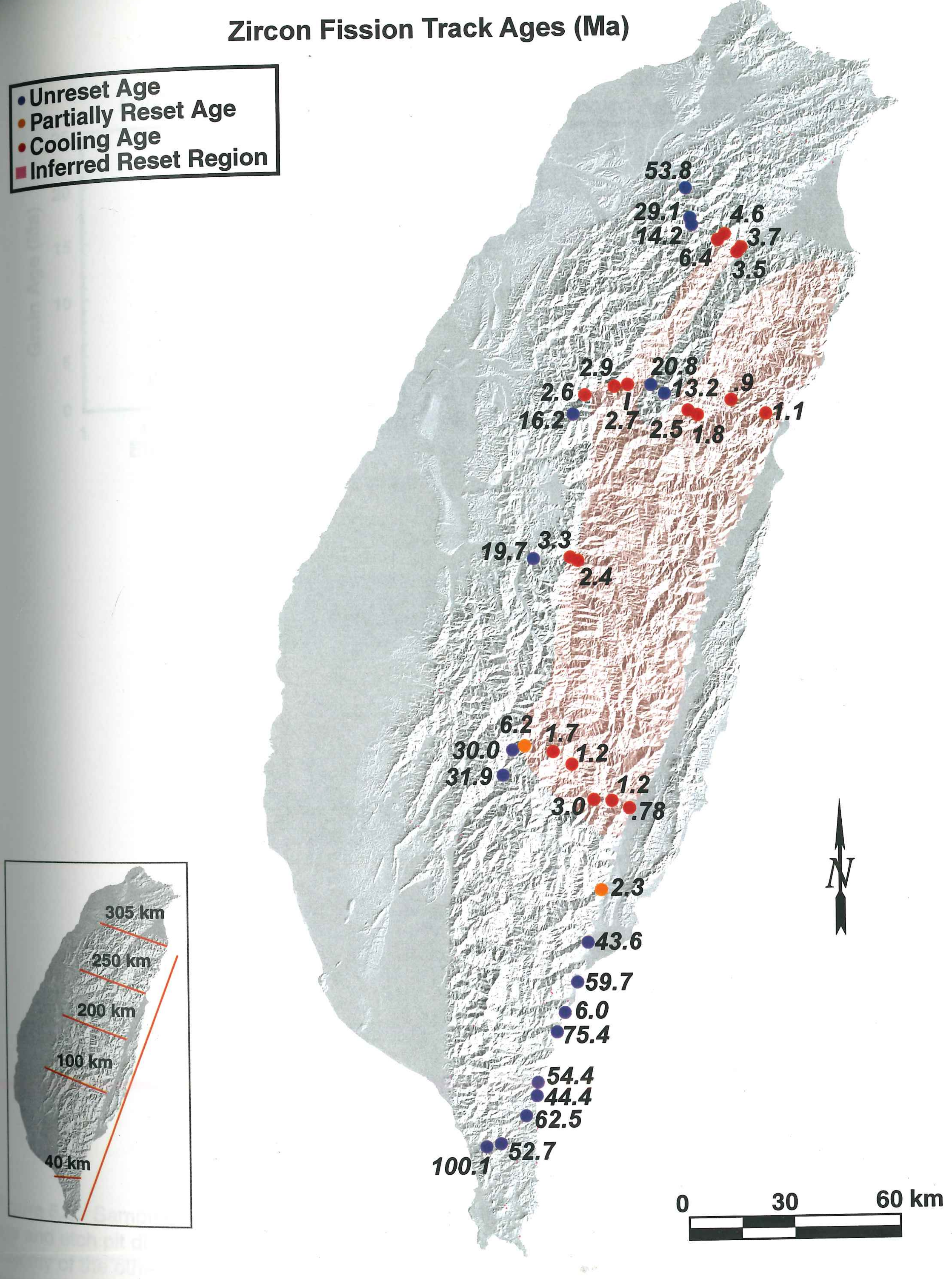

Figure 5.4: Locations and pooled ages or χ^2 ages of ZFT samples used in this study. Inset shows projections used in figures 5.6 and 5.8.

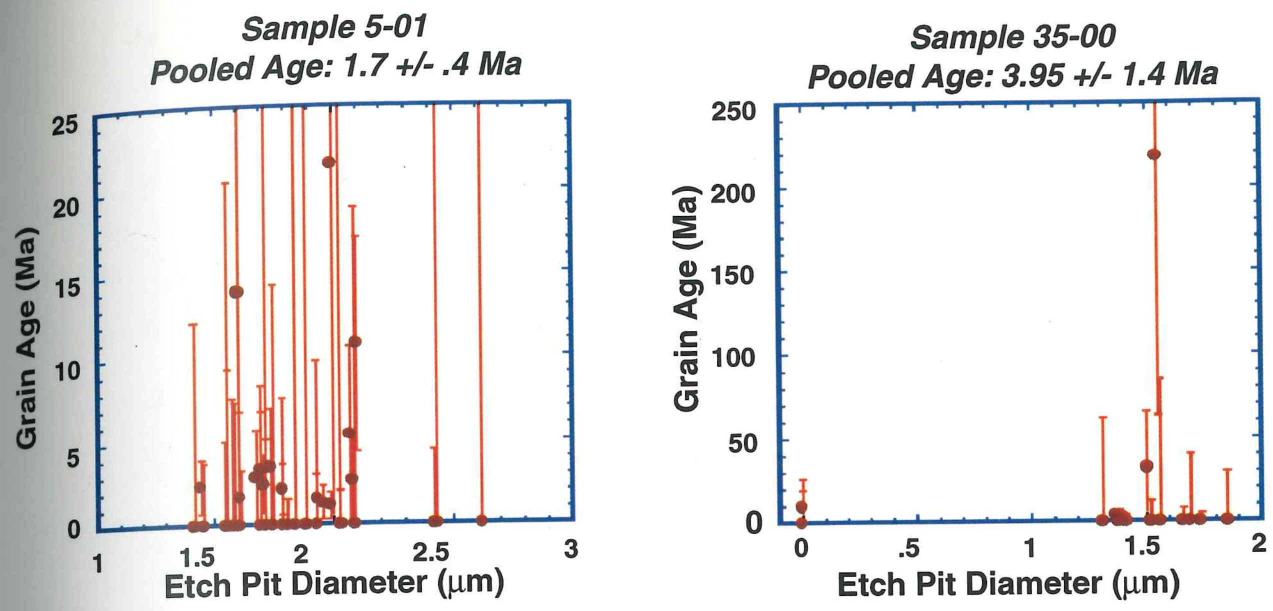
Sample 5-01
Pooled Age: 1.7 +/- .4 Ma

Sample 35-00
Pooled Age: 3.95 +/- 1.4 Ma

Figure 5.5: Samples 5-01 and 35-00 show highly variable grain ages but no distinct correlation between age and etch pit diameter. The lack of correlation suggests that the samples are not partially reset. The majority of the other samples indicated with accretionary ages on figure 5.3 show the same lack of correlation.

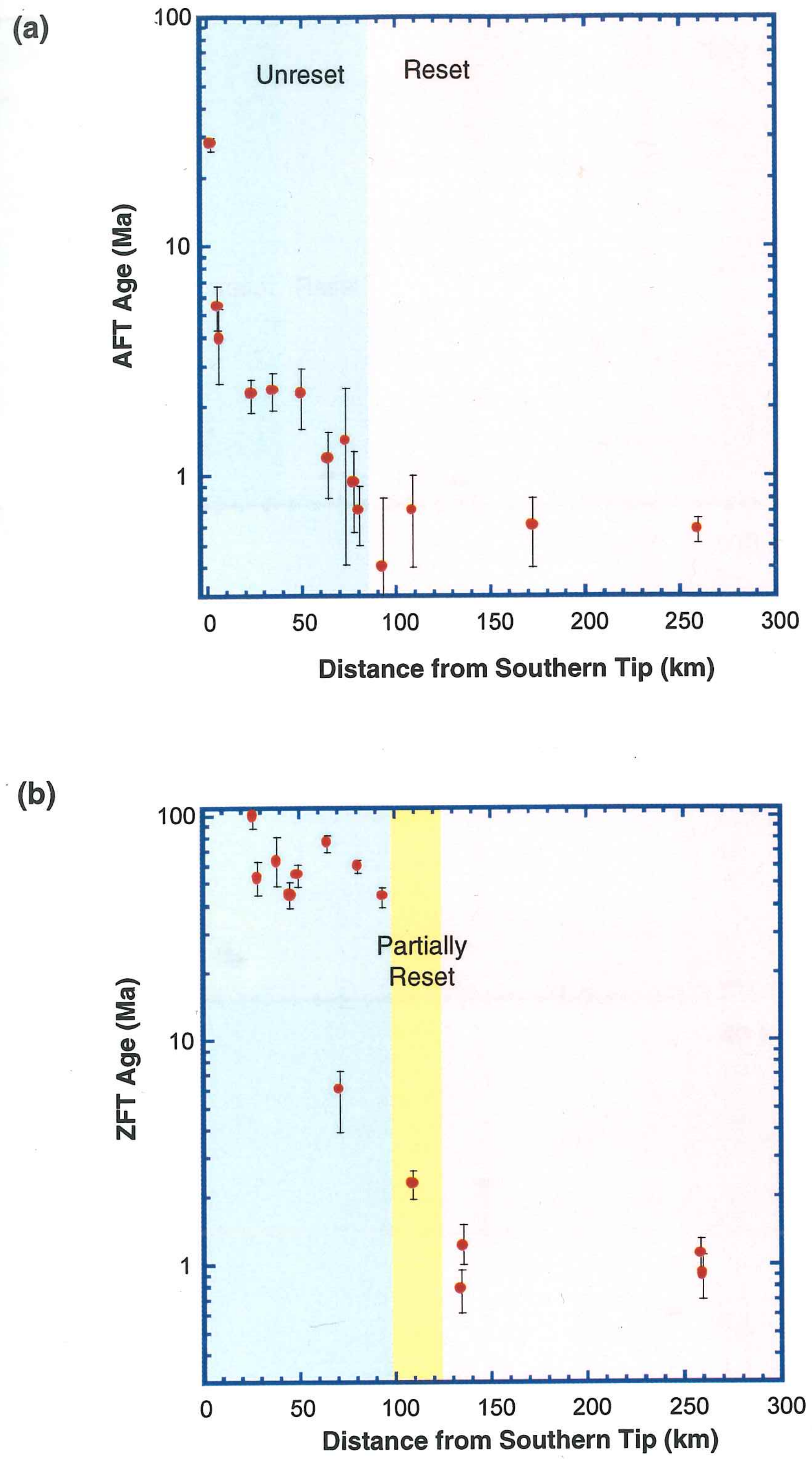

Figure 5.6: (a) AFT and (b) ZFT age trends projected parallel to the strike of the island as indicated in figure 4.3 and 4.4. All data from table 5.1 is plotted with ± 1σ confidence interval while data from table 5.2 is plotted with ± 2σ. Inferred reset, partially reset and unrest zones are indicated where possible.

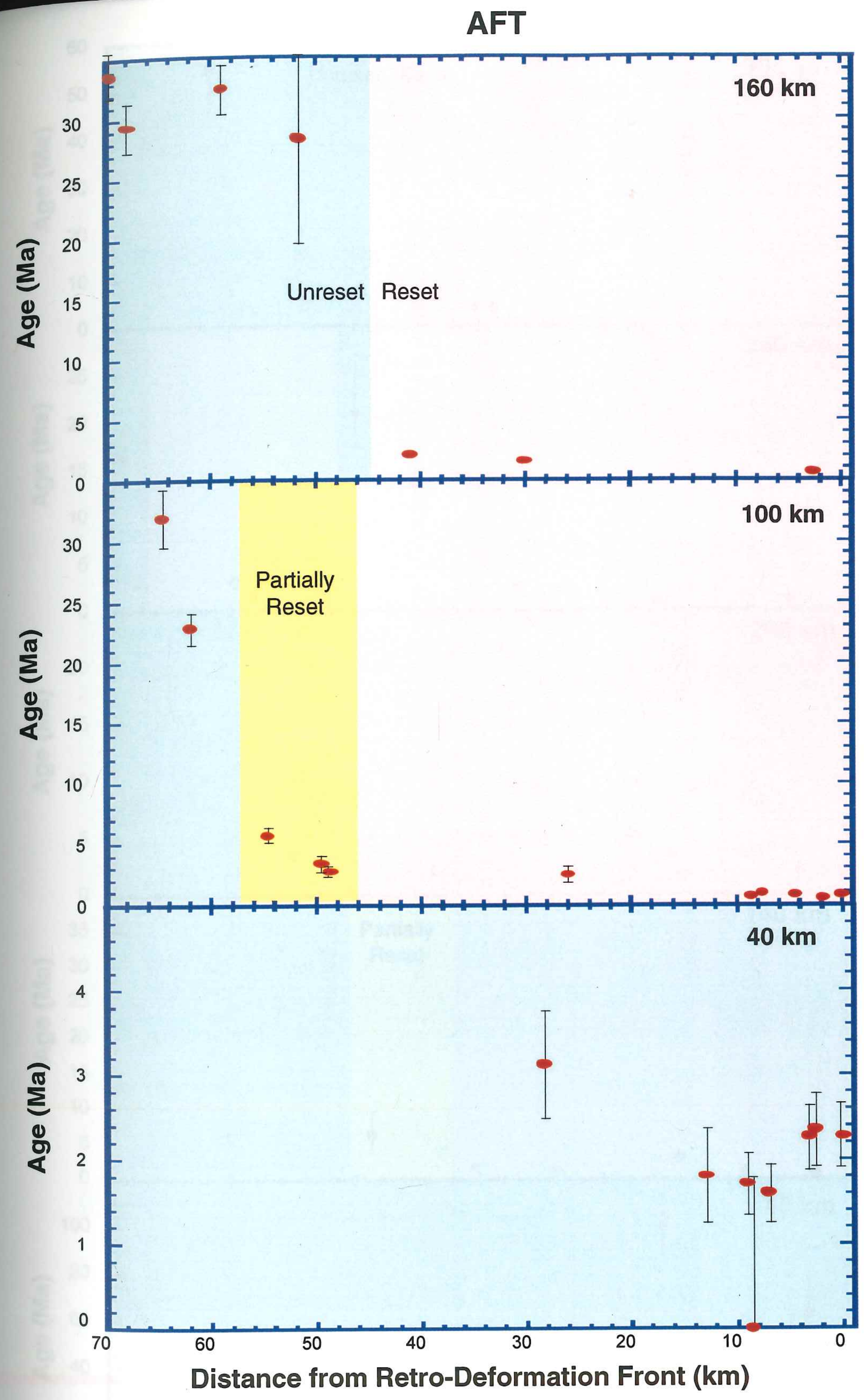

Figure 5.7: AFT ages projected perpendicular to strike at 40, 100 and 160 km from the southern tip of the island as indicated in figure 5.3. See text for discussion.

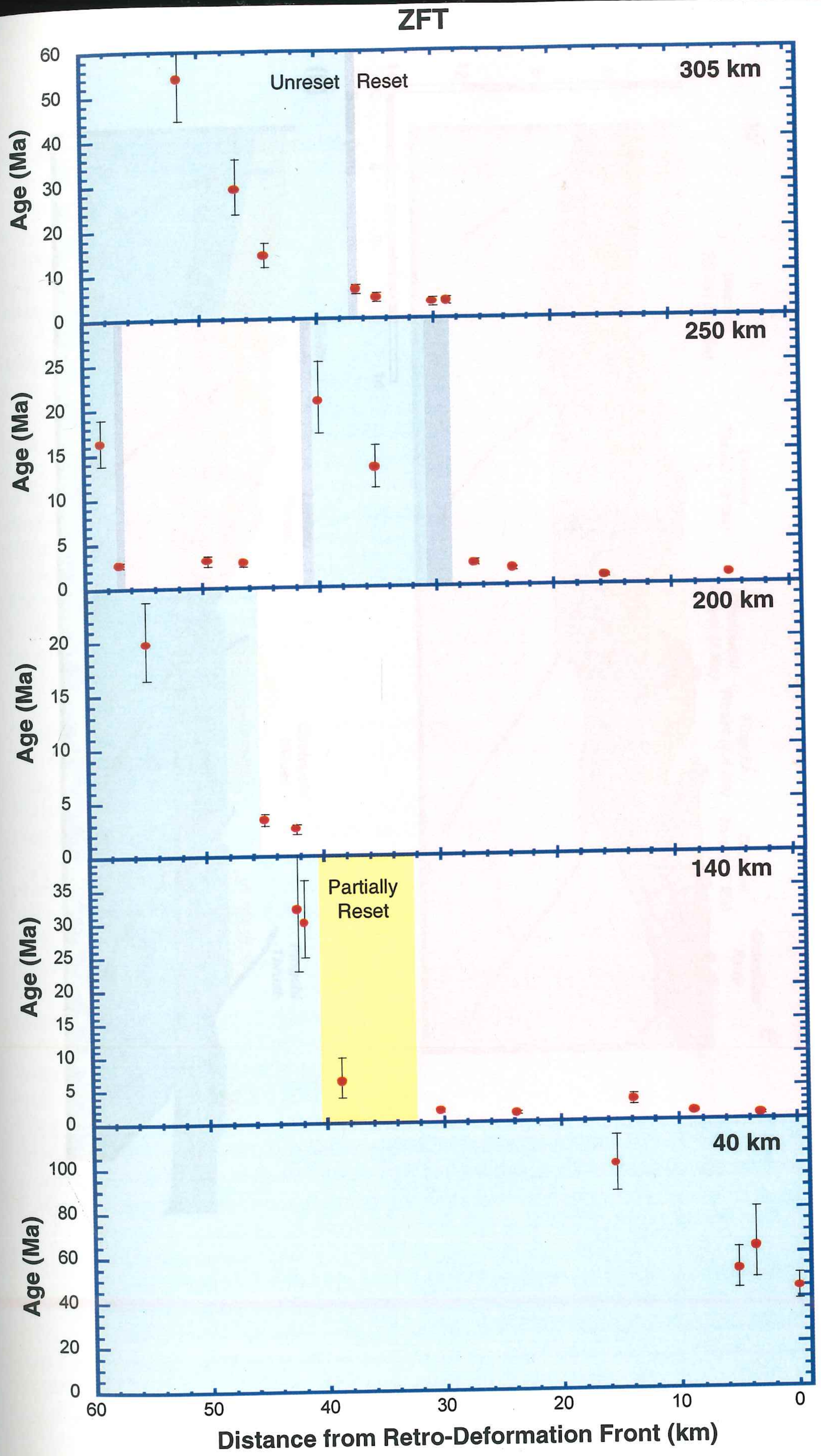

Figure 5.8: ZFT ages projected perpendicular to trend at 40, 140, 200, 250 and 305 km from the southern tip of the island as indicated in figure 5.4. Note that the break in the reset zone at 250 km is due to the Lishan fault. See text for discussion.

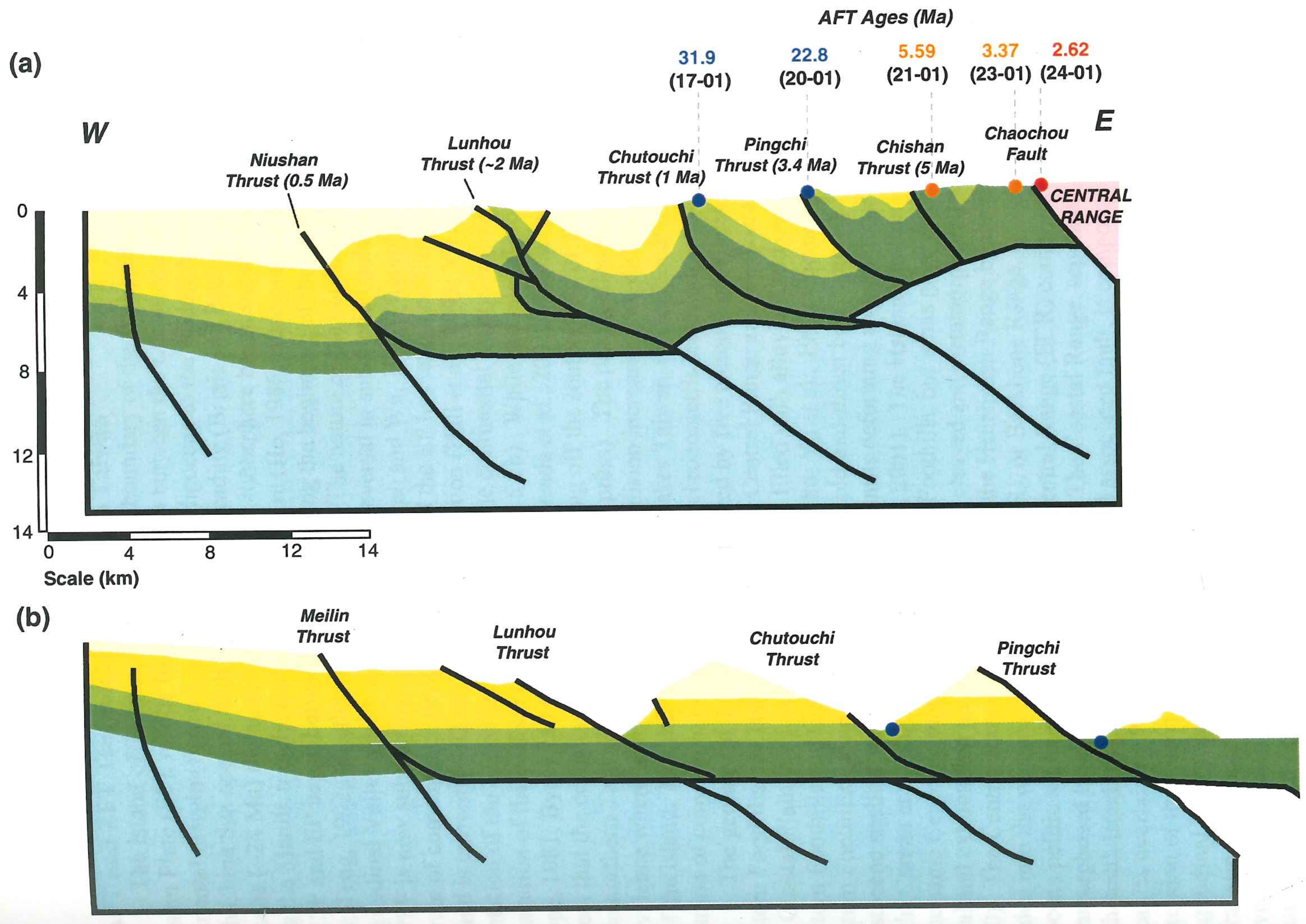

Figure 5.9: Balanced (a) and restored (b) cross section through the Western Foothills as indicated in figure 5.3 with projected AFT ages. labeled with the approximate time of their initiation. *Modified from Mouthereau et al. (2001).*

5.0 AFT and ZFT Thermochronometery in Taiwan

The island of Taiwan, located on the boundary of the Philippine Sea Plate (PSP) and the Eurasian Plate (EP), results from the collision between the Luzon Arc and the Eurasian continental margin (figure 5.1a). From the Oligocene to the Middle Miocene (~32 to 15 Ma) the South China Sea opened with NNW-SSE spreading (Briais and Pautot, 1992). In the Early Miocene (~24 Ma) the newly formed oceanic lithosphere began subducting beneath the PSP along the Manila trench creating the Luzon Arc (Ho, 1986; Huang et al., 2000). The collision of the PSP and EP began between 5-7 Ma marking the beginning of the Penglai Orogeny (Suppe, 1984; Teng, 1992; Mouthereau et al., 2001). The nature of the collision is altered north of the Longitudinal Valley where there has been a reversal in subduction polarity in the past 3-5 Ma and the PSP is now subducting beneath the EP (Rau and Wu, 1995) (figure 5.1a, 5.2). The direction and rate of convergence between the PSP and the EP has remained fairly constant for the past 20 My and is currently ~82 mm/yr in a NE direction (Hall et al., 1995; Yu et al., 1997). The oblique orientation of the Luzon arc with respect to the continental margin results in the southward propagation of the collision with time (figure 5.1b). While the rate of propagation is not clear (Suppe, 1981; Byrne and Crespi, 1997; Chemenda et al., 2001; Mouthereau et al., 2001), it is evident that the collision is presently beginning off the southern tip of Taiwan and began ~ 5-7 Ma in northern Taiwan (Malavieille et al., in press). The propagation results in a space-time equivalence where time since the onset of collision increases with distance north of the southern tip of the island. It is this equivalence that makes Taiwan an ideal location for studying the evolution of convergent orogens with thermochronometric techniques.

The geology of Taiwan is characterized by five tectonic provinces: the Coastal Plain, the Western Foothills, the Hsüehshan Range, the Central Range and the Coastal Range (figure 5.2). The Coastal Plain is a foreland flexural basin filled with alluvium and clastic deposits from the Western Foothills and Central Range (Ho, 1986; Yu et al., 1997; Chemenda et al., 2001). The Western Foothills are an actively deforming fold-and-thrust belt comprised of Upper Oligocene to Pleistocene shallow marine and clastic shelf units deforming along a decollement at ~ 10-12 km depth (Carena et al., 2001; Mouthereau et al., 2001). The Hsüehshan Range is largely composed of the same Cenozoic marine material as the Foothills, but it has gone through more extensive burial and exhumation has therefore exposed cleaved and metamorphosed sediments (Chang et al. 2000). The Central Range is separated from the Hsüehshan Range by the Lishan fault and is divided into the western Central Range (WCR), or Backbone Range, comprised of Eocene to Miocene pelitic sediments, and the eastern Central Range (ECR) comprised of pre-Tertiary metamorphosed basement rocks (Ho, 1986). The Coastal Range, separated from the ECR by the north-south trending Longitudinal Valley and associated fault, is composed of Miocene andesitic volcanics overlain by Plio-Pleistocene flysch-type sediments and is thought to be the on land expression of the Luzon Arc (Ho 1986; Dorsey and Lundberg, 1988; Chang et al. 2000). The Longitudinal Valley fault is a west verging, high angle thrust fault with a component of left lateral slip and is interpreted as the boundary between the EP and PSP. Of the ~82 mm/yr of convergence between the undeforming PSP and the stable continental margin, deformation in the Coastal Range and Longitudinal Valley accounts for ~30 mm/yr (Yu et al., 1997).

5.1 Thermochronometery Data

The AFT and ZFT data used in this study are shown in figures 5.3 and 5.4 and tables 5.1 and 5.2. Table 5.1 is a compilation of ages from recent work by Sean Willett, Don Fisher, En-Chao Yeh and myself. All ages were determined using the external detector method (Ravenhurst and Donelick, 1992). Pooled and mean ages are reported for all samples. The pooled age is determined by combining the track counts of all the grains and determining a single age. The mean age is the mean of the individual grain ages. The pooled age is similar to a weighted mean where grains with higher track counts are preferentially weighted in determining the sample age. This age is preferred when a sample has a single population of grain ages as suggested by passing the χ^2 test. When samples do not pass the χ^2 test the mean age is the preferred representation of the sample age (Galbraith, 1981; Green, 1981). Table 5.2 lists ages determined by Liu (1982) and Liu et al. (2001). The ages reported by Liu (1982) are mean ages while Liu et al. (2001) report χ^2 ages. The χ^2 age, developed by Brandon (1992), is the age of the youngest statistically related group of grains. In this study I use the zircon χ^2 ages, apatite pooled ages and apatite mean ages in the analysis.

The majority of the zircons and apatites in this study are detrital grains from sandstones. There is an expected discordance between grain ages of a single sample due to different cooling or crystallization histories prior to deposition and, for apatite, variations in annealing behavior due to composition (figure 5.5) (Brandon, 1992; Cerveny et al., 1988; Garver et al., 1999). These effects are important to keep in mind when looking at unreset and partially reset samples.

5.2 Thermochronometer Interpretation

I group the AFT and ZFT ages into three groups: reset, unreset and partially reset samples (figure 5.3, 5.4). In general, reset samples have ages much less than the onset of collision (5-7 Ma), and unreset samples have ages greater than the onset of collision. Without track length data to estimate the amount of annealing in a sample, partially reset samples have ages that are younger than the onset of collision but too old to have reached temperatures high enough to be reset. All of the ZFT ages and the majority of the AFT ages are easily classified in this manner. However, the group of AFT samples near the southern quarter of the island indicated with "accretionary ages" do not fit into these classifications. These samples cannot be unreset because their ages are younger than their stratigraphic age. If the samples were partially reset I would expect a trend of increasing grain ages with increasing D_{par} within a sample since higher D_{par} values correlate to higher closure temperatures. Grain ages for individual samples do not show this trend (figure 5.5). Therefore, it appears as is the ages should be classified as reset. If these sample ages reflect cooling due to the current exhumation, it would imply that this portion of the island has been eroding for ~ 2 My. Assuming that submarine erosion is minor when compared to subaerial erosion, the ages also imply that this portion of the island has been above sea level for ~ 2 Ma. This is unlikely since the collision is only began 5-7 Ma ago in the north and has propagated southward (Suppe, 1981; Byrne and Crespi, 997). Therefore, I interpret these ages as having been reset by their accretion at depth into the hot base of the submarine wedge that existed prior to the collision.

5.2.1 Along Strike Trends

The pattern of thermochronometer ages and extent of reset zones observed in Taiwan is very similar to the model predictions when increasing time is thought of as proportional to distance from the southern tip of Taiwan (figure 2.3, 4.7). Projections of AFT and ZFT ages perpendicular to the convergence direction show the expected pattern of ages younging with distance from the south and reaching a fairly constant age (figure 5.6). On along-strike projections, the transition to constant age at ~130 km for ZFT and ~80 km for AFT appears to represent the beginning of exhumational steady state for the two thermochronometers. This interpretation is also supported by looking at the width of the reset zones in the orogen perpendicular trends (see below). There is some variation in these "constant" ages that can be attributed to analytical error, variations due to the projection of samples from out of plane and variations due to the elevation differences between samples.

5.2.2 Orogen Perpendicular Trends

Projections of the AFT and ZFT ages perpendicular to strike also show patterns consistent with model predictions (figure 5.7, 5.8). The projections are characterized by unreset ages far from the retro-deformation front, a rapid decrease in age into the reset zone and then constant or slowly decreasing age as the retro-deformation front is approached. The southern most projection of AFT ages (figure 5.7 at 40 km) contains samples that all have ages classified as accretionary ages, and there is no distinct pattern to the ages. Somewhere between the projection at 40 km and the projection at 100 km reset ages first appear. Further north the reset zone reaches a constant width of ~40-45 km marking the beginning of exhumational steady state for the AFT thermochronometer. The location of this zone, <100 km north of the southern tip, is in agreement with the location determined from the along strike trends shown above (figure 5.6).

The reset zone for the ZFT data is more complicated since it extends farther to the north than the AFT data. Looking first at the the projection at 40 km and moving north to the 140 and 200 km projections, the reset zone increases in width from 0 to ~30 km and then to ~45 km (figure 4.8). However, at the 250 km projection the reset zone is interrupted by a band of unreset samples, also shown in figure 5.4. This break in the reset zone is due to movement on the west dipping Lishan thrust that allows the exhumation of the Hsüehshan Range from greater depths than the Backbone Range (Clark et al., 1993). This discontinuity in thermal histories is also apparent in the metamorphic grade (figure 5.2). The same pattern is expected in the 305 km projection, but the ZFT data are not extensive enough to resolve it. The projections at 250 and 305 km are also in the portion of the island where the polarity of subduction has been reversed (figure 5.1) and the kinematics of the region are poorly understood. It is likely that the distinctively older reset ages in the 305 km section are related to the changing tectonic setting. Finally, it is difficult to estimate a steady-state width of the ZFT reset zone because of the effects of the Lishan fault and the polarity reversal. From the onset of exhumational steady state suggested by the along-strike projections and the similar widths of the reset zone in the projections at 140 and 250 km when ignoring the reset zone due to the Lishan fault, I interpret the steady-state width of the ZFT reset zone to be ~30 km wide and to begin near 130 km north of the southern tip of the island.

5.2.3 AFT Thermochronometry in the Western Foothills

The presence of the Western Foothills fold-and-thrust belt provides an opportunity to examine the relationships between stratigraphic position and thermochronometer ages. Figure 5.9 is a balanced and restored cross section from the Western Foothills adapted from Mouthereau et al. (2001). AFT ages near the transect (samples 17-01, 20-01, 21-01, 23-01 and 24-01, all less than 4 km away) are also included and indicated as reset, partially reset or unreset as in figure 5.3. From east to west the samples are located in (24-01) Pre-Miocene basement rocks of the Central Range, (23-01) the Early to Middle Miocene Nankang formation, (21-01, 20-01) the Late Miocene Chanhchihkeng formation and (17-01) the stratigraphically highest Late Miocene Tangenshan Sandstone. Of interest are the four samples from Miocene units. While none of the samples are reset, they do show different degrees of annealing which generally correspond to their stratigraphic position. For example, the stratigraphically highest and lowest samples, 17-01 and 23-01, show the oldest and youngest ages. However, sample 20-01, unreset with a 22.8 Ma age, and sample 21-01 and 23-01, partially reset with 5.59 and 3.37 Ma ages respectively, are from very similar stratigraphic positions but have undergone different amounts of annealing. Without additional constraints it is difficult to determine how much additional heating the partially reset samples have experienced over the unreset sample. However, based solely on the annealing properties of apatite (Donelick et al., 1990), the partially reset samples would have had to reach temperatures on the order or 90-100° C while the unreset sample had to stay below temperatures of ~60-80° C. Possible explanations for the increased heating experienced by the partially reset samples beneath are deeper burial beneath syn-tectonic Pliocene sediments and initial stratigraphic depths greater than those predicted by the restored cross section. Further stratigraphic analysis is needed to be able to differentiate between these two possibilities.

					Apatite				
Sample	Location		Grains	N_s	N_i	D_{par} (μm)	Pooled Age (Ma)	Mean Age (Ma)	Pass χ^2
	Lon °	Lat °							
48-97	121.017	22.650	22	8	2062	NA	0.7 ± 0.3	0.4 ± 0.2	Yes
52-97	121.042	22.767	31	10	4745	NA	0.4 ± 0.1	0.3 ± 0.1	Yes
65-97	121.067	22.900	25	7	1974	NA	0.7 ± 0.2	0.6 ± 0.3	Yes
67-97	121.300	23.432	25	6	1950	NA	0.6 ± 0.2	0.3 ± 0.2	Yes
1-00	121.010	22.648	40	7	1703	1.65	0.918 ± 0.35	0.957 ± 0.45	Yes
2-00	120.980	22.592	18	2	317	1.52	1.41 ± 1.0	2.17 ± 1.84	Yes
6-00	120.952	22.511	39	10	1912	1.53	1.17 ± 0.37	1.26 ± 0.64	No
9-00	120.891	22.377	26	12	1183	1.6	2.26 ± 0.66	3.69 ± 1.82	Yes
13-00	120.886	22.249	39	31	2929	1.64	2.35 ± 0.43	3.93 ± 1.46	Yes
17-00	120.908	22.589	38	5	2864	1.52	0.388 ± 0.17	0.444 ± 0.27	Yes
19-00	120.932	22.623	36	9	2651	1.59	0.754 ± 0.25	1.08 ± 0.7	Yes
21-00	120.934	22.613	37	4	1519	1.56	0.584 ± 0.293	2.03 ± 1.58	No
27-00	120.831	22.250	3	0	126	1.77	0 ± 1.767	---------------	------
30-00	120.831	21.957	40	263	2081	1.91	27.9 ± 2.0	44.6 ± 12.5	No
32-00	120.883	22.155	35	36	3524	1.68	2.26 ± 0.38	1.3 ± 0.38	Yes
35-00	120.787	22.041	15	8	447	1.53	3.95 ± 1.42	17.8 ± 15.2	No
26-00	120.841	22.269	38	23	3175	1.72	1.6 ± 0.34	1.21 ± 0.33	Yes
29-00	120.762	22.216	20	11	1324	1.79	1.83 ± 0.56	2.65 ± 1.45	Yes
36-00	120.792	22.034	20	22	882	1.94	5.49 ± 1.2	5.42 ± 1.88	Yes
20-00	120.931	22.616	37	7	2584	1.49	0.558 ± 0.21	0.191 ± 0.097	Yes
23-00	120.943	22.620	40	8	2695	1.51	0.608 ± 0.22	2.04 ± 1.35	No
5-01	120.824	22.161	39	22	3087	1.83	1.69 ± 0.36	1.95 ± 0.7	Yes
10-01	120.632	22.389	38	24	1824	1.75	3.11 ± 0.64	7.55 ± 2.92	No
13-01	120.700	22.529	38	14	1389	1.76	2.37 ± 0.64	3.98 ± 2.41	No
15-01	120.648	22.713	36	31	2034	1.73	3.58 ± 0.66	3.68 ± 1.25	Yes
17-01	120.520	23.082	40	237	1739	2.01	31.9 ± 2.4	61.7 ± 10.4	No
20-01	120.544	23.071	39	471	4825	1.95	22.8 ± 1.3	39.6 ± 7.1	No
21-01	120.621	23.073	37	93	3885	1.96	5.59 ± 0.61	30.1 ± 13.7	No
23-01	120.659	23.031	37	29	2005	1.79	3.37 ± 0.64	4.5 ± 1.45	Yes
24-01	120.670	23.046	28	6	532	1.65	2.62 ± 1.08	2.81 ± 2.13	No
25-01	120.610	23.438	38	294	2022	1.9	33.6 ± 2.3	43.4 ± 7.1	No
28-01	120.617	23.432	37	317	2498	1.98	29.3 ± 2.0	47.1 ± 10.5	No
30-01	120.728	23.465	39	392	2864	1.96	32.4 ± 2.0	35.4 ± 6.0	No
31-01	120.821	23.512	3	12	101	1.75	28.2 ± 8.6	26.2 ± 17.1	Yes
34-01	120.841	23.284	34	10	1185	1.77	2.01 ± 0.64	1.84 ± 1.25	No
37-01	120.942	23.263	37	2	319	1.8	1.5 ± 1.06	2.58 ± 1.83	No
					Zircon				
1-00	121.0101	22.648	20	721	606	NA	59.7 ± 3.9	73.4 ± 8.6	No
6-00	120.9518	22.511	14	411	273	NA	75.4 ± 6.4	76.4 ± 13.6	No
9-00	120.8909	22.377	9	179	165	NA	54.4 ± 6.1	74.1 ± 17	No
48-01	121.1755	23.116	19	21	1067	NA	0.78 ± .17	0.862 ± 0.268	
50-01	121.0845	22.898	16	49	850	NA	2.26 ± .34	3.29 ± 0.81	
52-01	121.0494	22.760	20	416	372	NA	43.6 ± 4.4	60.9 ± 12.8	

Table 5.1: New AFT and ZFT ages reported in this study. See figure 5.3 and 5.4 for sample locations. Columns are (1) sample number, (2,3) sample location, (4) number of grains used in analysis, (5) number of spontaneous tracks, (6) number of induced tracks, (7) etch pit diameter, (8) pooled age ± 1σ, (9) mean age ± 1σ, (10) whether or not passed χ^2 test. All –97 samples were dated at Dalhousie University, and all –00 and –01 were dated by Donelick Analytical.

Zircon			
Sample	Location		χ^2 Age (Ma)
	Lon °	Lat °	
MT-403	120.895	23.789	19.7 ± 4, 3.3
MT-402	120.995	23.792	3.3 ± 0.6, 0.5
MT-401	121.025	23.782	2.4 ± 0.5, 0.4
NH-207	121.355	24.782	53.8 ± 11.3, 9.2
NH-206	121.367	24.699	29.1 ± 6.8, 5.5
NH-205	121.372	24.685	14.2 ± 2.9, 2.5
NH-204	121.448	24.641	6.4 ± 1.1, 1
NH-203	121.464	24.654	4.6 ± 1.1, 0.9
NH-202	121.514	24.61	3.5 ± 1.0, 0.8
NH-201	121.523	24.619	3.7 ± 0.9, 0.7
CH-301	121.581	24.173	1.1 ± 0.2, 0.2
CH-302	121.480	24.212	0.9 ± 0.2, 0.2
CH-303	121.38	24.174	1.8 ± 0.2, 0.2
CH-304	121.355	24.182	2.5 ± 0.4, 0.3
CH-305	121.285	24.228	13.2 ± 2.6, 2.2
CH-306	121.248	24.256	20.8 ± 4.4, 3.6
CH-307	121.18	24.257	2.7 ± 0.4, 0.4
CH-308	121.142	24.251	2.9 ± 0.6, 0.5
CH-309	121.056	24.232	2.6 ± 0.4, 0.3
CH-310	121.017	24.175	16.2 ± 2.8, 2.4
SH-507	120.798	23.210	31.9 ± 13.5, 9.2
SH-506	120.833	23.279	30 ± 6.3, 5.2
SH-505	120.853	23.285	6.2 ± 3.6, 2.4
SH-504	120.948	23.268	1.7 ± 0.3, 0.3
SH-503	121.0	23.233	1.2 ± 0.3, 0.2
SH-502	121.067	23.143	3 ±0.9, 0.7
SH-501	121.118	23.135	1.2 ± 0.3, 0.3
SR-601	120.971	22.562	6 ± 1.3, 2.1
SR-602	120.887	22.344	44.4 ± 6.1, 5.4
SR-603	120.859	22.287	62.5 ± 18 13.6
SR-604	120.781	22.215	52.7 ± 9.9, 8.3
SR-605	120.737	22.206	100.1 ± 13.2, 11.8

Apatite	
Sample	Mean Age (Ma)
CL-75-78	0.58 ± 0.07
CL-80-10	0.4 ± 0.03

Table 5.2: ZFT ages reported by Liu et al. (2001) and AFT ages reported by Liu (1982) used in this study. See figure 5.4 and 5.3 for sample locations. For the zircons, columns are (1) sample number, (2,3) sample location, (4) χ^2 age ± 2σ. The apatite samples are the northern most samples in figure 5.3.

6.0 Thermomechanical Model Applied to Taiwan

A qualitative overview of the thermochronometry data for Taiwan shows that it displays the reset age patterns expected in a convergent orogen. However, the data by itself is unable to provide detailed insight into the orogen kinematics. In this section I use the model described above (section 4) primarily constrained by the thermochronometry data to produce a model of the Taiwan orogen. With the model I investigate the importance of underplating as a mode of accretion and estimate the southward propagation rate for the collision between the Luzon Arc and the Eurasian continental margin.

6.1 Model Setup

When applied to the Taiwan orogen, I interpret the model domain shown in figure 4.1a as representing the upper crust of the Eurasian and Philippine Sea plates. The deforming region represents the island of Taiwan from the west coast to the western edge of the Longitudinal Valley. This representation corresponds to modeling the Taiwan orogen only above the observed mid-crustal detachment at 10-12 km. The model does not address deformation in the Longitudinal Valley and the Coastal Range.

I look at the effects of varying the following parameters for the Taiwan orogen: the amount and extent of underplating (v_{up}, u_{beg}), the internal angle of friction (φ), the fluvial erosion factor (k_v), sea level constraints on erosion (d_w), the initial model thickness (h_o), the asthenosphere temperature (T_a), the crustal heat production (A) and the kinetic parameter (D_{par}). Of these parameters there are specific constraints on the water depth and D_{par}. The imposed sea level needs to be within the range of water depths observed in the Taiwan Strait above the continental margin (< 1000m), and D_{par} should be within the range of the sample averages presented here, 1.5-2.0 μm (table 5.1).

All other model parameters are fixed as described above (section 4). However, the convergence velocity, thermal model run-up time and subduction angle have values specific to the Taiwan orogen. I use a convergence velocity of 50 mm/yr that does not include the deformation observed in the Longitudinal Valley and Coastal Range. I determine an average subduction angle of 35° for the Taiwan orogen from the location of the Wadati-Benioff zone (Lin, 1998; Tang and Chemenda, 2000) and seismic tomography (Rau and Wu, 1995; Ma and Liu, 1997). Also, the thermal model run-up time is set at 20 My to simulate the evolution of the PSP-EP subduction zone prior to collision (Hall et al., 1995).

6.2 Model Constraints

I constrain the model by its ability to reproduce orogen dimensions, erosion rates and patterns in thermochronometer ages consistent with those observed for Taiwan. I compare these constraints to the model at output times between 5-7 My. This time frame corresponds to the estimated beginning of collision for the orogen (Suppe, 1984; Teng, 1992; Mouthereau et al., 2001). For the thermochronometry I compare the extent of the AFT and ZFT reset zones and the reset ages to those predicted by the model. Due to the changing tectonic styles in the northern island from the subduction reversal, I make the comparisons between 150 and 250 km north of the southern tip. In this region the AFT and ZFT reset zones are approximately 40-45 km and 30 km wide respectively (section 5). I also use $^{40}Ar/^{39}Ar$ data from Lo and Onstott (1995) that shows reset microclines and partially reset to unreset biotite, hornblende and muscovite in the region indicated on figure 5.2. Combined with the predicted closure temperatures of these minerals (hornblende ~ 568 °C, muscovite ~ 402 °C, biotite ~ 350 °C and microcline ~ 275 °C), the data shows that during burial and exhumation these rocks did not reach temperatures greater than ~ 350 °C for extended periods of time.

The height and width of the orogen are additional key constraints. Peak elevations in Taiwan are between 3-4 km while the maximum width of the orogen between the west coast and the Longitudinal Valley varies between 100 and 140 km. Finally, erosion rates from the model are compared to those estimated from work with suspended sediment. Li (1976) estimated an average erosion rate of 5 mm/yr for the entire orogen, and Fuller et al. (in press), using longer data sets, estimated erosion rates east of the drainage divide at 3-9 mm/yr.

6.3 Model Results

Due to the number of free parameters in the model (table 4.1), I do not present a detailed overview of the parameter space search used in this study. Instead I present a fairly simple model and show how additional complexities allow for the development of what I have determined to be a preferred model of the Taiwan orogen. The parameters used in each model are listed in table 6.1. Since there have not been any published apatite (U-Th)/He ages, this portion of the predictive model is not shown.

6.3.1 No Underplating

Model Mt44 is the starting model for this set of results. The major features of the model are a weak decollement, an initial thickness of 12 km, no sea level cutoff for erosion and no underplating. The weak decollement is implemented in the same manner as in Mg18 with a reduction in the internal angle of friction at the base of the model extending from the S point to the pro-edge of the model. The following parameters were determined by their ability to match the constraints for the Taiwan orogen listed above in models that are not presented here: the internal angle of friction of (6˚) for the weak layer and (15˚) for the rest of the domain, the initial model thickness (12 km), the valley erosion factor (17), the heat production (1.0 $\mu w/m^3$) and the basal temperature boundary condition (1227 ˚C). The effects of changes in most of these parameters are presented above (section 4). Finally, a D_{par} value of 1.8 μm is used for the AFT model.

Figure 6.1 shows the results of model Mt44 with the constraints provided by the Taiwan orogen for the steady-state width, maximum elevation and erosion rates as well as the maximum temperature reached by particles and the extent of the reset zones with each plot. In Mt44 the maximum elevation is approximately 500 m too low, the orogen width is approximately 10-30 km too narrow and the erosion rates on the retro side are within the observed values (figure 6.1a). Also, the particle paths and resulting temperature histories from Mt44 all have maximum temperatures below 350 ˚C. Finally the AFT and ZFT reset zones are both approximately 15 km too narrow.

Despite the misfit of Mt44 to the observations of the Taiwan orogen listed above, it is an appropriate starting point in the modeling exercise because by varying only a few parameters this model evolves to the preferred model for Taiwan. Also, model Mt44 has two important features observed in Taiwan that persist through all of the models presented in this section: (1) Mt44 evolves to a steady state where the maximum elevation, orogen width and reset zones are constant and (2) the weak detachment leads to a broad zone of deformation on the pro side of the model that can be interpreted as a representation of the Western Foothills fold-and-thrust belt.

6.3.2 Underplating

As was demonstrated above (section 4), prescribing underplating as a mode of accretion can increase the width of the orogen and reset zones. Model Mt47 is identical to model Mt44 but has 50% of accreted material coming from a zone of underplating extending 37 km to the pro side of the S point (table 6.1) (figure 6.2). The effects of adding underplating to Mt44 is very similar to differences seen between models Mg4 (figure 4.6, 4.7, 4.8) and Mg14 (figure 4.13). The underplating has little effect on the maximum elevation, still ~500 m too low, and orogen width, still ~20-40 km too narrow, (figure 6.2a) when compared to Mt44 (figure 6.1a). The underplating does result in particles reaching peak temperatures ~25 ˚C higher (figure 6.2b) than in Mt44 (figure 6.1b), and they remain below 350 ˚C. The result of the higher peak temperatures is that the ZFT reset zones of Mt47 (figure 6.1c) are wider than in Mt44 (figure 6.1c). However, both

AFT and ZFT reset zones are still too narrow, ~15 and 10-12 km respectively, when compared to the Taiwan orogen. Other combinations of underplating amount and extent were also investigated, but with all other parameters fixed at the current values none were able to produce a better fit to the Taiwan orogen.

6.3.3 Effects of Underplating and Raising the Erosion Base Level

Implementing a sea level constraint on erosion is shown above as an effective means to increase peak elevations, orogen width and reset zone widths (model Mg25). Model Mt48 is identical to model Mt47 but with a water depth of 500 m (figure 6.3). With the raised base level the maximum elevation (~3.5 km), orogen width (~110 km), orogen averaged erosion rates (5 mm/yr), AFT reset zone width (~42 km) and ZFT reset zone width (~25 km) are all within the bounds observed in the Taiwan orogen (figure 6.3). There are, however, two discrepancies between this model and the Taiwan orogen: (1) the tracked particles reach temperatures greater than 350 °C, and (2) the predicted AFT and ZFT reset ages are younger than those observed in Taiwan. These discrepancies will be discussed in further detail below. In spite of the age differences and high temperatures, model Mt48 is the best representation of the Taiwan orogen as defined by the constraints mentioned above from the suite of 200+ models examined.

6.4 Discussion

While model Mt48 is the preferred model for the Taiwan orogen, there are discrepancies in the maximum temperatures reached by some of the material exposed at the surface and the AFT and ZFT reset ages. I do not interpret the fact that material passes the 350 °C isotherm as crucial due to the possible uncertainty in this temperature, the relative small amount of surface material (< 7 km in lateral extent) that passes 350 °C and the relative short period of time the material spends above 350 °C (all < .5 My, most < .25 My) (figure 6.3b). The differences between the predicted and observed fission-track ages are more significant. The minimum AFT ages from Taiwan are 0.4 to 0.6 Ma with 1-σ of approximately ± 0.1 to 0.2 (figure 5.3) (table 5.1), and the minimum ZFT ages are 0.8 to 1.1 Ma with 1-σ of approximately ± 0.2 (figure 5.4) (table 5.2). In contrast, the minimum predicted AFT and ZFT ages of Mt48 are < 0.1. One explanation for the differences in apatite ages could be variability in apatite annealing, but models run with the maximum and minimum observed D_{par} values of 1.5 and 2.0 μm (table 5.1) have little effect on the ages (figure 6.4). Other reasons for the age differences could be inaccuracies due to model resolution, variations in observed ages due to elevation effects, incorrect classification of observed ages that are actually partially reset and the inability of a continuum model to predict the kinematics of an orogen that has significant deformation occurring on discrete structures, i.e. faults. Regardless of the causes of these age differences, they are fairly small when the uncertainty of the fission-track ages are taken into consideration.

The general behavior of model Mt48 is shown with the second invariant of the rate of deformation tensor, the rate of deformation in the x (horizontal) direction and the evolution of the temperature field in figures 6.5, 6.6 and 6.7. The preferred model has three main characteristics that allow for the reproduction of the general thermochronometry trends observed in Taiwan: a sea level constraint on erosion, a weak layer representing a mid-crustal decollement and underplating as a mode of accretion. The sea level constraint on erosion is essential to modeling the orogen because it allows the orogen to grow prior to the onset of subaerial erosion. Model Mg18 (section 4) illustrated that a weak layer at the base of the model extending from the S point to the pro-edge of the model allows for the development of a broad zone of deformation on the pro-side of the model. In models for the Taiwan orogen this layer, representing a mid-crustal detachment, is needed to create a wide zone of deformation analogous to the fold-and-thrust belt of the Western Foothills. The necessity of the detachment in the numerical model is in direct agreement with the work of many others (e.g. Suppe, 1980; Chen, 1999; Carena et al, 2001; Mouthereau et al., 2001).

Model Mt48 also shows that the thermochronometery data is reproduced better with underplating as a mode of accretion. However, it is useful to go beyond this conclusion and estimate the amount and extent of underplating. Model Mt51 illustrates the variation in reset zone widths when the amount of underplating is decreased from 50% to 25% (figure 6.8). While all of the other constraints are still within the limits defined above for Taiwan (figure 6.8a,b), the AFT and ZFT reset zones decrease in width and are both ~5 km too narrow. This observation suggests that underplating plays a very significant role in the Taiwan orogen. In particular, underplating accounting for 50% of the accreted material in the orogen is consistent with the thermochronometry data.

This result conflicts with the study of Barr et al. (1991) where, using the Barr and Dahlen model described above (section 3), they determine from a flux balance of accreted material and from the extent of metamorphic facies that underplating is an insignificant process in the growth of the Taiwan orogen contributing to at most 10-25% of the accreted material (Barr et al., 1991). The discrepancy between the results of Barr et al. (1991) and those presented here are most likely due to the simplifying assumptions used in their kinematic model, especially the assumption of a vertical no-flux boundary at the rear of the orogen (Dahlen and Barr, 1989). The no-flux rear boundary follows from the analog of the Dahlen and Barr (1989) model as a bulldozer pushing a pile of sand. The blade, or no-flux boundary, forces particles into near vertical paths at the rear of the orogen. However, the Taiwan orogen is more accurately represented as a doubly vergent orogen (Willett et al., 1993) and not a pile of sand in front of a bulldozer. As was shown in the models presented here, a doubly vergent orogen does not have vertical particle paths, but these paths can be steepened through the implementation of underplating as a mode of accretion. I suggest that the models of Barr & Dahlen do not need large amounts of underplating because of the unnaturally steep particle paths that follow from the no-flux boundary condition.

The effects of extending the underplating zone another 60 km is shown with model Mt52 (figure 6.9). The orogen dimensions of Mt52 are a reasonable fit to the Taiwan data, and the reset zones are only slightly narrower than those of Mt48. The initial interpretation is that it may be difficult to resolve the appropriate extent of underplating for Taiwan. However, it is important to notice that the particles in Mt52 reach temperatures up to 400 ˚C and are above 350 ˚C for > 1 My. The temperatures and time spent at these temperatures is significantly greater than in model Mt48. I interpret the temperature histories of Mt52 to be in conflict with the maximum temperature constraint of 350 ˚C from the ^{40}Ar/^{39}Ar dating (Lo and Onstott, 1995). To make model Mt52 fit within the maximum temperature while keeping the same kinematics, several parameters would need to be adjusted to reduce the overall temperature field. However, reducing the temperature of the entire model domain will also decrease the width of the reset zones worsening the model fit. Therefore, a narrow zone of underplating is best at reproducing the observed thermochronometry patterns.

The indication of a narrow underplating zone has significant implications with respect to the evolution of the Taiwan orogen. One debate surrounding the Taiwan orogen is whether or not the deformation is limited in extent to the upper crust or if it extends into the lower crust and upper mantle (Suppe, 1981; Davis et al., 1983; Dahlen and Barr, 1989; Rau and Wu, 1995; Ellwood et al, 1996; Wu et al., 1997; Lin, 1998; Chen, 1999; Tang and Chemenda, 2000). Following the idea that deformation in Taiwan is focused in the upper crust, the narrow zone of underplating used here is easily interpreted as a region where subducting lower crustal material is underplated across the detachment. Another interpretation of the narrow underplating zone is that it represents lower crustal to upper mantle material that is being exhumed in the core of the orogen. Lin (1998, 2000) and Chemenda et al. (2001) propose that this material is a section of the Eurasian continental margin that has been subducted and is currently being exhumed due to buoyancy forces. Wu et al. (1997) also include material from greater depths in their model of Taiwan orogenesis by proposing that the collision extends into the upper lithosphere. In this model the narrow zone of underplating would represent the ductile extrusion of thickened crust beneath the Central Range. While the models presented here show that the thermochronometry data is consistent with underplated lower crustal material, they are unable to test the validity of these other hypotheses since they require drastically different particle paths than those shown in figure 6.3b.

Suppe (1981) initially proposed a constant southwards propagation of collision for the Taiwan orogen with a rate of 90 km/my. More recently Byrne and Crespi (1997) have estimated the rate to be at 55 km/my. Using the thermochronometry data presented here and the predicted reset zones of the preferred model, I can estimate the southward propagation rate in three ways. Assuming that submarine erosion is negligible compared to subaerial erosion, I calculate two propagation rates by comparing the distance between the southern tip of the island and the beginning of the ZFT reset zone (~125 km) (figure 5.4) and AFT reset zone (~72 km) (figure 5.3) to the time between the onset of erosion in the model and the beginning of the ZFT (~2.25 My) and AFT (~1.0 My) reset zones (figure 6.3c). Taking into account the time resolution of the model and uncertainties in the location of the reset zones, I determine southward propagation rates of 55 ± 5 km/my from the ZFT data and 70 ± 10 km/my from the AFT data. I calculate the final rate using the correspondence of the southern limit of the AFT and ZFT reset zones (~50 km) (figure 5.3, 5.4) to the time lapse (~1.25 My) between the first exposures of the reset zones as determined from the model (figure 6.3c). Taking into account the model resolution and uncertainties in the locations of the reset zones, I determine a propagation rate of 42 ± 8 mm/yr.

The differences in these propagation rates are significant in that they suggest the propagation rate is not constant through time. Figure 6.10 shows the propagation rates and the regions of the island over which they were determined. The rate from the AFT and ZFT data (42 km/my) is the lowest rate and averages over the indicated region (figure 6.10). The increase in rate to the south with the AFT determined rate (70 km/my) suggests that the propagation rate increased in the southern portion of the island. Finally, the ZFT rate averages over the combined area of the other rates (figure 6.10) and shows the consistency of this argument with a rate between the others (55 km/my). It is important to remember that these rates are highly dependent on the classification of the thermochronometry data as either reset and unreset.

6.5 Conclusions

In this study I have investigated the kinematics of the Taiwan convergent orogen through the use of new thermochronometry data and thermomechanical modeling. This study has built on previous modeling efforts with its use of an advanced thermomechanical model of convergent orogeneses coupled to the latest predictive models of AFT, ZFT and (U-Th)/He ages. The fission track data for the island shows the expected trends of nested reset zones corresponding to closure temperatures of AFT and ZFT, ages changing from unreset to reset as expected from the southward propagation of the collision and a direct correlation between AFT ages and stratigraphic depth for samples from the modern fold-and-thrust belt. The observed thermochronometry patterns were used to constrain the thermomechanical model for the Taiwan orogen. The preferred model was able to reproduce the geometry and patterns of reset ages for the Taiwan orogen but slightly under predicted the ages of reset thermochronometers. Some of the key features of this model are a delayed onset of erosion from an imposed erosion base level, the existence of a mid-crustal detachment, average erosion rates across the orogen of approximately 5 mm/yr and the necessity of underplating as a significant mode of accretion. The preferred model for Taiwan is consistent with 50% of accreted material coming from underplating over a narrow zone (tens of kilometers) under the center of the orogen. Finally, by looking at the new thermochronometry data combined with the results of the thermomechanical model, it appears that the southward propagation of the collision has not been constant in time. My best estimate of the current and long term average propagation rates is 70 ± 10 mm/yr and 55 ± 5 km/my.

Model	Mt44	Mt47	Mt48	Mt49	Mt50	Mt51	Mt52
% Underplating	0	50%	50%	50%	50%	25%	50%
Width of Underplating Zone (km)	NA	37	37	37	37	37	97
v_{up} (m/My)	NA	8200	8200	8200	8200	4100	3200
Initial Crustal Thickness, h_o (km)	12	12	12	12	12	12	12
Scaled Crustal Thickness, h_s (km)	12	5.9	5.9	5.9	5.9	5.9	5.9
k_v	17	17	17	17	17	17	17
φ (°)	15° with basal detachment at 6°	15° with basal detachment at 6°	15° with basal detachment at 6°	15° with basal detachment at 6°	15° with basal detachment at 6°	15° with basal detachment at 6°	15° with basal detachment at 6°
d_w (m)	0	0	500	500	500	500	500
Heat Production (μW/m^3)	1.0	1.0	1.0	1.0	1.0	1.0	1.0
T_a (°C)	1227	1227	1227	1227	1227	1227	1227
D_{par} (μm)	1.8	1.8	1.8	1.5	2.0	1.8	1.8

Table 6.1: Parameters used in models of the Taiwan orogen.

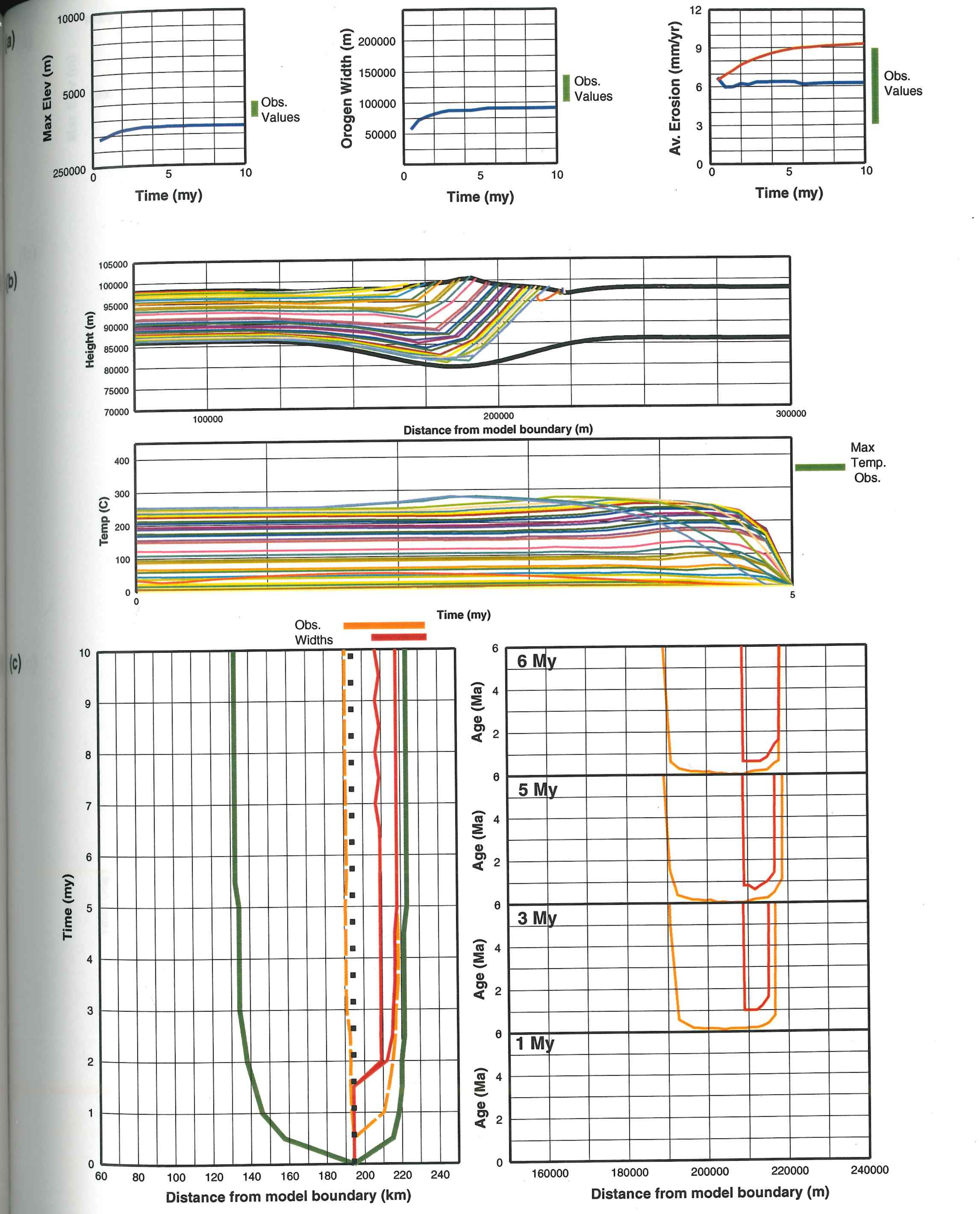

Figure 6.1: Results of model Mt44 shown with the observed constraints on: (a) maximum elevation, orogen width and erosion rates, (b) maximum temperature reached by particles at the surface and (c) width of the reset zones. For plot legends see figures 4.7 and 4.8. Tracked particles for this and all following plots are taken from model output at 5 My.

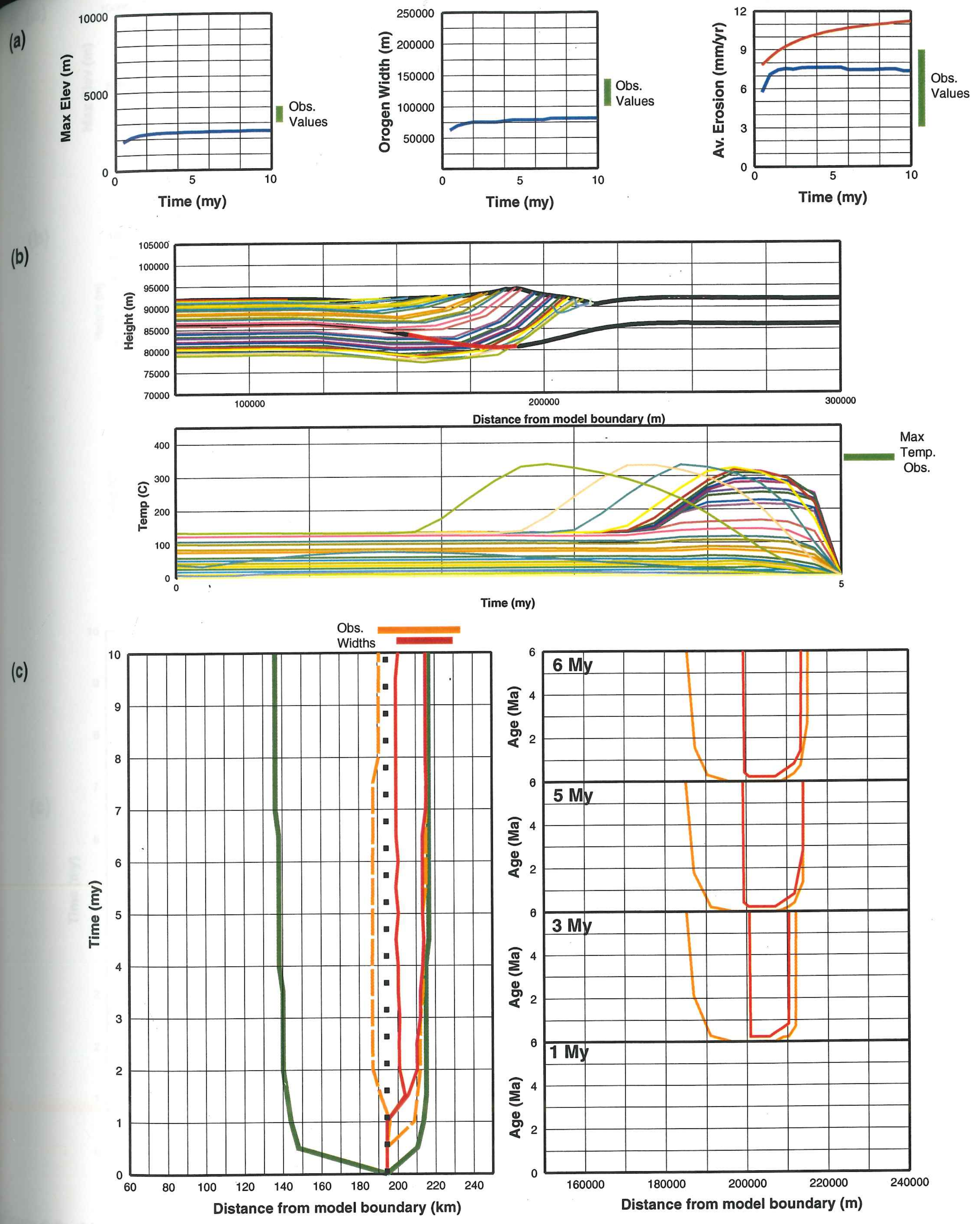

Figure 6.2: Model Mt47 (shown here) is identical to model Mt44 but has 50% underplating occuring over the region indicated in red (b). The underplating has little effect on the orogen dimensions (a). The underplating increases the maximum temperature reached by particles exposed on the surface (a) and increases the width of the ZFT reset zone (c) when compared to model Mt44 (figure 6.1).

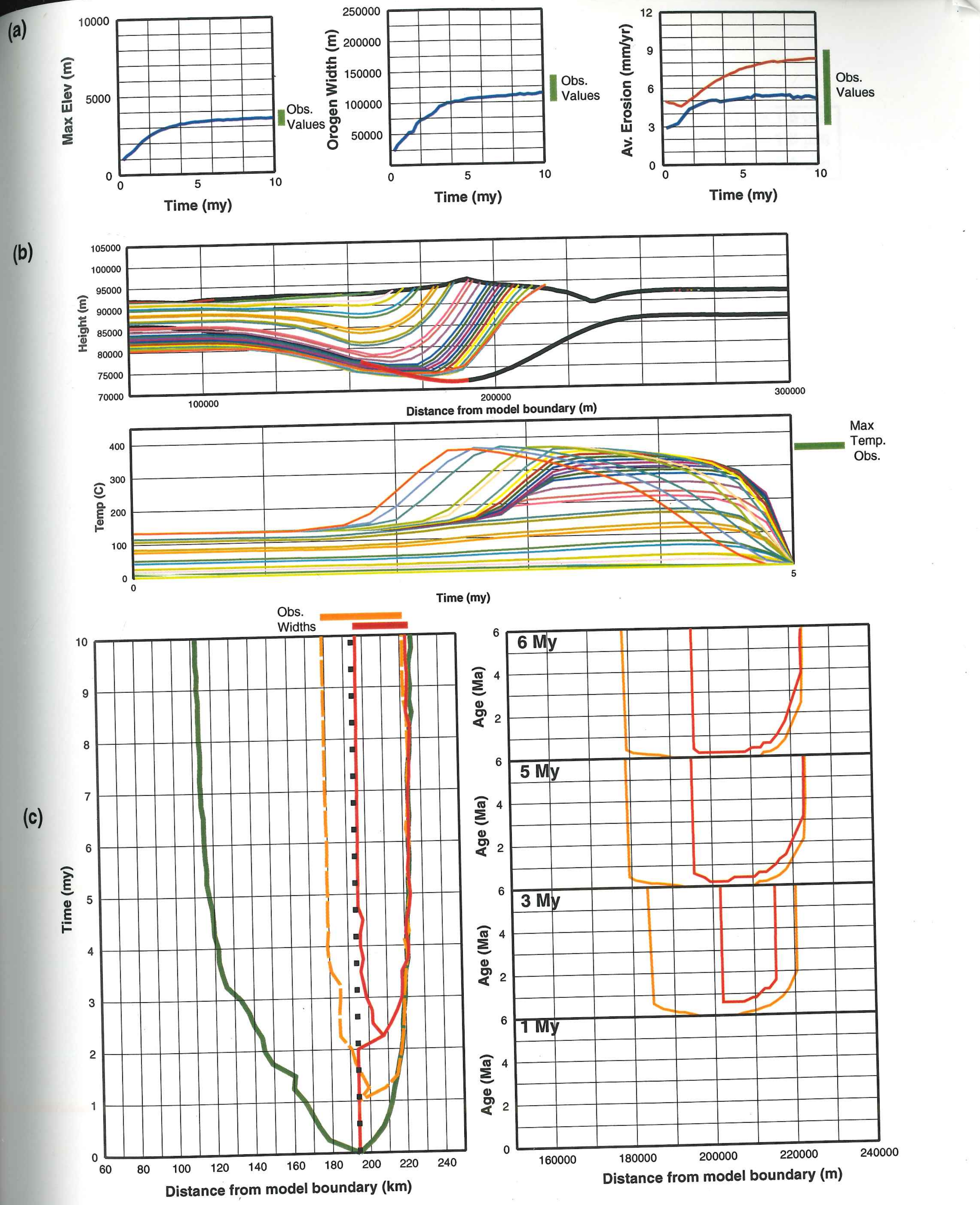

Figure 6.3: Model Mt48 (shown here) is identical to model Mt47 but has an elevated erosion base level from a 500 m sea level (table 6.1). Raising the base level results in orogen elevations, widths, erosion rates and reset zones that are in agreement with the Taiwan orogen (a,c). However, some of the particles exposed at the surface reach temperatures in excess of 350 C (b), and the reset thermochronometer ages are younger than those observed in Taiwan (c). Regardless of these discrepancies, model Mt48 is the preferred model for Taiwan.

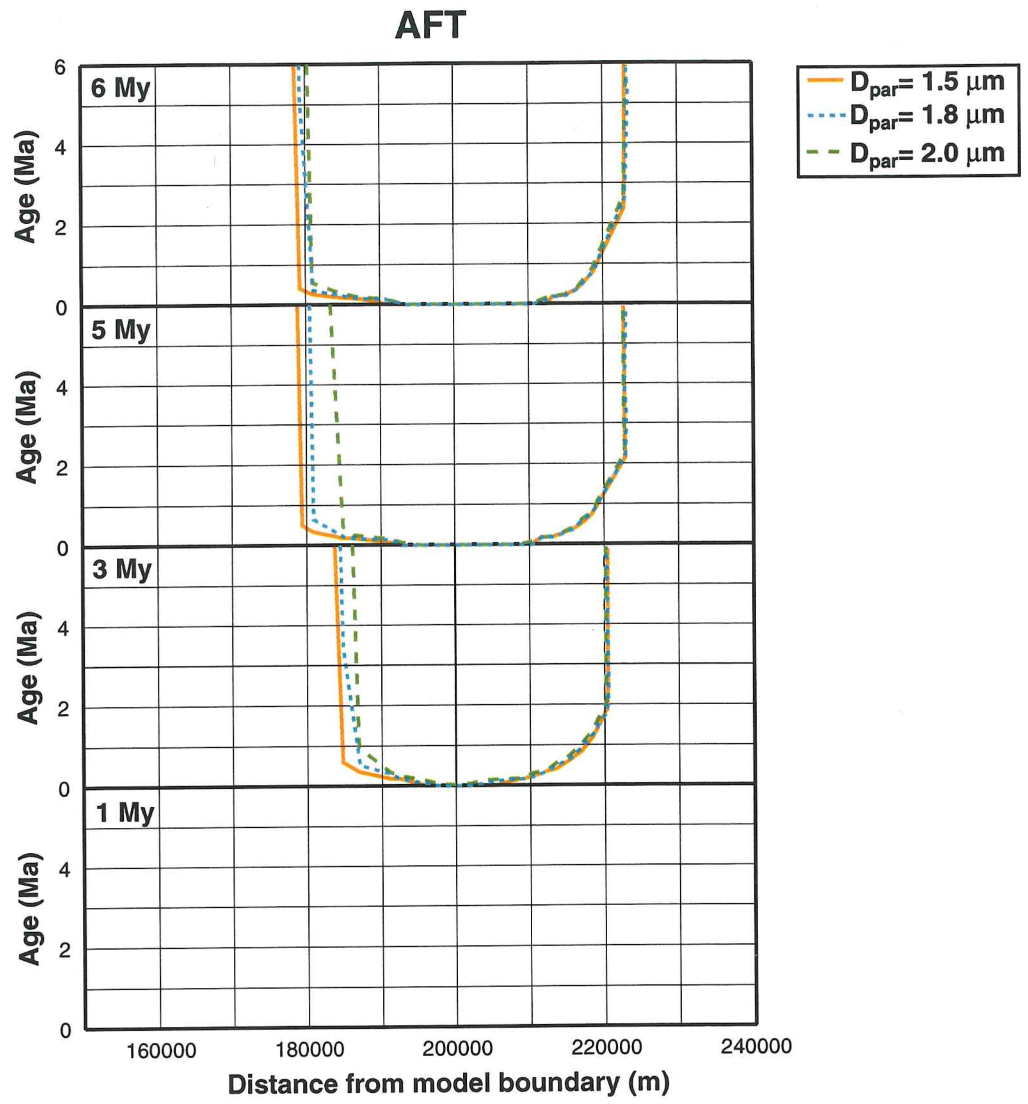

Figure 6.4: Differences in AFT reset ages with varying Dpar for model Mt48, Mt49 and Mt50. While the width of the reset zones vary, the minimum ages show little change.

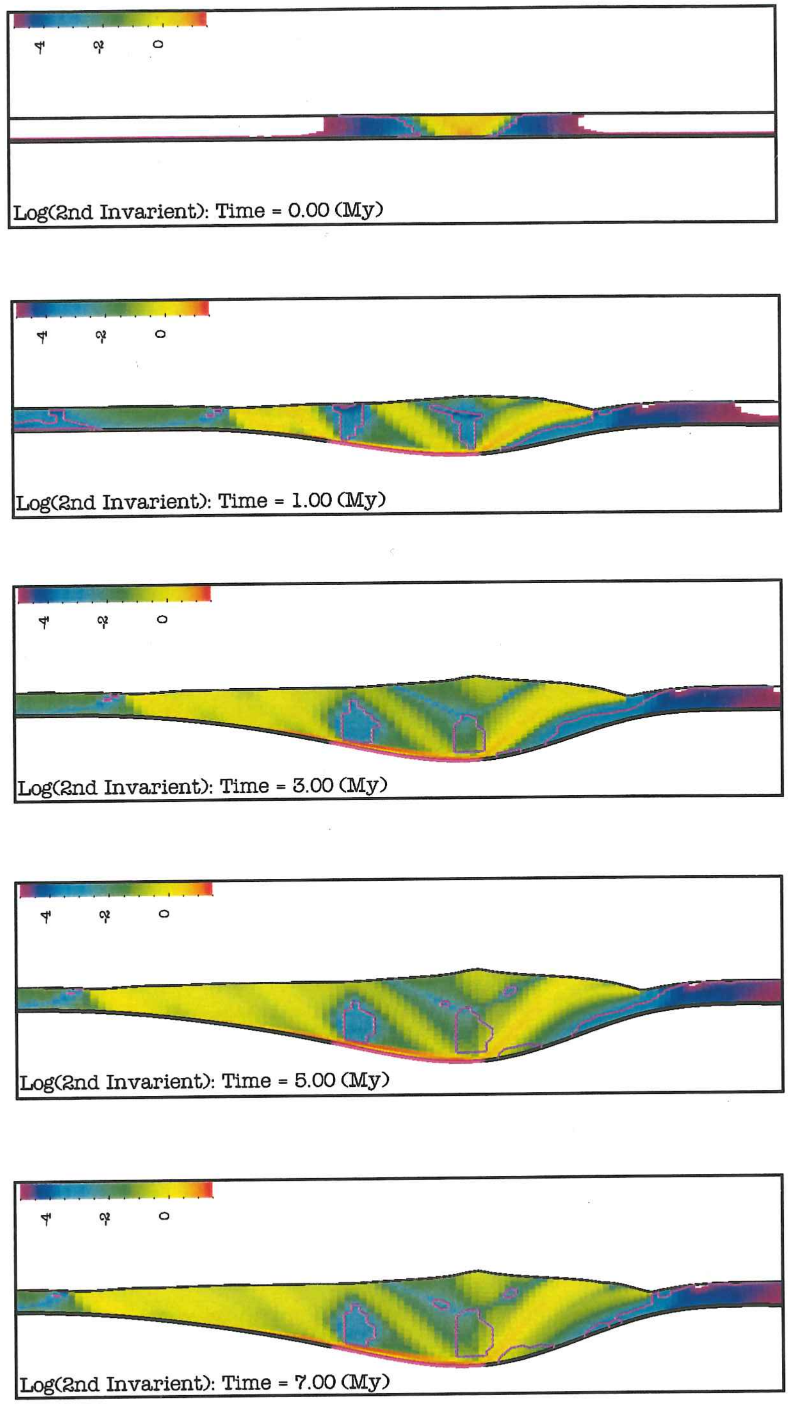

Figure 6.5: The second invariant of the rate of deformation for model Mt48. White regions are values < -5.0. he highlighted area on the model base indicates the region of underplating.

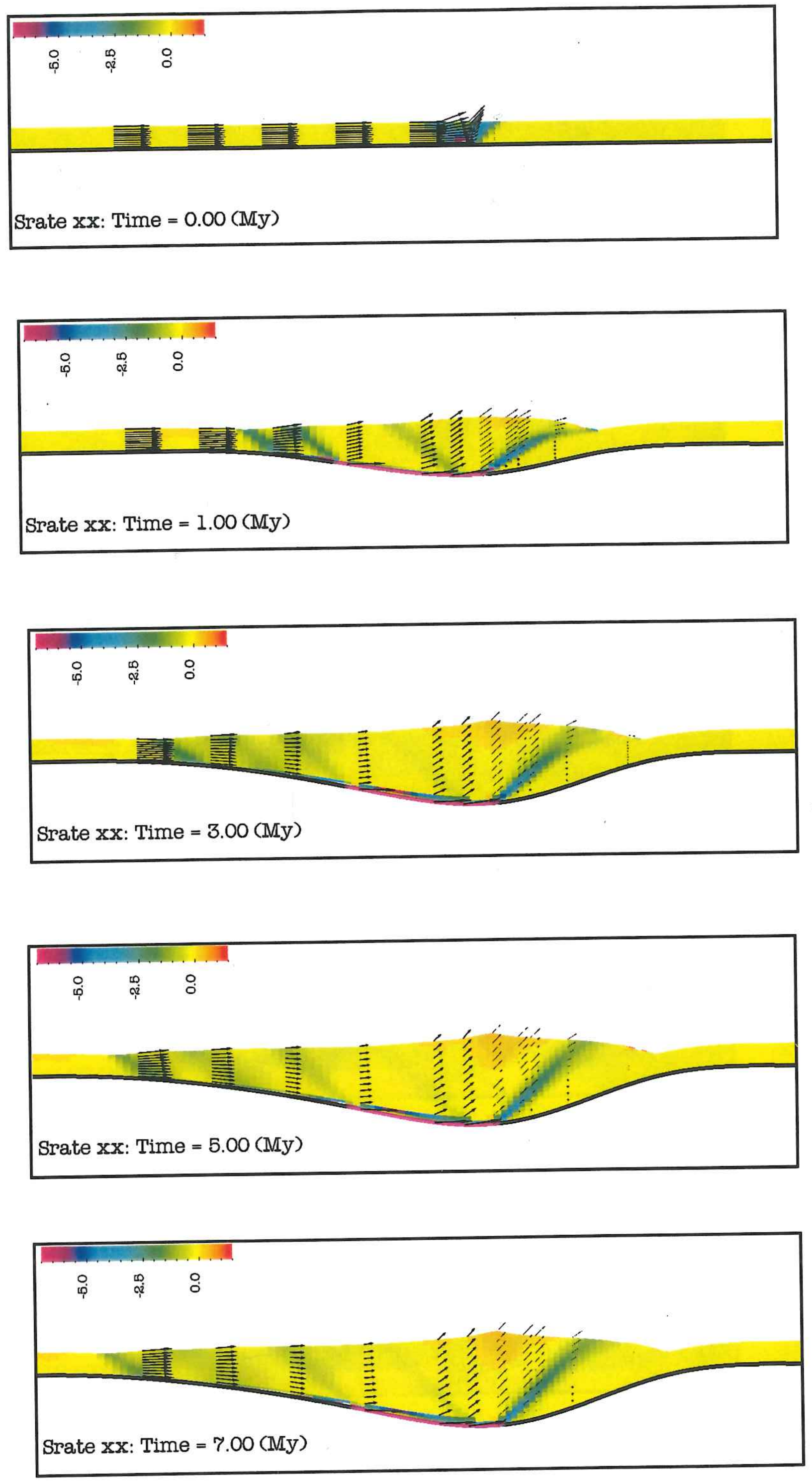

Figure 6.6: Strain rate in the x (horizontal) direction for model Mt48. Arrows show direction and relative magnitude of velocity. The highlighted area on the model base indicates the region of underplating. Note the partial decoupling of the orogen from the subducting material evident in the contrast in size between the velocity vectors in the orogen and along the base.

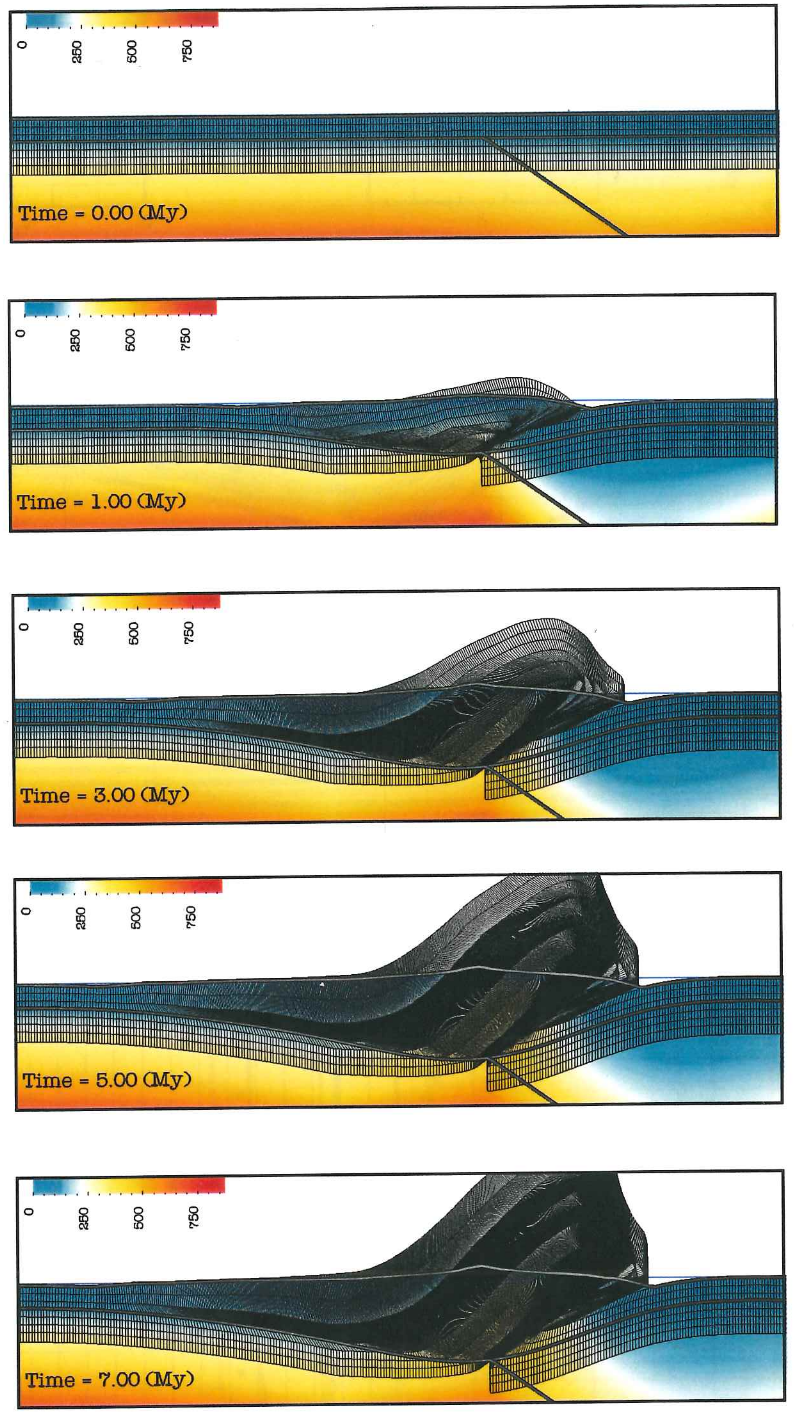

Figure 6.7: Temperature field and Lagrangian mesh for model Mt48. The blue line indicates the model sea level below which no erosion occurs.

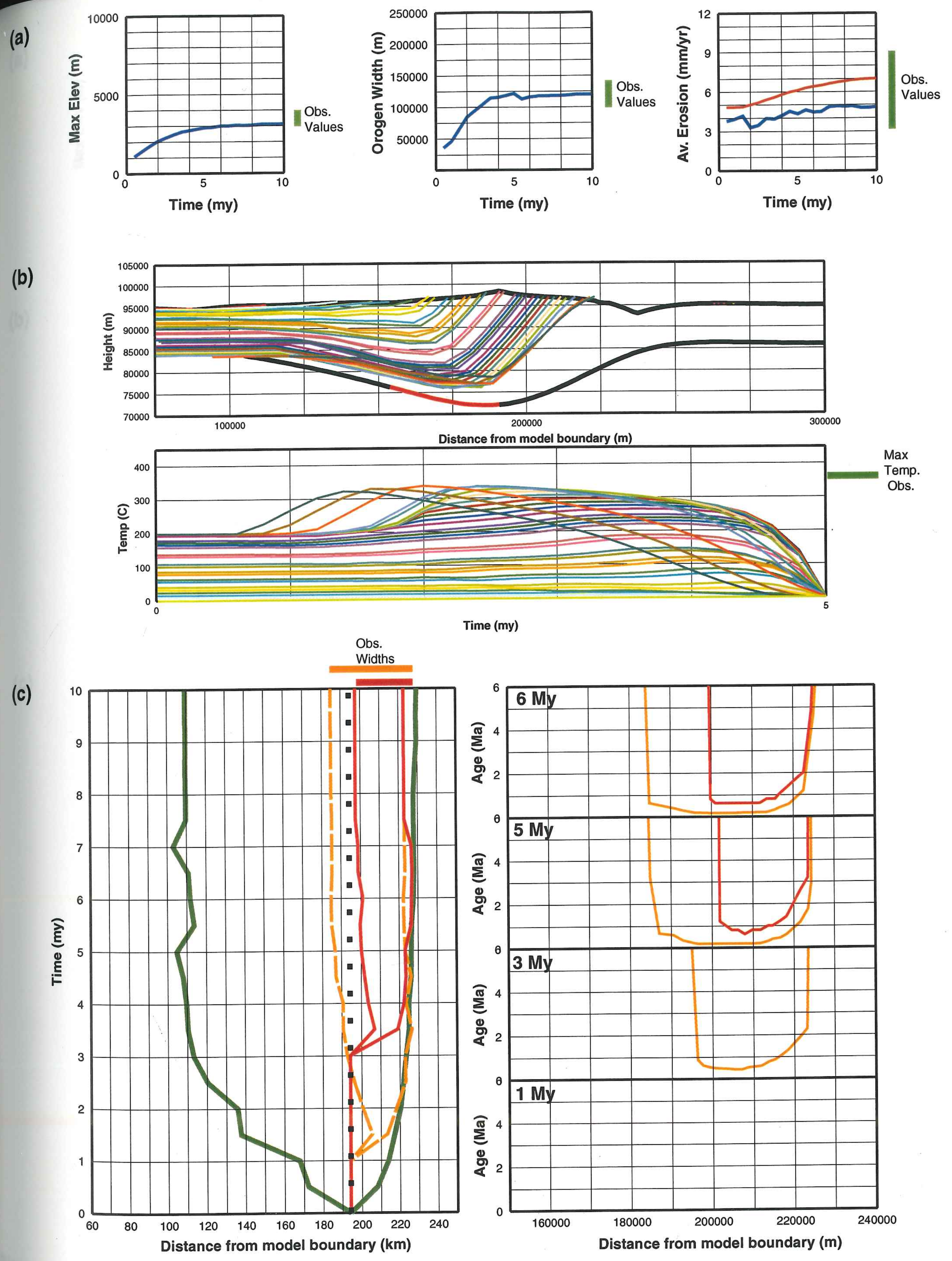

Figure 6.8: Model Mt51 (shown here) is identical to the preferred model (Mt48) but has only 25% underplating. (c) The reduction in the amount of underplating results in AFT and ZFT reset zones that are approximately 5 km narrower than those observed in the Taiwan orogen.

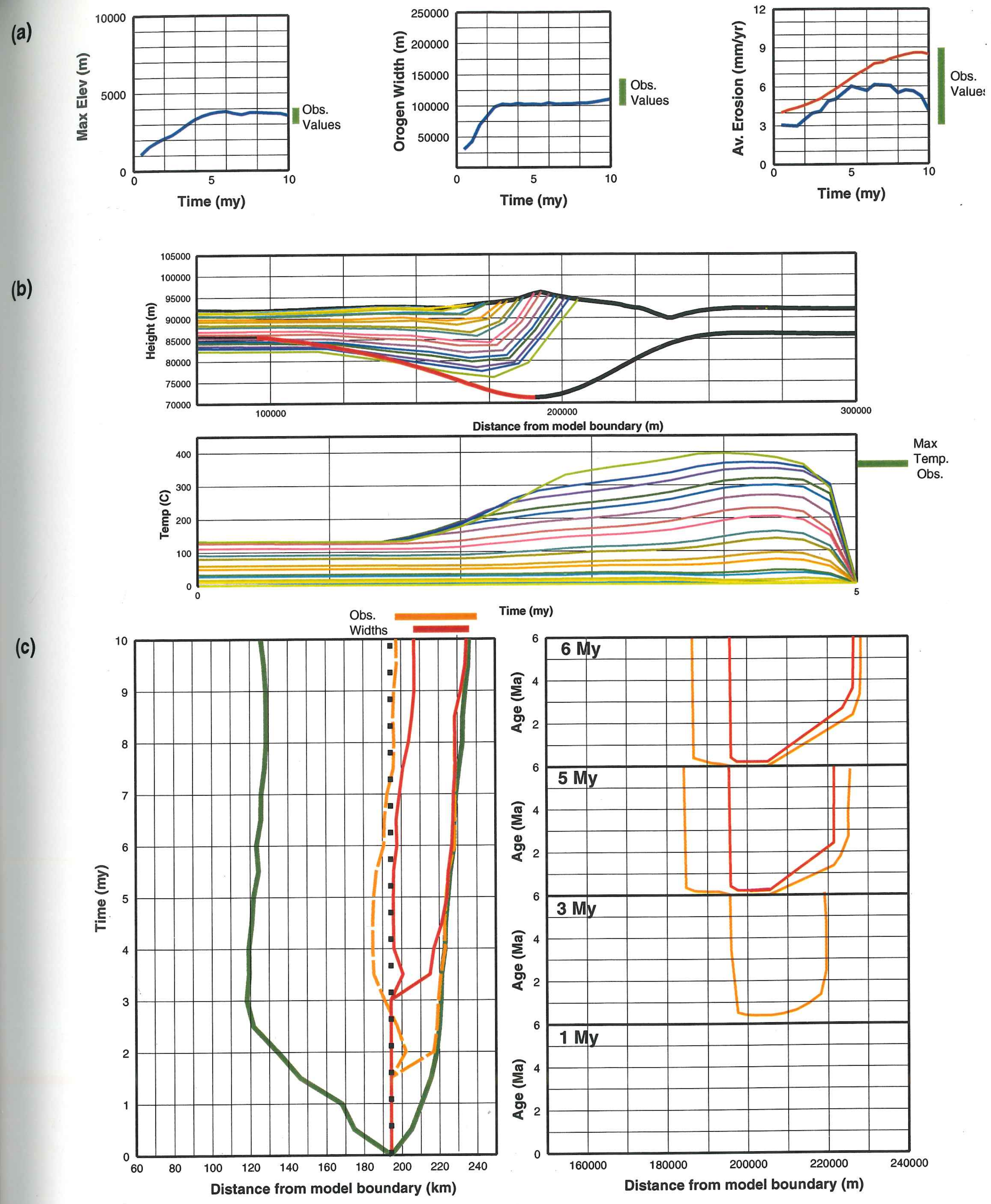

Figure 6.9: Results of model Mt52. A wider zone of underplating also produces narrower reset zones than those seen in model Mt48 (figure 6.4). Note that the tracked particles reach temperatures much higher than the upper limit of 350 C. After model parameters are adjusted to lower the maximum temperatures reached, the reset zones will be even narrower.

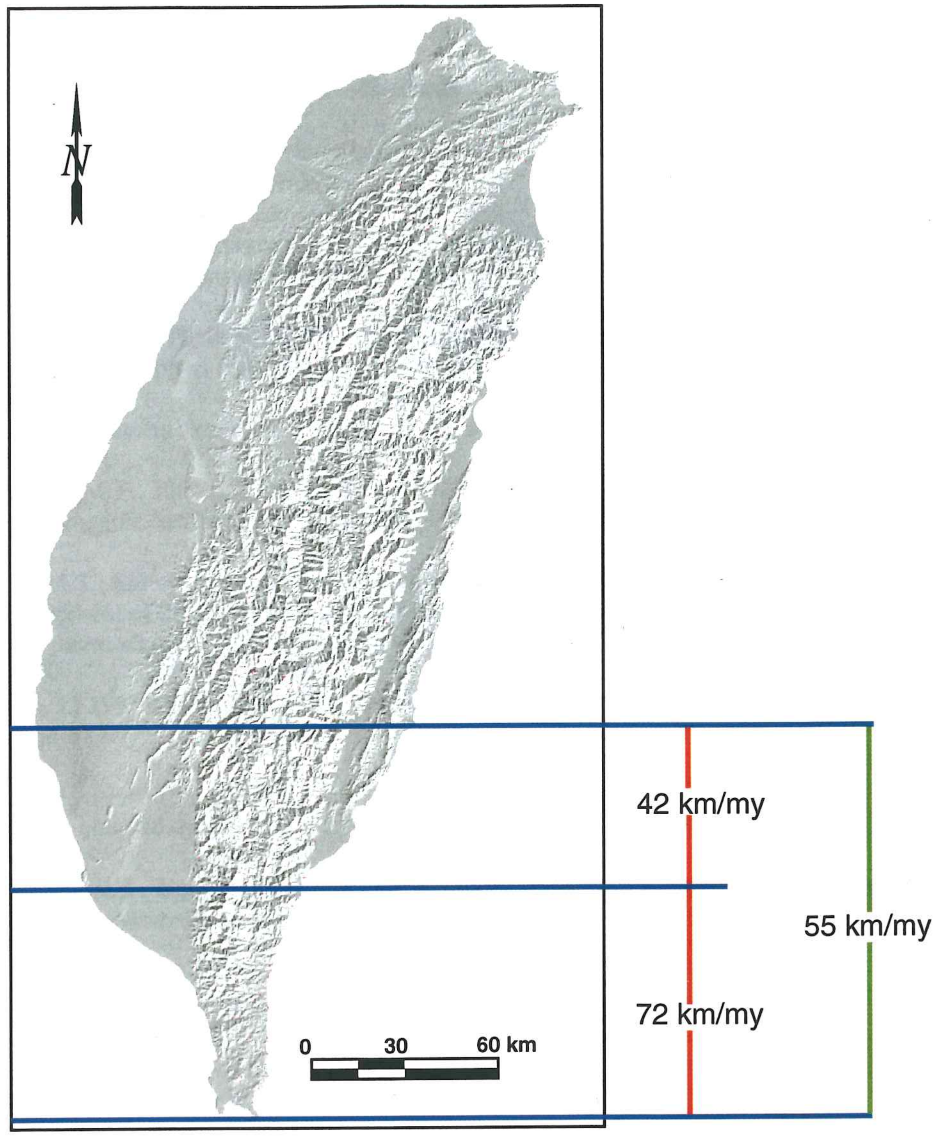

Figure 6.10: Propagartion rates determined for the Taiwan collision and the area over which they were determined. Note the increase in propagration rate in the south.

References

Barr, T.D. and Dahlen, F.A., 1989. Brittle Frictional Mountain Building 2. Thermal Structure and Heat Budget. J. Geophys. Res., 94: 3923-3947.

Barr, T.D. and Dahlen, F.A., 1990. Constraints on friction and stress in the Taiwan fold-and-thrust belt from heat flow and geochronology. Geology, 18: 111-115.

Barr, T.D., Dahlen, F.A. and McPhail, D.C., 1991. Brittle frictional mountain building 3. Low-grade metamorphism. J. Geophys. Res., 96: 10319-10338.

Bathe, K.J., 1996. Finite Element Procedures. Prentice Hall, Englewood Cliffs, New Jersey, 1037 pp.

Batt, G.E. and Brandon, M.T., 2002. Lateral Thinking: 2-D Interpretation of Thermochronology in Convergent Orogenic Settings. Tectonophysics, 349: 185-201.

Batt, G.E., Brandon, M.T., Farley, K.A. and Roden-Tice, M.K., 2001. Tectonic synthesis of the Olympic Mountains segment of the Cascadia wedge, using two-dimensional thermal and kinematic modeling of thermochronological ages. J. Geophys. Res., 106: 26,731-26,746.

Batt, G.E. and Braun, J., 1997. On the thermomechanical evolution of compressional orogens. Geophys. J. Int., 128: 364-382.

Batt, G.E. and Braun, J., 1999. The tectonic evolution of the Southern Alps, New Zealand: insights from fully thermally coupled dynamical modeling. Geophys. J. Int., 136: 403-420.

Beaumont, C., Jamieson, R.A., Nguyen, M.H. and Lee, B., 2001. Himalayan tectonics explained by extrusion of a low-viscosity crustal channel coupled to focused surface denudation. Nature, 414: 738-742.

Bird, P., 1978. Finite element modeling of lithosphere deformation: The Zagros collision orogeny. Tectonophysics, 50: 307-336.

Brandon, M.T., 1992. Decomposition of fission track age distributions. Am. J. Sci., 292: 535-564.

Brandon, M.T., Roden-Tice, M.K. and Garver, J.I., 1998. Late Cenozoic exhumation of the Cascadia accretionary wedge in the Olympic Mountains, northwest Washington State. GSA Bulletin, 110: 985-1009.

Brandon, M.T. and Vance, J.A., 1992. Fission-track ages of detrital zircon grains: implications for the tectonic evolution of the Cenozoic
Olympic subduction complex. Am. J. Sci., 292: 565-636.

Briais, A. and Pautot, G., 1992. Reconstructions of the South China Sea from structural data and magnetic anomalies. In: J. Xianglong, H.R. Kudrass and G. Pautot (Editors), Marine Geology and Geophysics of the South China Sea. China Ocean Press, pp. 60-69.

Broggi, J.A., 1932. Preliminary note on a physical phenomenon resembling mountain-building. American Journal of Science, 23: 1067-1070.

Burtner, R.L., Nigrini, A. and Donelick, R.A., 1994. Thermochronology of lower Cretaceous source rocks in the Idaho-Wyoming Thrust Belt. American Association of Petroleum Geologists Bulletin, 78: 1613-1636.

Byrne, T. and Crespi, J., 1997. Kinematics of the Taiwan arc-continent collision and implications for orogenic processes, International Conference and Sino-American Symposium on Tectonics of East Asia, Program and Abstracts, pp. 38.

Carena, S., Suppe, J. and Kao, H., 2001. Imaging the Main Detachment under Taiwan: Implications for the Critical-Taper Mechanics and Large Scale Topography. Eos Trans. AGU, 82(Fall Meet. Suppl.): Abstract T32A-0863.

Carlson, W.D., Donelick, R.A. and Ketcham, R.A., 1999. Variability of apatite fission-track annealing kinetics: I. Experimental results. American Mineralogist, 84: 1213-1223.

Cerveny, P.F., Naeser, N.D., Zeitler, P.K., Naeser, C.W. and Johnson, N.M., 1988. History of uplift and relief of the Himalaya during the past 18 million years: Evidence from fission-track ages of detrital zircons from sandstones of the Siwalik group. In: K.L. Kleinsphen and C. Paola (Editors), New Perspectives in Basin Analysis. Springer-Verlag, Berlin, pp. 43-61.

Chang, C.P., Angelier, J. and Huang, C.Y., 2000. Origin and evolution of a melange: the active plate boundary and suture zone of the Longitudinal Valley, Taiwan. Tectonophysics, 325: 43-62.

Chapple, W.M., 1978. Mechanics of thin-skinned fold-and-thrust belts. Geol. Soc. Am. Bull., 89: 1189-1198.

Chemenda, A.I., Yang, R.K., Stephan, J.F., Konstantinovskaya, E.A. and Ivanov, G.M., 2001. New results from physical modeling of arc-continent collision in Taiwan: evolutionary model. Tectonophysics, 333: 159-178.

Chen, C.S., 1999a. Recent MT Surveying Supports the Thin-Skinned Structures in the Orogen. J. Geol. Soc. China, 42: 59-68.

Chen, C.S., 1999b. Recent MT surveying supports the thin-skinned structures in the orogen. J. Geol. Soc. China, 42: 59-68.

Clark, M.B., Fisher, D.M., Lu, C.Y. and Chen, C.H., 1993. Kinematic analyses of the Hsuehshan Range: A large scale pop-up structure. Tectonics, 12: 205-217.

Clark, S.P. and Jager, E., 1969. Denudation rate in the Alps from geochronologic and heat flow data. American Journal of Science, 267: 1143-1160.

Copeland, P. and Harrison, T.M., 1990. Episodic rapid uplift in the Himalaya revealed by Ar-40/Ar-39 analysis of detrital K-feldspar and muscovite, Bengal fan. Geology, 18: 354-357.

Cowan, D.S. and Silling, R.M., 1978. A Dynamic, Scaled Model of Accretion at Trenches and Its Implications for the Tectonic Evolution of Subduction Complexes. J. Geophys. Res., 83: 5389-5396.

Crespi, J.M., Chan, Y.C. and Swaim, M.S., 1996. Synorogenic extension and underplating of the Taiwan hinterland. Geology, 24: 247-250.

Crowley, K.D., 1993. Lenmodle: a forward model for calculating length distributions and fission-track ages in apatite. Computers and Geosciences, 19: 619-626.

Dahlen, F.A. and Barr, T.D., 1989. Brittle Frictional Mountain Building 1: Deformation and Mechanical Energy budget. J. Geophys. Res., 94: 3906-3922.

Davis, D., Suppe, J. and Dahlen, F.A., 1983. Mechanics of fold-and-thrust belts and accretionary wedges. J. Geophys. Res., 88: 1153-1172.

Dodson, M.H., 1973. Closure Temperature in Cooling Geochronological and Petrological Systems. Contributions to Mineralogy and Petrology, 40: 259-274.

Dodson, M.H., 1979. Theory of Cooling Ages. In: E. Jager and J.C. Hunziker (Editors), Lectures in Isotope Geology. Springer-Verlag, New York, pp. 194-206.

Donelick, R.A., 1993. A method of fission track analysis utilizing bulk chemical etching of apatite. U.S. Patent 5,267,274.

Donelick, R.A., Roden, M.K., Mooers, J.D., Carpenter, B.S. and Miller, D.S., 1990. Etchable length reduction of induced fission tracks in apatite at room temperature (23 C): crystallographic orientation effects and "initial" mean lengths. Nuclear Tracks, 17: 261-265.

Dorsey, R.J. and Lundberg, N., 1988. Lithofacies analysis and basin reconstruction of the Plio-Pleistocene collisional basin, Coastal Range of eastern Taiwan. Acta Gelo Taiwan, 26: 57-132.

Duddy, I.R., Green, P.F. and Laslett, G.M., 1988. Thermal annealing of fission tracks in apatite 3. Variable temperature behavior. Chemical Geology, 73: 25-38.

Ehlers, T.A., 2001. Geothermics of Exhumation and Erosion in the Wasatch Mountains, Utah. Ph.D. Thesis, University of Utah, Salt Lake City, 106 pp.

Ellwood, A., Wang, C.Y., Teng, L.S. and Yen, H.Y., 1996. Gravimetric examination of thin-skinned detachment vs. basement-involved models for the Taiwan orogen. J. Geol. Soc. China, 39: 209-221.

England, P. and Houseman, G., 1985. Role of lithospheric strength heterogeneities in the tectonics of Tibet and neighboring regions. Nature, 315: 297-301.

England, P. and McKenzie, D., 1982. A thin viscous sheet model for continental deformation. Geophys. J. Royal Astr. Soc., 70: 295-321.

Escher, A. and Beaumont, C., 1997. Formation, burial and exhumation of basement nappes at crustal scale: a geometric model based on the Western Swiss-Italian Alps. Journal of Structural Geology, 19: 955-974.

Farley, K.A., 2000. Helium diffusion from apatite: General behavior as illustrated by Durango fluorapatite. J. Geophys. Res., 105: 2903-2914.

Fleischer, R.L. and Price, P.B., 1964. Techniques for geologic dating of minerals by chemical etching of fission fragments. Geochim. Cosmochim. Acta., 28: 1705-1714.

Fleischer, R.L., Price, R.B. and Walker, L.M., 1964. Fission track ages of zircons. J. Geophys. Res., 69: 4885-4888.

Foster, D.A., Kohn, B.P. and Gleadow, A.J.W., 1996. Sphene and zircon closure temperatures revisited: Empirical calibrations from Ar-40/Ar-39 diffusion studies of K-feldspar and biotite. International Workshop on Fission Track Dating.

Fowler, C.M.R., 1990. The Solid Earth. Combridge University Press, Cambridge, 472 pp.

Fuller, C.W., Willett, S.D., Hovius, N. and Slingerland, R., In press. Erosion rates for Taiwan mountain basins: New determinations from suspended sediment records and a stochastic model of their temporal variation. Journal of Geology.

Fullsack, P., 1995. An arbitrary Langrangian-Eulerian formulation for creeping flows and its application in tectonic models. Geophys. J. Int., 1995: 1-23.

Galbraith, R.F., 1981. On statistical models for fission-track counts. J. Math. Geol., 13: 471-478.

Garver, J.I., Brandon, M.T., Roden-Tice, M. and Kamp, P.J.J., 1999. Exhumation history of orogenic highlands determined by detrital fission-track thermochronology. In: U. Ring, M.T. Brandon, G.S. Lister and S.D. Willett (Editors), Exhumation processes: Normal Faulting, Ductile Flow and Erosion. Geological Society, London, pp. 283-304.

Green, P.F., 1981. A new look at statistcs in fission-track dating. Nuclear Tracks, 5: 77-86.

Green, P.F., 1986. On the thermotectonic evolution of northern England: evidence from fission track analysis. Geol. Mag., 123: 405-415.

Green, P.F., Duddy, I.R., Gleadow, A.J.W., Tingate, P.R. and Laslett, G.M., 1985. Fission-track annealing in apatite: track length measurements and the form of the Arrhenius plot. Nuclear Tracks and Radiation Measurements, 10: 323-328.

Green, P.F., Duddy, I.R., Gleadow, A.J.W., Tingate, P.R. and Laslett, G.M., 1986. Thermal annealing of fission tracks in apatite, 1. A qualitative description. Chemical Geology, 59: 237-253.

Green, P.F. et al., 1989. Thermal annealing of fission-tracks in apatite 4. Quantitative modeling techniques and extension to geologic timescales. Chemical Geology, 79: 155-182.

Hall, J., 1859. The Natural History of New York, Part 6- Paleontology, J.3. Van Benthuysen, Albany, 1-85 pp.

Hall, R., Ali, J.R., Anderson, C.D. and Baker, S.J., 1995. Origin and motion history of the Philippine Sea Plate. Tectonophysics, 251: 229-250.

Harrison, T.M., Armstrong, R.L., Naeser, C.W. and Harakal, J.E., 1979. Geochronology and thermal history of the Coast Plutonic Complex, near Prince Rupert, British Columbia. Can. J. Earth Sci., 16: 400-410.

Ho, C.S., 1986. A synthesis of the geologic evolution of Taiwan. Tectonophysics, 125: 1-16.

Houseman, G.A., McKenzie, D.P. and Molnar, P., 1981. Convective instability of a thickened boundary layer and its relevance for the thermal evolution of continental convergent belts. J. Geophys. Res., 86: 6115-6132.

Howard, A.D. and Kirby, G., 1983. Channel changes in badlands. Geo. Soc. of Am. Bul., 94: 739-752.

Huang, C.Y., Yuan, P.B., Lin, C.W., Wang, T.K. and Chang, C.P., 2000. Geodynamic processes of Taiwan arc-continent collision and comparisons with analogs in Timor, Papua New Guinea, Urals and Corsica. Tectonophysics, 325: 1-21.

Huerta, A.D., Royden, L.H. and Hodges, K.V., 1996. The interdependence of deformational and thermal processes in mountain belts. Science, 273: 637-639.

Huerta, A.D., Royden, L.H. and Hodges, K.V., 1998. The thermal structure of collisional orogens as a response to accretion, erosion and radiogenic heating. J. Geophys. Res., 103: 15,287-15,302.

Huerta, A.D., Royden, L.H. and Hodges, K.V., 1999. The effects of accretion, erosion and radiogenic heat on metamorphic evolution of collisional orogens. J. Metamorphic Geol., 17: 349-366.

Jamieson, R.A., Beaumont, C., Fullsack, P. and Lee, B., 1998. Barrovian regional metamorphism: where's the heat? In: P.J. Treloar and P.J. O'Brien (Editors), What Drives Metamorphism and Metamorphic Reactions? Geological Society of London, London, pp. 23-51.

Jamieson, R.A., Beaumont, C., Hamilton, J. and Fullsack, P., 1996. Tectonic assembly of inverted metamorphic sequences. Geology, 24: 839-842.

Jamieson, R.A., Beaumont, C., Nguyen, M.H. and Lee, B., 2002. Interaction of metamorphism, deformation and exhumation in large convergent orogens. J. Metamorphic Geology, 20: 9-24.

Kamp, P.J.J., Green, P.F. and White, S.H., 1989. Fission track analysis revals character of collisional tectonics in New Zealand. Tectonics, 8: 169-195.

Ketcham, R.A., Donelick, R.A. and Carlson, W.D., 1999. Variability of apatite fission-track annealing kinetics: III. Extrapolation to geological timescales. American Mineralogist, 84: 1235-1255.

Ketcham, R.A., Donelick, R.A. and Donelick, M.B., 2000. AFTSolve: A program for multi-kinetic modeling of apatite fission-track data. Geological Materials Research, 2: 1-30.

Kohlstedt, D.L., Evans, B. and Mackwell, S.J., 1995. Strength of the lithosphere: Constraints imposed by laboratory experiments. J. Geophys. Res., 100: 17,587-17,602.

Kooi, H. and Beaumont, C., 1996. Large-scale geomorphology: Classical concepts reconciled and integrated with contemporary ideas via a surface process model. J. Geophys. Res., 101: 3361-3386.

Koons, P.O., 1987. Some thermal and mechanical consequences of rapid uplift: an example from the Southern Alps, New Zealand. Earth and Plan. Sci. Let., 86: 307-319.

Krishnaswami, S., Lal, D., Prabhu, N. and MacDougall, D., 1974. Characteristics of fission tracks in zircon: applications to geochronology and cosmology. Earth Plan. Sci. Let., 22: 51-59.

Kronenberg, A.K. and Tullis, J., 1984. Flow Strengths of Quartz Aggregates: Grain Size and Pressure Effects due to Hydrolytic Weakening. J. Geophy. Res., 89: 4281-4297.

Li, Y.H., 1976. Denudation of Taiwan Island since the Pliocene Epoch. Geology, 4: 105-107.

Lin, C.H., 1998. Tectonic implications of an aseismic belt beneath the eastern Central Range of Taiwan: Crustal subduction and exhumation. J. Geol. Soc. China, 41: 441-460.

Lin, C.H., 2000. Thermal modeling of continental subduction and exhumation constrained by heat flow and seismicity in Taiwan. Tectonophysics, 324: 189-201.

Liu, T.K., 1982. Tectonic implications of fission track ages from the Central Range, Taiwan. Proc. Geol. Soc. China, 25: 22-37.

Liu, T.K., Hsieh, S., Chen, Y.G. and Chen, W.S., 2001. Thermo-kinematic evolution of the Taiwan oblique-collision mountain belt as revealed by zircon fission track dating. Earth Plan. Sci. Let., 186: 45-56.

Lo, C.H. and Onstott, T.C., 1995. Rejuvenation of K-Ar systems for minerals in the Taiwan Mountain Belt. Earth Plan. Sci. Let., 131: 71-98.

Ma, K.F. and Liu, N.J., 1997. The images of subduction slabs in the Taiwan region. J. Geol. Soc. China, 40: 653-670.

Malavieille, J. et al., In press. Arc-Continent Collision in Taiwan: New Marine Observations and Tectonic Evolution. Geological Society of American Special Paper.

Molnar, P. and England, P., 1995. Temperatures in zones of steady-state underthrusting of young oceanic lithosphere. Earth Plan. Sci. Let., 131: 57-70.

Mouthereau, F., Lacombe, O., Deffontaines, B., Angelier, J. and Brusset, S., 2001. Deformation history if the southwestern Taiwan foreland thrust belt: insights from tectono-sedimentary analyses and balanced cross-sections. Tectonophysics, 333: 293-322.

Naeser, C.W., 1979. Fission-Track Dating and Geological Annealing of Fission Tracks. In: E. Jager and J.C. Hunziker (Editors), Lectures in Isotope Geology. Springer-Verlag, New York, pp. 154-169.

Pazzaglia, F.J. and Brandon, M.T., 2001. A fluvial record of long-term steady-state uplift and erosion across the Cascadia forearc high, western Washington State. American J. Science, 301: 385-431.

Pope, D.C., 1997. Thermal-Mechanical Modeling of Andean Orogenesis by Ablative Subduction. Ms. Thesis, University of Pennsylvania, 94 pp.

Pope, D.C. and Willett, S.D., 1998. Thermal-mechanical model for crustal thickening in the central Andes driven by ablative subduction. Geology, 26: 511-514.

Rau, R.J. and Wu, F.T., 1995. Tomographic imaging of lithospheric structures under Taiwan. Earth Plan. Sci. Let., 133: 517-532.

Ravenhurst, C.E. and Donelick, R.A., 1992. Fission Track Thermochronometry. In: M. Zentilli (Editor), Short Course on Low Temperature Thermochronology. Mineralogical Association of Canada, Nepean, Ontario, pp. 21-42.

Sacks, P.E. and Secor, D.T., 1990. Delamination in collisional orogens. Geology, 18: 999-1002.

Scholz, C.H., 1980. Shear Heating and the State of Stress on Faults. J. Geophys. Res., 85: 6174-6184.

Stockmal, G.S., 1983. Modelling of Large Scale Accretionary Wedge Deformation. J. Geophys. Res., 88: 8271-8287.

Suppe, J., 1980. A Retrodeformable Cross Section of Northern Taiwan. Proceedings of the Geological Society of China, 23: 46-55.

Suppe, J., 1981. Mechanics of mountain building and metamorphism is Taiwan. Mem. Geol. Soc. China, 4: 67-89.

Suppe, J., 1984. Kinematics of arc-continent collision, flipping of subduction and back-arc spreading neat Taiwan. Memo. Geol. Soc. China, 6: 21-34.

Tang, J.C. and Chemenda, A.I., 2000. Numerical modeling of arc-continent collision: application to Taiwan. Tectonophysics, 325: 23-42.

Teng, L.S., 1992. Geotectonic evolution of Tertiary continental margin basins of Taiwan. Pet. Geol. Taiwan, 27: 1-19.

van der Beek, P., 1995. Tectonic evolution of continental rifts, inferences from numerical modeling and fission track thermochronology. PhD Thesis, Free University, Amsterdam.

Wagner, G.A., 1968. Fission-track dating of apatites. Earth Plan. Sci. Let., 4: 411-415.

Wagner, G.A. and Reimer, G.M., 1972. Fission-track tectonics: the tectonic interpretation of fission track apatite ages. Earth Plan. Sci. Let., 14: 263-268.

Wagner, G.A., Reimer, G.M. and Jager, E., 1972. Cooling ages derived by apatite fission-track, mica Rb-Sr and K-Ar dating: the uplift and cooling history of the Central Alps. Memoir of the Institute of Geology and Mineralogy, University of Padova, 30: 1-27.

Willett, S.D., 1992a. Dynamic and kinematic growth and change of a Coulomb wedge. In: K.R. McClay (Editor), Thrust Tectonics. Chapman and Hall, London, pp. 19-31.

Willett, S.D., 1992b. Modeling thermal annealing of fission tracks in apatite. In: M. Zentilli (Editor), Short Course on Low Temperature Thermochronology. Mineralogical Association of Canada, Nepean, Ontario, pp. 43-72.

Willett, S.D., 1999. Orogeny and orography: The effects of erosion on the structure of mountain belts. J. Geophys. Res., 104: 28,957-28,981.

Willett, S.D., Beaumont, C. and Fullsack, P., 1993. Mechanical model for the tectonics of doubly vergent compressional orogens. Geology, 21: 371-374.

Willett, S.D. and Brandon, M.T., 2002. On steady states in mountain belts. Geology, 30: 175-178.

Wintsch, R.P., Byrne, T. and Toriumi, M., 1999. Exhumation of the Sanbagawa blueschist belt, SW Japan, by lateral flow and extrusion: evidence from structural kinematics and retrograde *P-T-t* paths. In: U. Ring, M.T. Brandon, G.S. Lister and S.D. Willett (Editors), Exhumation Processes: Normal Faulting, Ductile Flow and Erosion. Geological Society, London, pp. 129-155.

Wolf, R.A., Farley, K.A. and Kass, D.M., 1998. Modeling of the temperature sensitivity of the apatite (U-Th)/He thermochronometer. Chemical Geology, 148: 105-114.

Wolf, R.A., Farley, K.A. and Silver, L.T., 1996a. Assessment of (U-Th)/He thermochronometry: The low-temperature history of the San Jacinto Mountains, California. Geology, 25: 65-68.

Wolf, R.A., Farley, K.A. and Silver, L.T., 1996b. Helium diffusion and low-temperature thermochronometry of apatite. Geochim. Cosmochim. Acta, 60: 4231-4240.

Wu, F.T., Rau, R.J. and Salzberg, D., 1997. Taiwan orogen: thin-skinned or lithospheric collision. Tectonophysics, 274: 191-220.

Yamada, R., Tagami, T., Nishimura, S. and Ito, H., 1995. Annealing kinetics of fission tracks in zircon: an experimental study. Chem. Geol., 122: 249-258.

Yen, H.Y., Yeh, Y.H. and Wu, F.T., 1998. Two-dimensional crustal structures of Taiwan from gravity data. Tectonics, 17: 104-111.

Yu, S.B., Chen, H.Y. and Kuo, L.C., 1997. Velocity of GPS stations in the Taiwan area. Tectonophysics, 274: 41-59.

Zeitler, P.K., 1985. Cooling history of the Himalaya, Pakistan. Tectonics, 4: 127-151.

Zeitler, P.K., Herczeg, A.L., McDougall, I. and Honda, M., 1987. U-Th-He dating of apatite: A potential thermochronometer. Geochim. Cosmo. Acta, 51: 2865-2868.

Zienkiewicz, O.C. and Godbole, P.N., 1974. Flow of plastic and visco-plastic solids with special reference to extrusion and forming processes. International Journal for Numerical Methods in Engineering, 8: 3-16.